3A1: Applications to External Flows

Contents

1 Introduction

The lectures in this part of the 3A1 course discuss a central part of external aerodynamics: the theory of incompressible flow around wings. This body of work was developed in the course of the 20th Century, up to about 1980. One may thus query its continued relevance, both to aerodynamicists and to engineers in general. The majority of this introduction consists of a justification of this point. Also given are a brief reference list and a description of the lecture format.

1.1 Motivation

Computing power has increased vastly in the past 25 years, and much more complex calculations than anything discussed in this course are now possible. So, why not simply solve all the problems of external aerodynamics numerically using the latest codes?

The first argument against this is that such an approach is time-consuming and costly, not just in the computation itself, but also the associated overheads (grid generation and optimisation, results post-processing etc). In the early stages of design, engineers need to consider a wide range of possibilities quickly, and thus require simpler, more economical, modelling tools.

The second argument is more abstract, but also more significant. Hand-in-hand with the formulation of simplified theoretical models goes the development of a *conceptual understanding* of the problem under consideration. This understanding is a hugely powerful asset. If you compare the civil aircraft of 50 years ago with those of today, you will see that the fundamental configuration for high-speed, subsonic flight was already fully established, by designers armed only with the ideas we will discuss in this course.

This point brings us to the general relevance of wing theory to engineers. It is a shining example of how a complex problem may be approached by first splitting it into simplified component elements, and then combining the insights obtained to form the conceptual understanding mentioned earlier. In this sense, it represents a way of thinking that is essential to an engineer of any discipline.

1.2 References

These notes draw heavily on ideas (and diagrams!) from the following books:

Anderson, 'Fundamentals of aerodynamics' (ISBN 0-07-001679-8). Possibly the most complete recent treatment, with some nice historical asides.

Glauert, 'The elements of aerofoil and airscrew theory' (CUED shelfmark TD.32A/C/E/F). A beautifully lucid exposition of the classical theory by 'the English Prandtl'.

Milne-Thomson, 'Theoretical aerodynamics' (CUED shelfmark TD.60). A later, and more rigorous/mathematical, account than Glauert of the classical theory.

Jones, 'Wing theory' (CUED shelfmark TD.125). Heavy-duty wing theory, by a guru of the subject. Masterful, but probably too condensed to be used as an introductory text.

Katz & Plotkin, 'Low speed aerodynamics' (CUED shelfmark TD.140/B/C, TD.128B). A recent theoretical treatment, particularly useful for its detailed discussion of panel methods.

Barnard & Philpott, 'Aircraft flight' (CUED shelfmark TQ.88). Equation-free aerodynamics, with emphasis on physical principles. An excellent adjunct to the more theoretical texts.

Simons, 'Model aircraft aerodynamics' (ISBN 1-85486-121-2). Aimed at model-builders, so combines the 'physical' approach of Barnard & Philpott with a simplified account of the theory. Clear and informative.

1.3   Lecture Format

The lectures will cover the material in these notes, but in a presentational format and with other, supporting, material. They will thus appear substantially different, and you should not expect to be able to follow the notes line-by-line during a lecture. However, the notes *do* contain all the material you need for the examples papers and the exam.

The handout has two main sections, dealing respectively with 2D and 3D wing flows. In each case, the exposition moves from relatively complex descriptions, which can only be solved numerically, to simpler representations that provide the insight needed for a conceptual understanding of the topic. There is also an appendix containing supporting mathematical derivations.

2 Two-dimensional Flow Around Aerofoil Sections

2.1 General Features

An aerofoil section is a streamlined shape that, when placed in a high Reynolds number flow at appropriate incidence (angle of attack) generates a relatively large perpendicular force (lift) for a relatively small streamwise force (drag). The range of appropriate angles of attack typically covers small positive values (e.g. 2 – 12 degrees). In this section, we briefly summarise the characteristics of the flow as the angle of attack varies from below to above the working range.
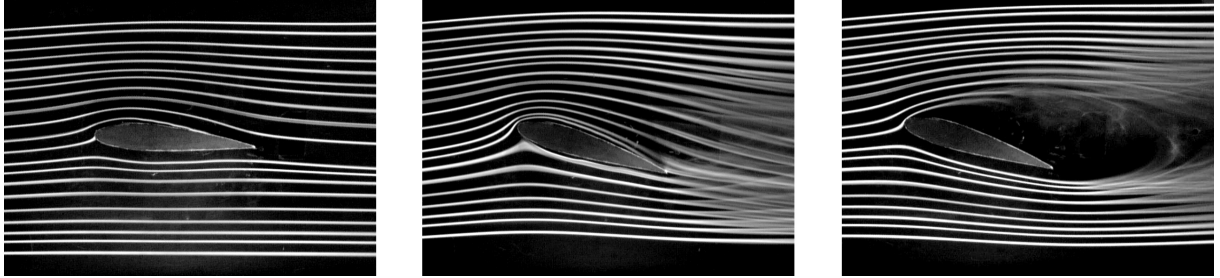

Figure 1: Smoke visualisation of flow around an aerofoil section; from left to right: (a) low incidence; (b) working incidence; (c) high incidence.

At low incidence, (Figure 1(a)), the flow is attached to the aerofoil surface throughout. The drag is largely determined by skin friction, and is thus small. The corresponding boundary layers are thin, as is the wake that they form at the trailing edge. Most of the lift generated is due to section asymmetry (camber). A typical associated surface pressure distribution is shown in Figure 2 ($\alpha = 1°$), with the lower surface line plotted dashed. Both curves start at the stagnation point ($c_p = 1$), which sits very close to the leading edge, and then drop to negative (below atmospheric) values, as one would expect from the streamline curvature visible in Figure 1(a). This curvature is greater above the upper surface, thanks to the aerofoil camber, resulting in more suction and hence a net lift force. Towards the trailing edge the streamline curvature reverses as the flow straightens out, so the pressure recovers to (typically) slightly above atmospheric.

As the incidence is increased, into the working range, the flow remains attached (Figure 1(b)) but the pressure distribution develops a marked suction peak near the leading edge (Figure 2, $\alpha = 7°, 12°$). The average pressure difference between lower and upper surfaces also increases. Self-evidently, there is an increase in lift; less obviously, the drag also rises. The increase consists largely of form drag, due to incomplete cancellation of the streamwise pressure forces on the aerofoil. This feature is linked to the growth of the upper surface boundary layer under the adverse pressure gradients it experiences. In contrast, the lower surface boundary layer is subject to favourable gradients, and typically remains thin. Note also that the lower surface pressures are now above atmospheric, consistent with the curvature reversal evident in Figure 1(b).

Further increases in incidence, to beyond the working range, lead to unsustainable adverse pressure gradients on the upper surface, and the flow separates (Figure 1(c)). The associated reduction in streamline curvature above the aerofoil leads to a marked loss of suction (Figure 2, $\alpha = 18°$), and hence lift. There is no corresponding reduction in form drag, however, as the lost suction is predominantly around the region where the upper surface is horizontal. Instead there is much more drag than previously, as the aerofoil is now like a bluff body, with a large region of separated flow behind it. The pressure in this region is low and almost constant (because the fluid is slow moving); note, in particular, that there is no longer a pressure recovery towards the

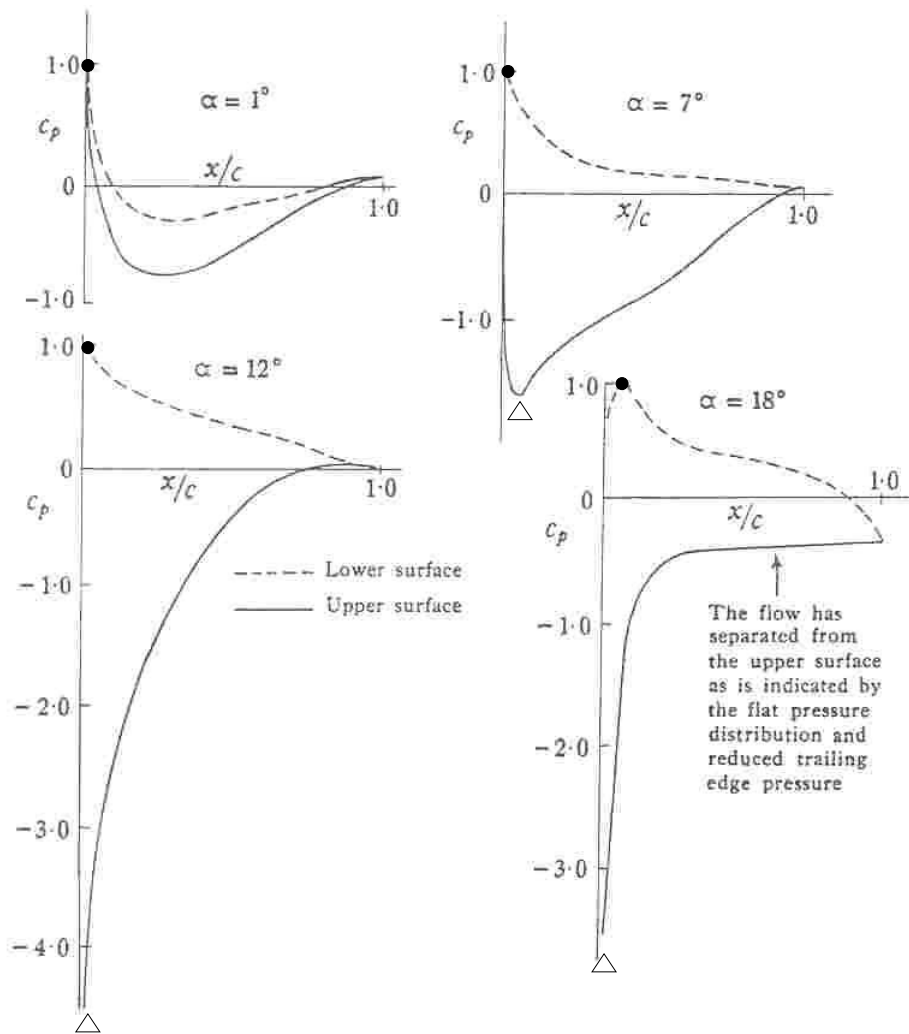Figure 2: Plots of typical pressure distributions on an aerofoil section as incidence is increased. •: stagnation point; △: suction peak. Note that $c_p = 0$ corresponds to atmospheric pressure, and suction is shown as negative, unlike the usual convention.

trailing edge. This is the source of the large (form) drag increase. Significant lift components can still be generated in this regime, but are of little use due to the high drag.

To summarise: in the working range of angles of attack, the flow around the aerofoil is attached, with a small, thin wake. Our modelling efforts will concentrate on this regime.

2.2 Modelling the flow

2.2.1 The potential flow assumption

You are already familiar with the assumption that the attached flow around an aerofoil is irrotational, and experimental observations appear to support the view that vorticity is confined to small regions – the boundary layers and wake. Here we present a more detailed theoretical justification for the potential flow hypothesis.

The vorticity equation, derived in the Incompressible Flow lectures, is

$$\frac{\partial \boldsymbol{\omega}}{\partial t} + \boldsymbol{u} \cdot \nabla \boldsymbol{\omega} - \boldsymbol{\omega} \cdot \nabla \boldsymbol{u} = \nu \nabla^2 \boldsymbol{\omega}. \tag{1}$$

For two-dimensional flow in the $x - y$ plane, we have $\boldsymbol{\omega} = \omega \boldsymbol{e}_z$ and $\boldsymbol{\omega} \cdot \nabla \boldsymbol{u} = 0$, so

$$\frac{\partial \omega}{\partial t} + \boldsymbol{u} \cdot \nabla \omega = \nu \nabla^2 \omega. \tag{2}$$

Now consider a fixed area S of air flow (Figure 3). The rate of change of the vorticity in this region is given by:

$$\frac{d}{dt} \int_S \omega dS = \int_S \frac{\partial \omega}{\partial t} dS = \int_S \left(\nu \nabla^2 \omega - \boldsymbol{u} \cdot \nabla \omega \right) dS. \tag{3}$$

The first term in the integral is already a divergence, and the second can be expressed as one by noting that

$$\nabla \cdot (\omega \boldsymbol{u}) = \omega \nabla \cdot \boldsymbol{u} + \boldsymbol{u} \cdot \nabla \omega = \boldsymbol{u} \cdot \nabla \omega \tag{4}$$

for incompressible flow. We can now use Gauss' divergence theorem to convert the area integral into one around the contour bounding S, giving

$$\frac{d}{dt} \int_S \omega dS = \int_C \left(\nu \frac{\partial \omega}{\partial n} - \omega u_n \right) dl. \tag{5}$$

This tells us that changes in the vorticity in S are due to two contributions:

$\quad -\omega u_n \quad$ the convective flux ;

$\quad \nu \frac{\partial \omega}{\partial n} \quad$ the diffusive flux.

Since both these terms are fluxes, we also see that **vorticity is neither created nor destroyed in 2D viscous flow**. (If it's not clear to you that this conclusion follows from (5) imagine a region S where all the vorticity is well away from the boundary, on which $\omega = \partial \omega / \partial n = 0$.) The **generation** of vorticity can therefore only take place at the surfaces of bodies within the flow.

The extent of the vortical region in the flow around an aerofoil thus depends on how quickly the vorticity generated at the surface diffuses outwards in comparison to the rate at which it is swept downstream. The diffusion coefficient for vorticity is ν, with dimensions m^{2}s^{-1}. Hence, in time t, one expects diffusion over a length scale $\sqrt{\nu t}$ (on dimensional grounds). If t is taken as the time for the free-stream flow to traverse the aerofoil, of chord c, then the diffusion length represents the boundary layer thickness at the trailing edge. Substituting $t = c/U$, we have

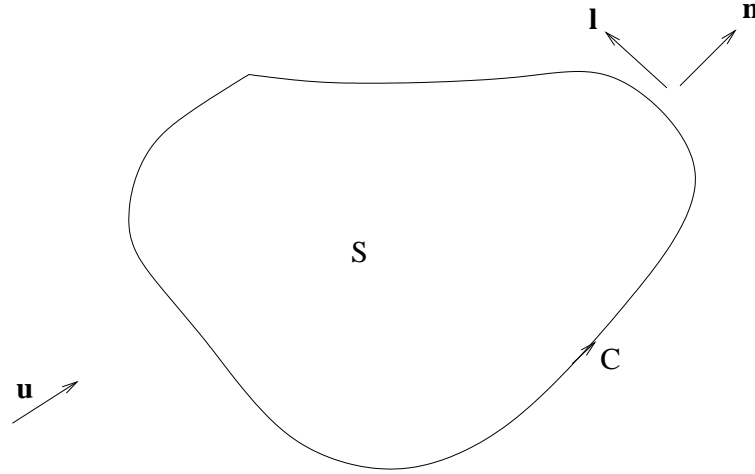$$\sqrt{\nu t} = \sqrt{\frac{\nu c}{U}} = c \sqrt{\frac{\nu}{Uc}} \tag{6}$$

Figure 3: An area, S, of two-dimensional flow. The coordinates x and l are, respectively, normal and tangential to the bounding contour, C.

and the boundary layer is thin in terms of the chord as long as the Reynolds number, Uc/ν, is large. The potential flow approximation is thus justifiable in the high Reynolds number flows of aeronautics.

2.2.2 The Kutta condition revisited

You will recall that the potential flow calculation for the flow past a body is plagued by the existence of multiple solutions and that the Kutta condition is invoked to solve this problem. To recap: the Kutta condition states that, of the three possible potential flows around an aerofoil shown in Figure 4, it is (b), which leaves the trailing edge smoothly, that represents reality most closely.

To see why the alternative flows are inadmissible, consider the pressures experienced by the boundary layer in case (a), as it passes from the lower surface to the upper, around the trailing edge. The sharp kink in the streamline at the trailing edge corresponds to infinite curvature, or zero radius of curvature. We therefore have an infinite pressure gradient across the streamlines and, correspondingly, high suction at this point. The pressure then recovers to its stagnation value at the rear stagnation point. Figure 5 shows the surface pressure field experienced by the flow. It is evident that the extreme adverse pressure gradient immediately after the trailing edge could not be sustained by a boundary layer, and the flow would separate. The same conclusion applies to case (c), leaving case (b) as the only possible attached flow around the aerofoil.

> *N.B. The Kutta condition relies on the existence of a (very thin) boundary layer. Thus, although we explain aerofoil lift in terms of an inviscid flow, it can only come about thanks to viscosity.*
> *N.B.2 For any realistic aerofoil (i.e. one with a non-zero trailing edge angle), the Kutta condition solution has a stagnation point at the trailing edge. This follows from the observation that both upper and lower surface streamlines meet there.*
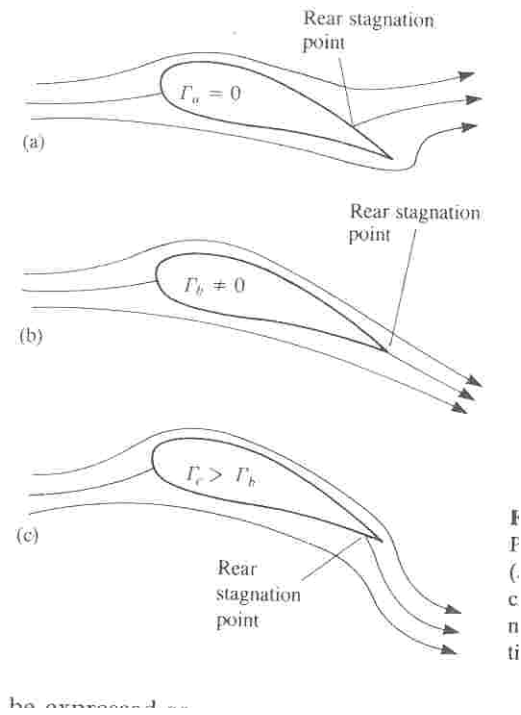
Figure 4: Possible potential flows over an aerofoil section. The circulation, Γ, is clockwise-positive in this diagram.
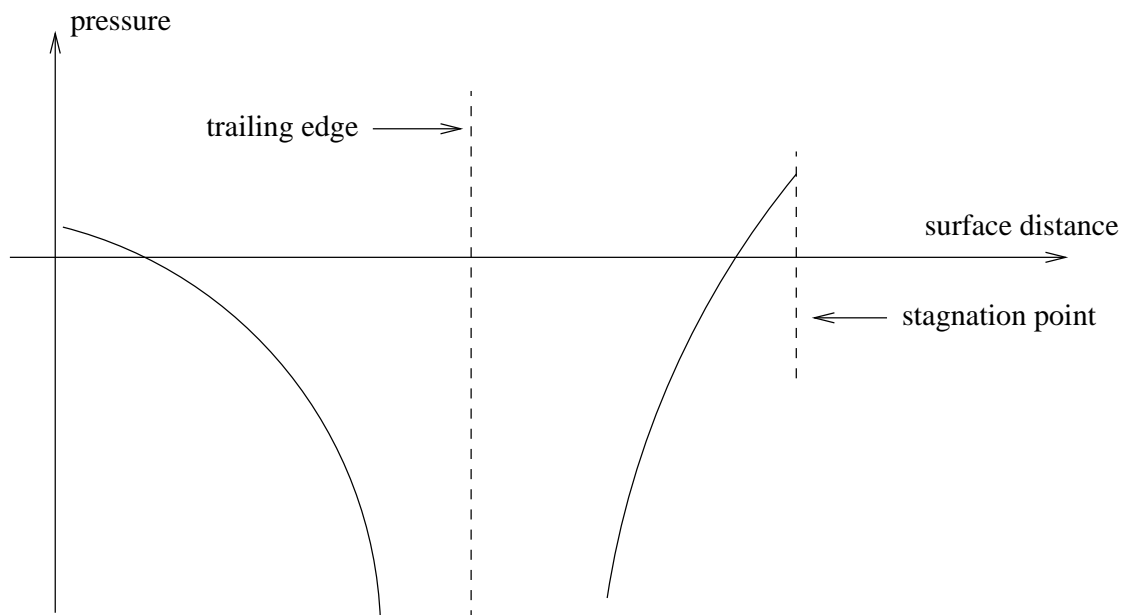

Figure 5: Surface pressure field around the trailing edge for case (a) of Figure 4

Example: Wedge flows and the Kutta condition

2.2.3 Limitations of the potential flow approximation

The potential flow solution, even with the Kutta condition applied, suffers from two important limitations. The first is well known to you; it predicts zero drag. Thus, a separate calculation of the boundary layer evolution subject to the potential flow pressure field is required.

The second limitation is more subtle. Figure 6 compares measured surface pressures on a NACA section with those calculated from potential theory. In general the agreement is good, but there is a clear discrepancy at the trailing edge, where the predicted recovery to stagnation pressure is not manifested in practice.
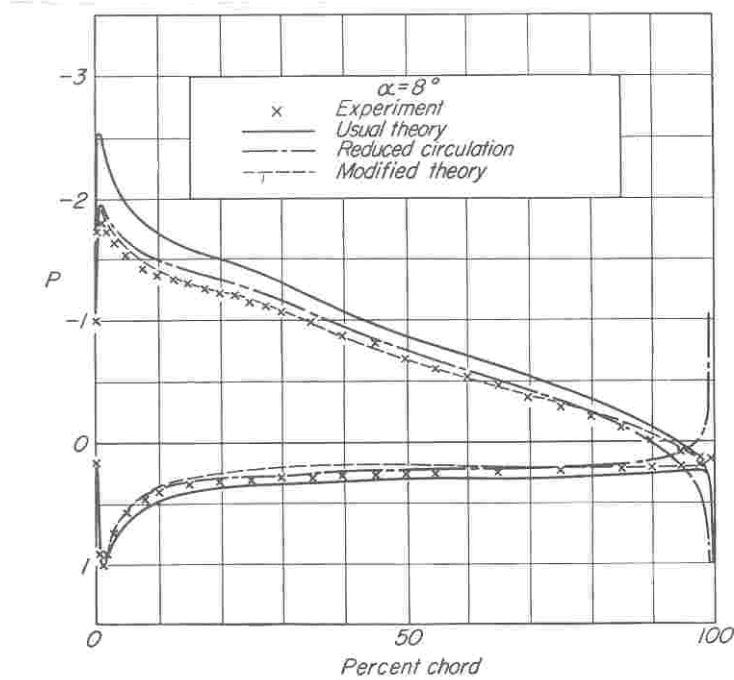
Figure 6: Experimental and theoretical pressures on a NACA 4412 section (unknown Reynolds number). The potential flow result is given by the 'usual theory' line.

This is not a problem for lift estimation, as the difference has a negligible influence on the integrated pressures. However, the strong adverse gradients would result in very significant errors in any associated boundary layer calculation. Numerical codes that calculate section properties thus have to incorporate an ad hoc 'fix' to work around this issue.

In spite of these issues, the potential flow approximation was invaluable in the early theoretical development of aerodynamics, and remains important today. The advent of cheap, high-speed computing has, however, changed the pecking order of solution techniques. In the past, the conformal mapping approach was developed to the stage where it could be used in the hand calculation of the flow around a general aerofoil section. Nowadays, calculations based on superpositions of elementary solutions (e.g. sources, doublets) require minimal computational power, and the conformal mapping's usefulness is restricted to special cases with analytical solutions (e.g. the Joukowski aerofoils). In the rest of this section, then, we shall only consider methods that are applicable to general section geometries. These are:

- numerical algorithms; (2.3)

- thin aerofoil theory; (2.4)

- the lumped parameter model (2.5)

2.3 Numerical Algorithms

2.3.1 The vortex sheet representation

The idea of using superpositions of elementary potential flow solutions to build up a field that describes flow over a body was introduced in the Incompressible Flow lectures. Numerical algorithms using this approach are known as 'panel methods'. Given a body geometry, a set of elements with unknown strengths is placed on the surface, and the strengths are then found by applying the boundary condition of zero normal velocity there.

This brief description begs the obvious question: how does one choose the set of elements? In fact, consideration of the general solution of Laplace's equation for the flow around a body (see, e.g., Katz and Plotkin), shows that many different choices can be made. However, a vortex sheet on the aerofoil surface is a particularly nice one, for reasons that will be explained subsequently.

First, we recall the definition of a vortex sheet. It is a line of concentrated vorticity whose strength gives its circulation per unit length (Figure 7). The contribution of an elemental length δl to the flow stream function is thus simply that of a point vortex, i.e.

$$\delta \psi = -\frac{\gamma(l)\delta l}{2\pi} \log r_l \tag{7}$$

and the overall stream function due to the sheet follows by integrating this expression from $l = l_0$ to l_1.
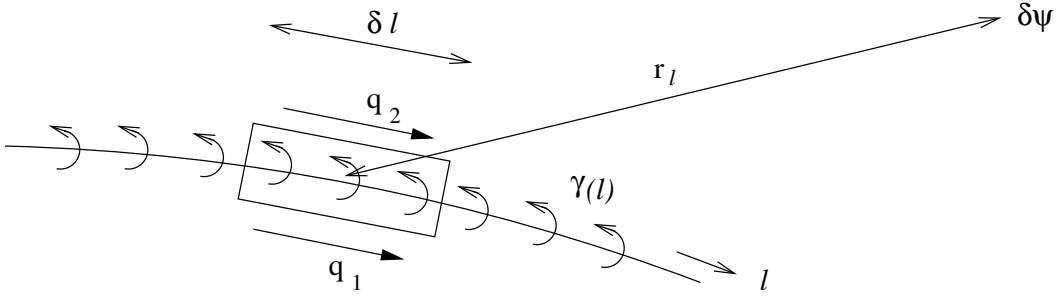
Figure 7: A vortex sheet, with circulation per unit length γ

Thus, given a discretised representation of the vortex sheet strength, say in terms of N values $\gamma_1, \gamma_2 \cdots \gamma_N$, we can derive the flow field as a linear function of the γ_is. The zero normal flow condition at the aerofoil surface will give us $(N-1)$ independent equations linking the γ_is, and the N'th is provided by the Kutta condition. The N simultaneous equations can then be solved to find the vortex sheet strength.

To find the surface velocities, and hence pressures (via Bernoulli), one could sum up the free-stream and vortex sheet contributions at each point. However, there is an extremely useful short-cut that renders this calculation unnecessary. We shall show that:

(i) if the interior of the aerofoil is occupied by fluid, then that fluid is stationary;

(ii) the tangential velocity jump across the vortex sheet is equal to its strength, γ; and therefore:

(iii) **the surface velocity at any point is equal to the vortex sheet strength there**.

There is no vorticity inside the aerofoil contour, so

(i) the interior fluid also satisfies Laplace's equation:

$$\nabla^2 \psi = 0 \tag{8}$$

subject to the boundary condition

$$\psi = \text{constant} = \psi_0 \tag{9}$$

on the underside of the vortex sheet. Now some very fine mathematical minds have proved the solution to Laplace's equation inside a closed contour, with prescribed values on that contour, is unique. This means that, if I can find *a* solution by inspection, it must be *the* solution. The obvious result is $\psi = \psi_0$ throughout the interior region, which is therefore stationary. This makes intuitive sense; a bounded region of fluid without sources, vortices or other singularities must surely be at rest.

(ii) Consider the rectangular contour shown in Figure 7. The circulation around this contour can be evaluated directly, with result

$$\delta\Gamma = \delta l \left[q_1 - q_2 \right], \tag{10}$$

or via Stokes' theorem:

$$\delta\Gamma = \gamma \delta l \tag{11}$$

Comparison of these two expressions shows that **the jump in tangential velocity across a vortex sheet is equal to its strength**.

(iii) Since the flow velocity inside the vortex sheet is zero, that outside is the same as the jump across the sheet; i.e. **the surface flow velocity is equal to the vortex sheet strength**. This means that the pressures can be immediately calculated (via Bernoulli) from the solution for the vortex sheet strength.

2.3.2 Physical interpretation of the vortex sheet representation

(a) The vortex sheet as a model for the boundary layer
The potential flow solution is required only to satisfy the boundary condition of zero normal velocity at the body surface. We justify its relevance to the real flow by appeal to the existence of a boundary layer between the true, no-slip, boundary condition and the non-zero tangential velocity in the potential flow. However, we have now shown that the vortex sheet representation of the potential flow solution does actually satisfy the no-slip condition on the inside of the sheet. It is therefore tempting to identify the vortex sheet with the boundary layer.

To confirm the legitimacy of this idea, we need to show that the boundary layer looks like a vortex sheet in mathematical terms, i.e. that its circulation per unit length is equal to the velocity jump across it. For simplicity, we do this for a flat plate boundary layer on a surface in the x-direction, with velocity components (u, v) (Figure 8). Consider the control volume ABCD at streamwise location x. It has circulation equal to the area integral of its vorticity, i.e.

$$\Gamma_{ABCD} = \int_x^{x+\Delta x} \int_0^\delta \omega(x, y) dy dx \approx \Delta x \int_0^\delta \omega(x, y) dy. \tag{12}$$

The circulation per unit length at this point, $\gamma(x)$, is $\Gamma_{ABCD}/\Delta x$, so

$$\gamma(x) = \int_0^\delta \omega(x, y) dy \tag{13}$$

with

$$\omega(x, y) = \frac{\partial v}{\partial x} - \frac{\partial u}{\partial y} \tag{14}$$
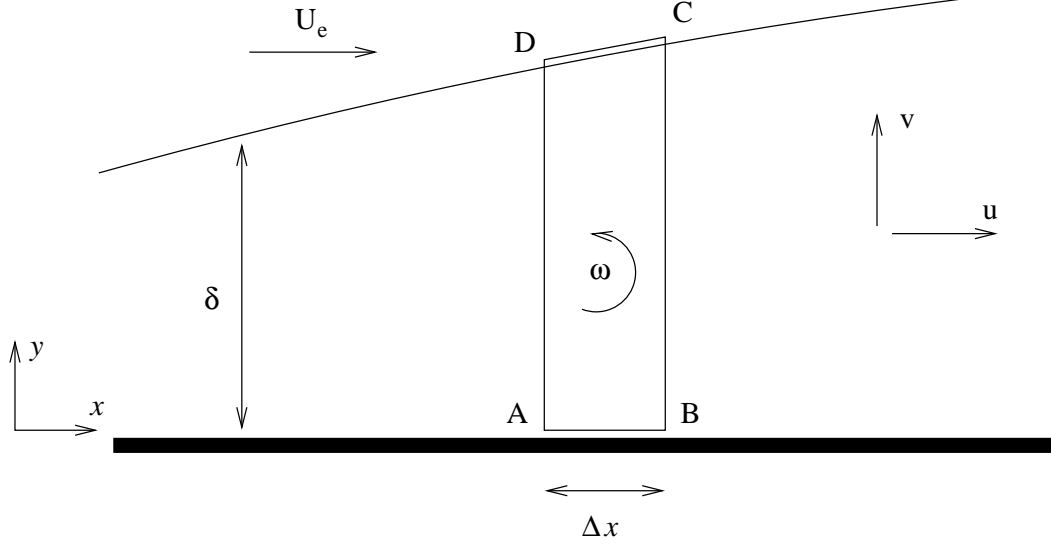
Figure 8: A flat plate boundary layer. The control volume $ABCD$ extends from the wall to the boundary-layer edge.

Now we appeal to the boundary layer approximation, which states that v is small compared to u, and that variations in the streamwise direction are small compared to those across the flow. Thus

$$\omega(x, y) \simeq -\frac{\partial u}{\partial y} \tag{15}$$

and the integral of (13) can be straightforwardly evaluated to give

$$\gamma(x) = -U_e(x) \tag{16}$$

where $U_e(x)$ is the velocity at the boundary layer edge. Since the fluid at the wall is stationary, $-U_e(x)$ is the velocity jump across the boundary layer, so (16) proves that the boundary layer can be viewed as a vortex sheet.

(b) 'Bound' vorticity

Although the vortex sheet represents the boundary layer, it is more commonly referred to as the 'bound vorticity' of the flow. The reason for this terminology is that it remains 'bound' to the aerofoil, instead of moving with the fluid. However, surely this is a contravention of the Helmholtz laws?

The solution to this paradox lies in observing that the vorticity isn't *really* stationary. In fact, it does move with the flow, but at the same time its value changes due to generation at the aerofoil surface. The contributions of these two effects exactly balance, so that the strength of the sheet at a given, fixed location remains constant.

2.3.3 The Xfoil program

A nice example of the numerical approach that we have discussed here is the Xfoil code, developed by Mark Drela at MIT, and available as freeware at http://web.mit.edu/drela/Public/web/xfoil. Initially developed about 20 years ago, it has become the *de facto* standard panel method for 2D aerofoil calculations.

Nowadays, there are many more sophisticated CFD codes available than Xfoil. Nonetheless, these codes would struggle to match Xfoil's accuracy for 2D aerofoil flows, and would consume vastly more computational resources in doing so. This is a good example of the benefits that can accrue from using conceptual models to simplify a complex physical problem before turning that problem over to the computer.

Example: Stream function for constant-strength vortex panel

Example (cont'd)

2.4 Thin Aerofoil Theory

Although a 2D panel method, coupled with a boundary layer solver, achieves good accuracy in predicting aerofoil characteristics, such a calculation still gives us little insight into the links between aerofoil geometry and performance. We are thus motivated to develop a simpler theory, which allows us to make further analytical progress. This theory is based on the observation that well-designed and effective aerofoils have small thickness-to-chord ratios, and operate at small angles of attack (e.g. $10°$ in radians is 0.17). We therefore postulate that the perturbations to the flow are small in comparison to the free-stream, and simplify the potential flow solution on this basis.

2.4.1 The approximate potential flow problem

Consider the exact boundary conditions for the flow past the aerofoil shown in Figure 9. These are simply the tangency conditions on the upper and lower surfaces:

$$\frac{v}{u}\Big|_{y=y_u} = \frac{dy_u}{dx} \quad , \quad \frac{v}{u}\Big|_{y=y_l} = \frac{dy_l}{dx}. \tag{17}$$

Now, if we assume small perturbation flow, we can write (17) in a form which allows us to superpose separate aerofoil solutions. The advantages of this simplification are best seen by working through the method.
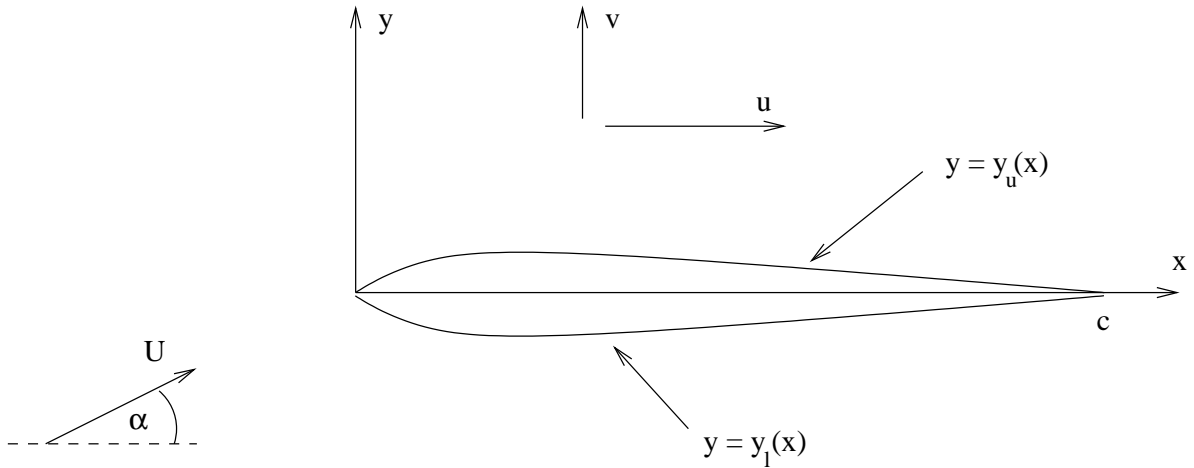
Figure 9: Nomenclature for thin aerofoil. The aerofoil, of chord c, lies on the x axis, and the oncoming flow is at incidence α.

We write the flow in terms of the free-stream plus a perturbation:

$$u = U\cos\alpha + u' \quad , \quad v = U\sin\alpha + v', \tag{18}$$

where u' and v' are assumed small compared to U. Corresponding to this hypothesis is the requirement that α is small, i.e. $\cos\alpha \simeq 1$, $\sin\alpha \simeq \alpha$. Our upper surface boundary condition becomes

$$\frac{dy_u}{dx} \simeq \frac{U\alpha + v'}{U + u'} \simeq \frac{U\alpha + v'}{U}\left(1 - \frac{u'}{U}\right) \simeq \alpha + \frac{v'}{U}. \tag{19}$$

Similarly, on the lower surface,

$$\alpha + \frac{v'}{U} \simeq \frac{dy_l}{dx}. \tag{20}$$

Now we have simpler boundary conditions, but it's still difficult to make analytical progress while they have to be applied on the aerofoil surface. Fortunately, it turns out that we can actually apply them on the $x-$axis. The justification for this is that v' can be expressed as a Taylor series, e.g.

$$v'\big|_{y=y_u} \simeq v'\big|_{y=0} + y_u \left.\frac{\partial v'}{\partial y}\right|_{y=0} + \dots, \tag{21}$$

where our requirement that the aerofoil is thin means that the first term dominates. Our boundary conditions thus become:

$$\alpha + \frac{v'}{U}\bigg|_{y=0^+} = \frac{dy_u}{dx} \quad , \quad \alpha + \frac{v'}{U}\bigg|_{y=0^-} = \frac{dy_l}{dx}. \tag{22}$$

Note that this implies (in general) a discontinuous velocity field as one crosses the x axis, hence the need to specify whether we are (just) above ($y = 0^+$) or below ($y = 0^-$) it. Also, in writing the Taylor series (21), we assumed that the velocity was continuous between $y = 0^+$ and $y = y_u$. This means that any elementary solutions that we use to represent the potential flow must lie on the x-axis. We have effectively squashed the aerofoil into the flat plate between $x = 0$ and $x = c$.

Once we have a solution for the potential flow, we will want to work out the corresponding pressure. As with the full potential solution, this follows from Bernoulli's equation:

$$p + \frac{1}{2}\rho\left[(U + u')^2 + (U\alpha + v')^2\right] = p_\infty + \frac{1}{2}\rho U^2, \tag{23}$$

where p_∞ is the pressure far from the aerofoil. Within the terms of our approximation, however, we have

$$(U + u')^2 + (U\alpha + v')^2 \simeq U^2 + 2Uu' \tag{24}$$

and hence the pressure coefficient has the simple form

$$c_p = \frac{p - p_\infty}{\frac{1}{2}\rho U^2} = -2\frac{u'}{U}. \tag{25}$$

The linear dependence of pressure on the perturbation velocity means that the thin aerofoil approximation is also referred to as **linearised potential flow**.

2.4.2 Solution for the linearised potential flow

(a) The component problems
We can use the linearity of the boundary conditions to split the flow into three components, associated with angle of attack, camber and thickness. To do this, we express the aerofoil geometry in camber-line/thickness form. The camber-line is defined as the average of the upper and lower surfaces:

$$y_c = \frac{y_u + y_l}{2} \tag{26}$$

and the thickness as their separation:

$$t = y_u - y_l. \tag{27}$$

Hence, we have $y_u = y_c + t/2$, $y_l = y_c - t/2$, and our boundary conditions (22) become

$$\alpha + \left.\frac{v'}{U}\right|_{y=0^+} = \frac{dy_c}{dx} + \frac{1}{2}\frac{dt}{dx} \quad , \quad \alpha + \left.\frac{v'}{U}\right|_{y=0^-} = \frac{dy_c}{dx} - \frac{1}{2}\frac{dt}{dx}. \tag{28}$$

We can thus split our problem into the superposition of three solutions:

(i) the incidence flow, which satisfies

$$\left.\frac{v'}{U}\right|_{y=0} = -\alpha \quad ; \tag{29}$$

(ii) the camber flow, which satisfies

$$\left.\frac{v'}{U}\right|_{y=0} = \frac{dy_c}{dx} \quad ; \tag{30}$$

(iii) the thickness flow, which satisfies

$$\left.\frac{v'}{U}\right|_{y=0^+} = \frac{1}{2}\frac{dt}{dx} \quad , \quad \left.\frac{v'}{U}\right|_{y=0^-} = -\frac{1}{2}\frac{dt}{dx}. \tag{31}$$

These three problems are shown schematically in Figure 10.
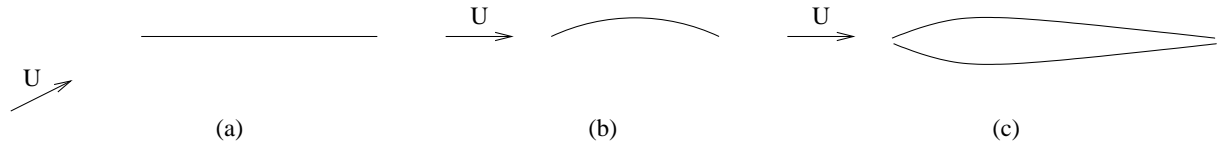
Figure 10: The component problems of thin aerofoil theory: (a) the incidence flow; (b) the camber flow; (c) the thickness flow.

(b) The flat plate revisited

The incidence flow shown in Figure 10 is one you have already encountered. In the Incompressible Flow lectures it was shown that the flow on the surface of a cylinder of radius a (Figure 11) with circulation Γ is given by

$$(u - iv)_z = Ue^{-i\alpha} - Ue^{i(\alpha - 2\theta)} - \frac{i\Gamma}{2\pi a}e^{-i\theta} \tag{32}$$

and that the cylinder could be mapped to a flat plate of length $4a$ by the conformal transformation

$$\zeta = z + \frac{a^2}{z}. \tag{33}$$

In order to satisfy the Kutta condition at the end of the plate, the cylinder flow must have a stagnation point at $\theta = 0$, and this specifies $\Gamma = -4\pi aU \sin\alpha$. The surface flow velocity (32) is thus

$$\begin{aligned}
(u - iv)_z &= Ue^{-i\theta}\left[e^{i(\theta - \alpha)} - e^{-i(\theta - \alpha)} + 2i\sin\alpha\right] \\
&= 2iUe^{-i\theta}\left[\sin(\theta - \alpha) + \sin\alpha\right]
\end{aligned} \tag{34}$$

18

Figure 11: Geometry for the formula for potential flow past a cylinder.
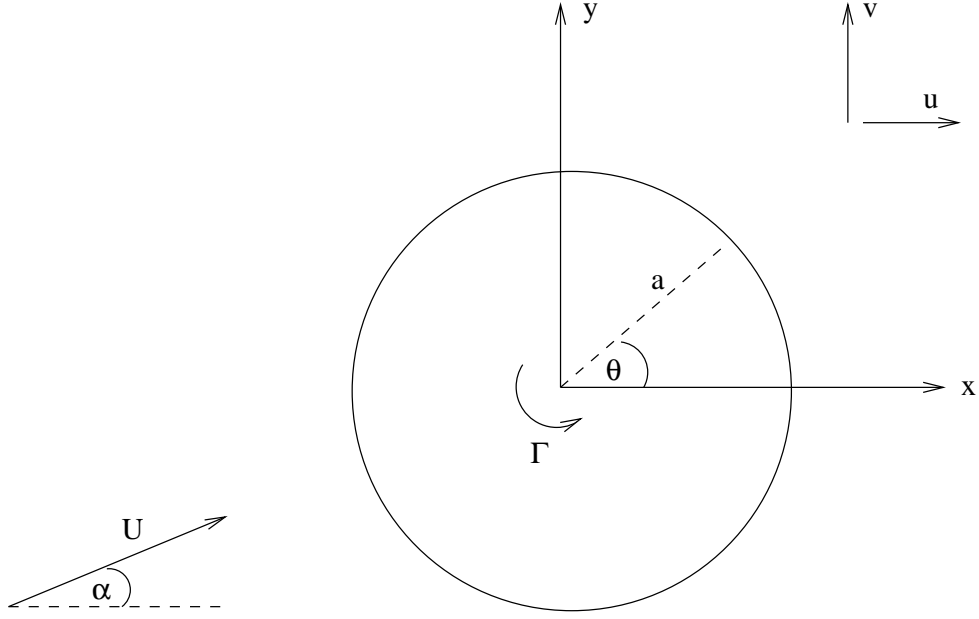
Now recall that the flow in the ζ (plate)-plane is linked to that in the z-plane by the derivative of the z-ζ transformation:

$$(u - iv)_\zeta = \frac{(u - iv)_z}{d\zeta/dz}. \tag{35}$$

On the surface of the cylinder, $z = ae^{i\theta}$, so

$$\frac{d\zeta}{dz} = 1 - \frac{a^2}{z^2} = 1 - e^{-i2\theta} = e^{-i\theta} 2i \sin\theta \tag{36}$$

and therefore the velocity on the surface of the plate is given by

$$(u - iv)_\zeta = U \frac{\sin(\theta - \alpha) + \sin\alpha}{\sin\theta}. \tag{37}$$

This is the exact potential solution, valid for any α. To find its linearised form, we just need to note that, for small α, $\sin\alpha \simeq \alpha$ and

$$\sin(\theta - \alpha) = \sin\theta\cos\alpha - \cos\theta\sin\alpha \simeq \sin\theta - \alpha\cos\theta, \tag{38}$$

so that (37) becomes

$$(u - iv)_\zeta = U \left[1 + \alpha \frac{1 - \cos\theta}{\sin\theta} \right]. \tag{39}$$

Finally, we need to shift and scale the plate so that it runs from $x = 0$ to $x = c$ instead of $-2a$ to $2a$. This is achieved by writing

$$x = c \frac{\text{Re}(\zeta) + 2a}{4a} = \frac{c}{2}(\cos\theta + 1) \tag{40}$$

Note that:

(i) this solution has the expected form $u = U + u'$, with $u' << U$ (except at $\theta = \pi$);

(ii) $v = 0$, i.e. like (37) it satisfies the required boundary condition;

(iii) there is a discontinuity in velocity across the plate. Consider the perturbation velocity at a point $x_\phi = (c/2)[1 + \cos\phi]$, with $0 < \phi < \pi$. On the upper surface,

$$u' = U\alpha \frac{1 - \cos\phi}{\sin\phi}. \tag{41}$$

The corresponding point on the lower surface is at $\theta = -\phi$ (remember that $\cos(-\phi) = \cos\phi$), and here

$$u' = -U\alpha \frac{1 - \cos\phi}{\sin\phi}. \tag{42}$$

The flat plate solution thus corresponds to a vortex sheet of strength

$$\gamma(\phi) = -2U\alpha \frac{1 - \cos\phi}{\sin\phi} \tag{43}$$

with

$$\phi = \cos^{-1}\left[\frac{2x}{c} - 1\right] \quad, \quad 0 \le \phi \le \pi. \tag{44}$$

We can think of $\gamma(\phi)$ as being the result of combining the bound vortex sheets on the upper and lower surfaces of the aerofoil. Note that it is zero at the trailing edge, as we would expect from the Kutta condition, but singular at the leading edge, like the exact solution. This unphysical result is due to the inadequacy of the flat plate model at the leading edge. It can be fixed up elegantly with the mathematical technique of 'matched asymptotic expansions', but the results don't add greatly to the deduction that one is likely to find high, albeit not infinite, velocities around the nose of a thin aerofoil.

(c) The camber component.

We expect that camber will be associated with some degree of lift or, equivalently, circulation. This means we should be able to represent the associated flow with a vortex sheet, as for the flat plate. The perturbation velocity v' associated with this sheet can be found by integrating its elemental contributions. In polar coordinates centred on a given element, the associated velocity is tangential, with magnitude $(\gamma\delta x/2\pi r)$, as shown in Figure 12. On the x-axis this component is purely vertical, so

$$v'(X, 0) = \int_0^c \frac{\gamma(x)}{2\pi(X - x)}dx \tag{45}$$

Equivalently, in terms of our angular variable ϕ (see (44)), we have

$$x = \frac{c}{2}(1 + \cos\phi), \tag{46}$$

$$dx = -\frac{c}{2}\sin\phi d\phi \tag{47}$$

and hence

$$v'\big|_{y=0} = \frac{1}{2\pi}\int_\pi^0 \frac{-\gamma(\phi)\sin\phi}{\cos\theta - \cos\phi}d\phi = \frac{1}{2\pi}\int_0^\pi \frac{-\gamma(\phi)\sin\phi}{\cos\phi - \cos\theta}d\phi \tag{48}$$

where

$$\theta = \cos^{-1}\left[\frac{2X}{c} - 1\right]. \tag{49}$$

The boundary condition for the camber problem, (30), thus becomes

$$\frac{1}{2\pi U}\int_0^\pi \frac{-\gamma(\phi)\sin\phi}{\cos\phi - \cos\theta}d\phi = \frac{dy_c}{dx}. \tag{50}$$

There is no general analytical solution to this integral equation. To solve it, we have to assume a certain form for γ, with unknown parameters, and then substitute this form into (50) to obtain equations defining the parameters.
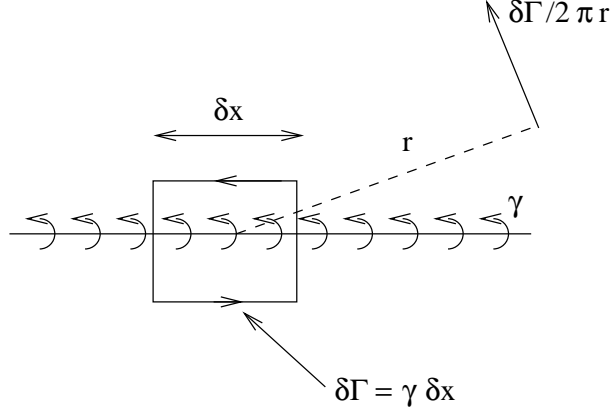

Figure 12: The contribution of an element of a vortex sheet to the flow field.

What form should we assume? We can again expect infinite loading at our unrealistically thin leading edge representation. Equally, the Kutta condition must still be satisfied at the trailing edge. A possible form for the vortex sheet thus consists of a proportion of the flat plate solution combined with a sum of Fourier components:

$$\gamma(\phi) = -U\left[g_0 \frac{1 - \cos\phi}{\sin\phi} + \sum_{n=1}^\infty g_n \sin n\phi\right]. \tag{51}$$

Note that there's no *a priori* guarantee that the solution is of this form; we just have to wait and see whether the analysis works with this assumption.

Substituting (51) into (50) leads to the equation

$$
\begin{aligned}
\frac{dy_c}{dx}\bigg|_\theta &= \frac{1}{2\pi}\int_0^\pi \left\{g_0\frac{1-\cos\phi}{\sin\phi} + \sum_{n=1}^\infty g_n \sin n\phi\right\}\frac{\sin\phi}{\cos\phi - \cos\theta}d\phi \\
&= \frac{1}{2\pi}\int_0^\pi \left\{g_0\frac{1-\cos\phi}{\cos\phi - \cos\theta} + \frac{1}{2}\sum_{n=1}^\infty g_n \frac{\cos(n-1)\phi - \cos(n+1)\phi}{\cos\phi - \cos\theta}\right\}d\phi \\
&= \frac{g_0}{2\pi}(I_0 - I_1) + \sum_{n=1}^\infty \frac{g_n}{4\pi}(I_{n-1} - I_{n+1}),
\end{aligned} \tag{52}
$$

where

$$I_n = \int_0^\pi \frac{\cos n\phi}{\cos\phi - \cos\theta}d\phi. \tag{53}$$

21

The solution for I_n is investigated in Appendix A, where we show that

$$I_n = \pi \frac{\sin n\theta}{\sin \theta} \tag{54}$$

and also that

$$I_{n-1} - I_{n+1} = -2\pi \cos n\theta. \tag{55}$$

Equation (52) becomes

$$g_0 + \sum_{n=1}^{\infty} g_n \cos n\theta = -2\frac{dy_c}{dx}\bigg|_\theta . \tag{56}$$

We can recognise this as a half-range Fourier series representation of the camber-line gradient (because $0 \leq \theta \leq \pi$). The coefficients follow from the standard Fourier series formula:

$$g_0 = \frac{1}{\pi} \int_0^\pi \left(-2\frac{dy_c}{dx}\right) d\theta,$$

$$g_m = \frac{2}{\pi} \int_0^\pi \left(-2\frac{dy_c}{dx}\right) \cos m\theta d\theta, \quad m = 1, 2\ldots \tag{57}$$

Thus, via (51) and (57) we have the required solution for the camber problem.

Example: Parabolic camber

Example (cont'd)

(d) Implications of the incidence and camber solutions

The symmetry of the thickness problem immediately implies that there will be no lifting contributions from the associated pressures. We can therefore already examine the lift and pitching moment predicted by thin aerofoil theory.

First note that the pressure difference between lower and upper surfaces follows from (25) as

$$p_l - p_u = \frac{1}{2}\rho U^2 \left[-\frac{2u_l'}{U} + \frac{2u_u'}{U} \right] = -\rho U \gamma. \tag{58}$$

The lift is thus

$$\int_0^c (p_l - p_u)dx = -\rho U \int_0^c \gamma dx \tag{59}$$

as we could have shown via a direct appeal to the Kutta-Joukowski theorem. For a cambered aerofoil at incidence, we have (from (43) and (51))

$$\gamma = -U \left\{ (2\alpha + g_0)\frac{1 - \cos\phi}{\sin\phi} + \sum_{n=1}^{\infty} g_n \sin n\phi \right\} \tag{60}$$

and (from (47)) $dx = -(c/2)\sin\phi d\phi$. The lift coefficient is found by non-dimensionalising (59) on $\frac{1}{2}\rho U^2 c$, giving

$$
\begin{aligned}
c_l &= \frac{-\rho U}{\frac{1}{2}\rho U^2 c} \int_{\pi}^{0} -U \left\{ (2\alpha + g_0)\frac{1 - \cos\phi}{\sin\phi} + \sum_{n=1}^{\infty} g_n \sin n\phi \right\} \left(-\frac{c}{2} \right) \sin\phi d\phi \\
&= (2\alpha + g_0) \int_0^{\pi} (1 - \cos\phi)d\phi + g_1 \int_0^{\pi} \sin^2\phi d\phi
\end{aligned} \tag{61}
$$

since

$$\int_0^{\pi} \sin m\phi \sin n\phi d\phi = 0 \tag{62}$$

for $m \neq n$. The integrals in (61) are straightforward, giving

$$c_l = 2\pi\alpha + \pi \left[g_0 + \frac{g_1}{2} \right]. \tag{63}$$

Notes:

(i) Unsurprisingly, given the separation between incidence and camber effects that is possible in the linear solution, the lift-curve slope is that of the flat plate: 2π.

(ii) The camber contribution comes from the first two terms in the Fourier series for $-2(dy_c/dx)$. We can obtain further insight into this contribution by re-writing it in terms of an integral over x. First

$$g_0 + \frac{g_1}{2} = \frac{1}{\pi} \int_0^{\pi} \left(-2\frac{dy_c}{dx} \right)(1 + \cos\theta)d\theta, \tag{64}$$

from (57). Now $x = (c/2)(1 + \cos\theta)$, so $dx = -(c/2)\sin\theta d\theta$ and

$$g_0 + \frac{g_1}{2} = \frac{1}{\pi} \cdot \frac{2}{c} \int_0^c \left(-2 \frac{dy_c}{dx} \right) \frac{1 + \cos\theta}{\sin\theta} dx \qquad (65)$$

Now we can also express x in terms of $\cos(\frac{1}{2}\theta)$:

$$x = c \frac{1 + \cos\theta}{2} = c \cos^2\left(\frac{1}{2}\theta \right), \qquad (66)$$

which means $\sin^2(\frac{1}{2}\theta) = 1 - x/c$. Thus

$$\frac{1 + \cos\theta}{\sin\theta} = \frac{2\cos^2(\frac{1}{2}\theta)}{2\sin(\frac{1}{2}\theta)\cos(\frac{1}{2}\theta)} = \frac{\cos(\frac{1}{2}\theta)}{\sin(\frac{1}{2}\theta)} = \sqrt{\frac{x/c}{1 - x/c}}. \qquad (67)$$

So, finally,

$$g_0 + \frac{g_1}{2} = \frac{2}{\pi c} \int_0^c \left(-2 \frac{dy_c}{dx} \right) \sqrt{\frac{x/c}{1 - x/c}} dx. \qquad (68)$$

This tells us that the contribution of camber to lift depends on the camber-line gradient, weighted by $\sqrt{(x/c)/(1 - x/c)}$. This function is plotted in Figure 13, showing that the influence of camber is greatest towards the rear of the aerofoil. An aerofoil with positive camber will have positive dy_c/dx near the nose and negative dy_c/dx near the trailing edge. The extra weighting at the rear will make $g_0 + g_1/2$ positive, so (referring back to (63)) we see that positive camber corresponds to a positive lift contribution, as we intuitively expect. Note also that the rearward weighting of camber-line influence explains why control surfaces on aircraft (and birds!) are at the trailing edge.
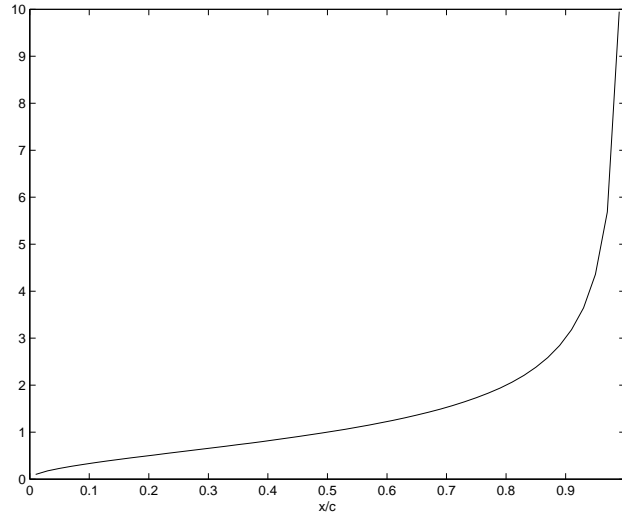

Figure 13: Weighting function for the integral giving camber-line contribution to lift.

(iii) The lift coefficient of the cambered aerofoil can alternatively be expressed as

$$c_l = 2\pi(\alpha - \alpha_0), \qquad (69)$$

where

$$\alpha_0 = -\left(\frac{g_0}{2} + \frac{g_1}{4}\right) \tag{70}$$

is the angle at which the aerofoil produces zero lift. For the positive camber case, where $g_0 + g_1/2 > 0$, it will be negative.

The aerofoil pitching moment (anti-clockwise positive, about the leading edge) is given by the integral of elemental lift contributions multiplied by their moment arms, i.e.

$$M = \int_0^c (p_l - p_u)x\,dx. \tag{71}$$

The pitching moment coefficient, c_m, is defined as the non-dimensionalisation of M by $\frac{1}{2}\rho U^2 c^2$, and (from (58)) $p_l - p_u = -\rho U \gamma$, so

$$c_m = \frac{2}{c^2}\int_0^c -\frac{\gamma}{U}x\,dx. \tag{72}$$

Substituting (60) for γ and using $x = (c/2)(1 + \cos\phi)$ give

$$\begin{aligned}
c_m &= \frac{1}{2}\int_0^\pi \left\{(2\alpha + g_0)\frac{1 - \cos\phi}{\sin\phi} + \sum_{n=1}^\infty g_n \sin n\phi\right\}(1 + \cos\phi)\sin\phi\,d\phi \\
&= \frac{(2\alpha + g_0)}{2}\int_0^\pi \sin^2\phi\,d\phi + \sum_{n=1}^\infty \frac{g_n}{2}\int_0^\pi \sin n\phi\left(\sin\phi + \frac{1}{2}\sin 2\phi\right)d\phi \\
&= \frac{\pi}{4}(2\alpha + g_0) + \frac{\pi}{4}g_1 + \frac{\pi}{8}g_2 \\
&= \frac{\pi}{2}\left(\alpha + \frac{g_0}{2} + \frac{g_1}{4}\right) + \frac{\pi}{8}(g_1 + g_2).
\end{aligned} \tag{73}$$

The reason for writing the result in this way is that the first bracket is the term $(\alpha - \alpha_0)$, so the pitching moment coefficient can alternatively be written as

$$c_m = \frac{1}{4}c_l + c_{m0} \tag{74}$$

where

$$c_{m0} = \frac{\pi}{8}(g_1 + g_2). \tag{75}$$

This implies that the pressure forces on the aerofoil can be represented by a force and moment combination acting at the quarter-chord point, $x = c/4$, as shown in Figure 14. Furthermore, the moment is independent of the angle of attack. Equivalently, we can say that the *additional* lift due to incidence change effectively acts at the quarter-chord point. This prediction is nicely confirmed by experiment; for example, Figure 15 shows measurements on a NACA 4412 aerofoil section. The pitching moment is measured about the quarter-chord point, so we expect to see only the constant component. The pitching moment coefficient results are the symbols around -0.4; as expected, the moment is independent of incidence in the range where the lift coefficient curve is linear.

It might seem more natural to represent the effect of the distributed pressures as a force only, located at the point about which the pressures have zero moment. This alternative representation is shown in Figure 16; the lift is now said to act at the **centre of pressure**. Since both representations are equivalent, we have (taking moments about $x = 0$):

26

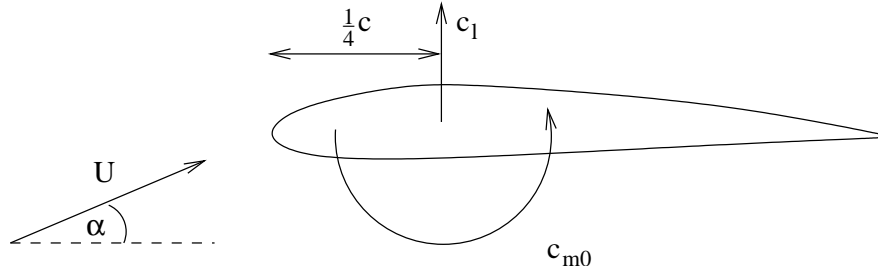Figure 14: The pressures acting on a thin aerofoil are equivalent to a lift force and an incidence-independent moment at the quarter-chord point.
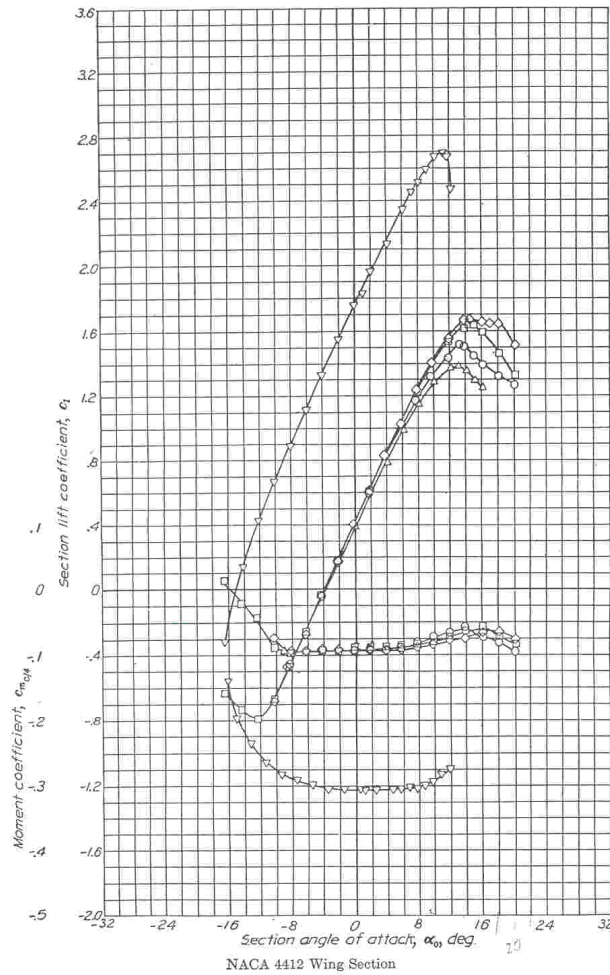

NACA 4412 Wing Section

Figure 15: Measured lift and pitching moment coefficients on a NACA 4412 section (Reynolds numbers $3 \times 10^6 - 9 \times 10^6$). Lift coefficients are positive, moment coefficients negative. The displaced curves show the effect of a deflected flap.

$$
\begin{aligned}
c_l \frac{x_c}{c} &= \frac{1}{4} c_l + c_{m0} \\
\frac{x_c}{c} &= \frac{1}{4} + \frac{c_{m0}}{c_l}
\end{aligned}
\tag{76}
$$

We see that the centre of pressure is coincident with the quarter-chord point only in the special case with $c_{m0} = 0$. Otherwise, it differs, depending on the camber-line shape and, worse still, on the incidence. For small lift coefficients, it takes leave of the aerofoil altogether and heads off to infinity.
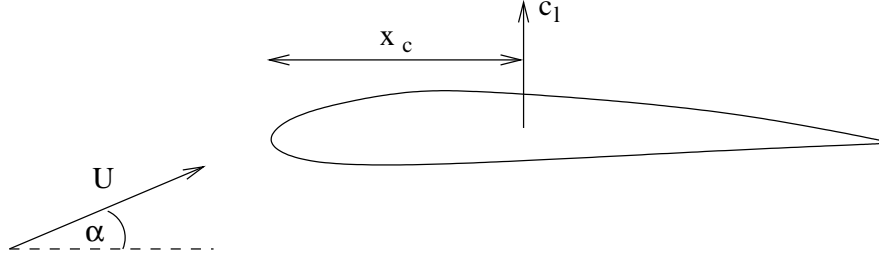

Figure 16: Alternative representation of the pressures acting on a thin aerofoil, consisting of a (lift) force only acting at the centre of pressure, x_c.

The footloose nature of the centre of pressure means that it is not generally a helpful concept. On the other hand, the observation that the quarter-chord pitching moment remains constant *is* useful, and can be extended to the aircraft as a whole. It is particularly important in the theory of aircraft balance and stability.

(e) The thickness component
We now consider the third and final component of thin aerofoil theory; the flow due to thickness. Recall that the corresponding linearised boundary conditions are:

$$
\left. \frac{v'}{U} \right|_{y=0^+} = \frac{1}{2} \frac{dt}{dx} \quad , \quad \left. \frac{v'}{U} \right|_{y=0^-} = -\frac{1}{2} \frac{dt}{dx},
\tag{77}
$$

implying that the velocity field is symmetrical about the x-axis. We thus postulate that the perturbation flow can be represented by a line source distribution. To see why this is reasonable, consider the elemental portion $\sigma(x)\delta x$ of the line source shown in Figure 17. The principle of mass conservation applied to the (infinitesimally-thin) control volume surrounding it gives

$$
2q\delta x = \sigma(x)\delta x,
\tag{78}
$$

where q is the velocity normal to the line. Therefore, a source distribution

$$
\sigma(x) = U \frac{dt}{dx}
\tag{79}
$$

will satisfy the required boundary condition.

To find the flow field, we superpose the elemental source contributions via integration. As our main interest is in the surface velocity (and hence pressure), we have

$$
u'(x, 0) = \int_0^c \frac{\sigma(x')}{2\pi(x - x')} dx'.
\tag{80}
$$

We can again make useful progress via a Fourier series approach. If, as previously
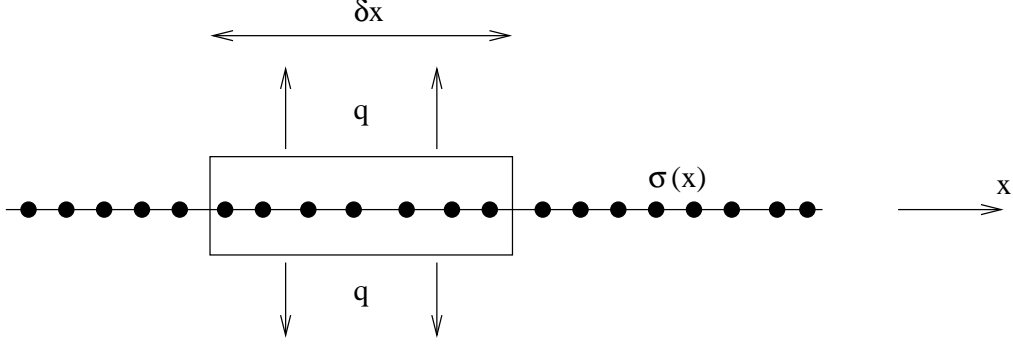
28

Figure 17: A line source, of strength σ, and the control volume used to link σ to the normal velocity component, q.

$$x' = \frac{c}{2}(1 + \cos\phi), \tag{81}$$

then we can write the thickness distribution as the Fourier series

$$t = c\sum_{n=1}^{\infty} \tau_n \sin n\phi. \tag{82}$$

The source strength distribution $\sigma(x')$ follows from (79) as:

$$\sigma(x') = Uc\sum_{n=1}^{\infty} n\tau_n \cos n\phi \frac{d\phi}{dx'} = Uc\frac{\sum_{n=1}^{\infty} n\tau_n \cos n\phi}{(dx'/d\phi)}. \tag{83}$$

Now we express x in terms of angular coordinates; $x = c(1 + \cos\theta)/2$, and note that $dx' = (dx'/d\phi)d\phi$, so (80) becomes

$$u'(x,0) = \frac{U}{\pi}\sum_{n=1}^{\infty} n\tau_n \int_0^\pi \frac{\cos n\phi}{\cos\phi - \cos\theta}d\phi = U\sum_{n=1}^{\infty} n\tau_n \frac{\sin n\theta}{\sin\theta}, \tag{84}$$

using the result of (54).

To obtain a feeling for what this result tells us, consider first the case where only τ_1 is non-zero, which corresponds to the ellipse

$$t(x) = 2c\tau_1 \sqrt{\frac{x}{c}\left(1 - \frac{x}{c}\right)}. \tag{85}$$

In this case

$$u'(x,0) = U\tau_1, \tag{86}$$

which is a constant, independent of x! In reality, of course, the velocity will vary smoothly from zero at the leading edge stagnation point, and smoothly back to zero at the trailing edge stagnation point. The inability of the thin aerofoil solution to reproduce this behaviour is due to the breakdown of its assumptions near stagnation points, which *ipso facto* correspond to large departures from free-stream conditions. However, we can deduce from this approximation that the exact flow would undergo rapid accelerations near the leading edge, and correspondingly rapid decelerations near the trailing edge. (This is confirmed by inspection of the exact solution, which is shown, along with the thin aerofoil theory result, in Figure 18.) The former correspond

29

to favourable pressure gradients, and hence would be of little concern, but the adverse pressure gradients associated with the latter would be bad news for the boundary layer in a real flow. This, of course, explains the need for the 'teardrop' shapes typically adopted for streamlined bodies.
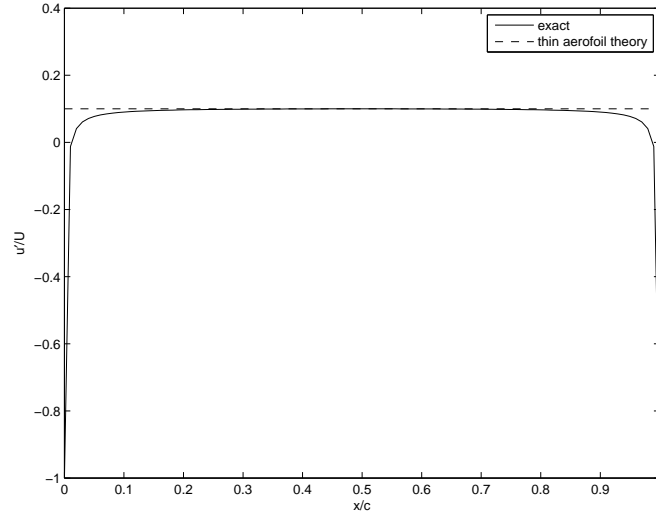
Figure 18: Exact and thin aerofoil solutions for the surface velocity on a 10% thick ellipse.

We can obtain an indication that the move towards a teardrop shape is beneficial by considering the requirement on the second term of (84) if we are to reduce the surface velocity in advance of the trailing edge. Note that

$$\frac{\sin 2\theta}{\sin \theta} = 2\cos\theta = 2\left[\frac{2x}{c} - 1\right],\tag{87}$$

from which we see that τ_2 must be negative to reduce the aft velocity. Figure 19 shows the shape obtained with $\tau_1 = 0.12$, $\tau_2 = -0.03$; although not quite a genuine teardrop, it represents a significant shift in that direction.

Figure 19: The thickness distribution obtained from (82) with $\tau_1 = 0.12$, $\tau_2 = -0.03$.

(f) The aerofoil pressure distribution

We are now in a position to combine the components of thin aerofoil theory to give the predicted pressure distribution on the aerofoil. Recall that the pressure coefficient is given by (25):
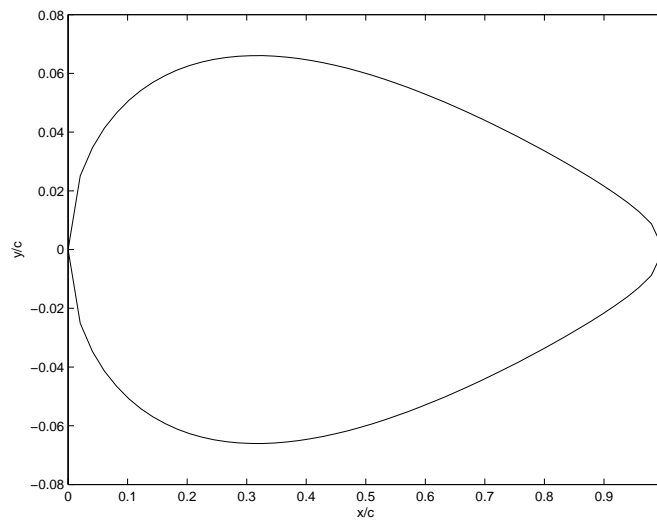
$$c_p = -\frac{2u'}{U}. \tag{88}$$

For the incidence and camber-line components, symmetry implies that $u'(y = 0^-) = -u'(y = 0^+)$, and hence that $\gamma(x) = u'(y = 0^-) - u'(y = 0^+) = -2u'(y = 0^+)$. Thus

$$c_p = \pm\frac{\gamma}{U} = \mp\left\{(2\alpha + g_0)\frac{1 - \cos\theta}{\sin\theta} + \sum_{n=1}^{\infty} g_n \sin n\theta\right\}, \tag{89}$$

from (60). (The negative and positive signs refer to the aerofoil upper and lower surfaces respectively.) This expression consists of a singular component, identical in shape to the flat plate distribution, but modified in amplitude by the camber (Figure 20(a)), and a finite component due to camber alone (Figure 20(b)). Note that both are symmetrical about the x-axis.

The form of the thickness component follows directly from (88) and (84). Since u' is positive and continuous across the x-axis, the pressure coefficient is negative, and identical on upper and lower surfaces (see Figure 20(c)).

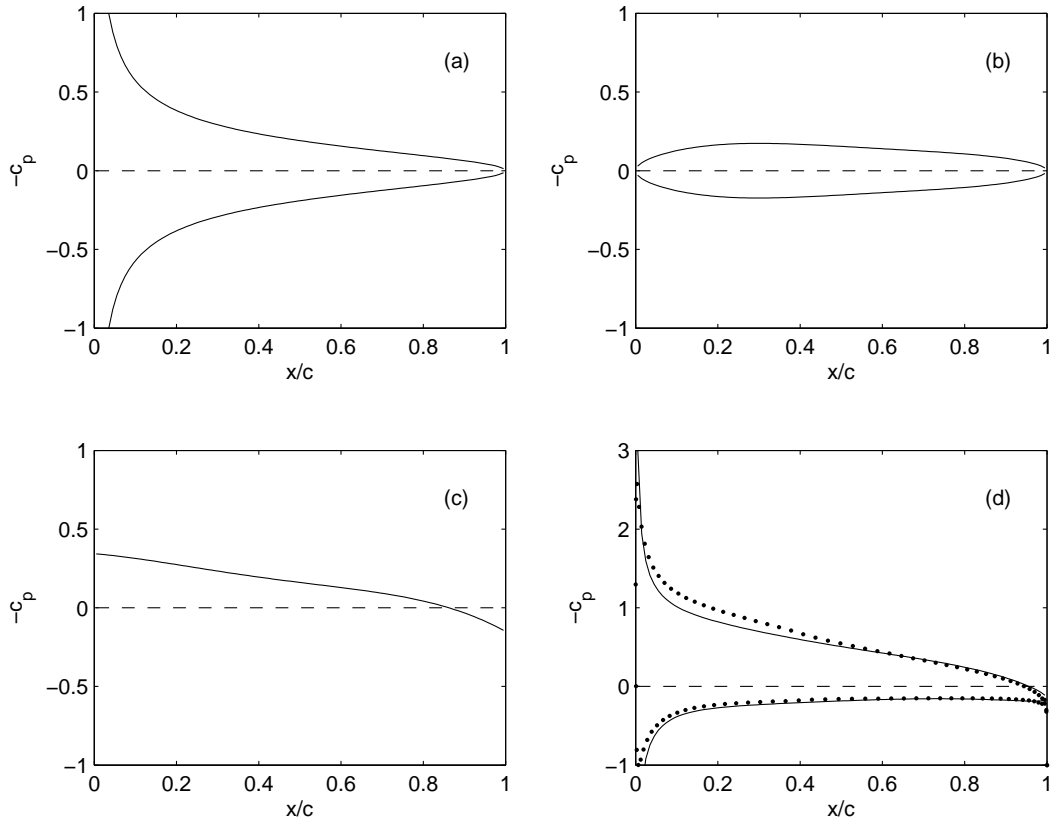Figure 20: Thin aerofoil theory pressure distributions for NACA 2409 aerofoil at 5° incidence: (a) singular component ($\alpha = 0.087, g_0 = -0.009$); (b) finite camber component ($g_1 = 0.163, g_2 = -0.028, g_3 = 0.006, g_4 = 0.004, g_5 = -0.003$); (c) thickness component ($\tau_1 = 0.0780, \tau_2 = -0.0256, \tau_3 = -0.0017, \tau_4 = -0.0013, \tau_5 = -0.0006$); (d) overall (—) and numerical solution (...).

Finally, we superpose the component pressure distributions in Figure 20(a)-(c) to give the thin aerofoil prediction for the overall distribution (Figure 20(d)). Also shown here is the exact potential flow solution for the aerofoil corresponding to the coefficient values used. At this aerofoil thickness (9%) and incidence, the thin aerofoil theory can be seen to work very well.

Notes

(i) As observed previously, the regions where the thin aerofoil solution departs significantly from the full potential result are around the stagnation points and the suction peak.

(ii) In general, a lifting aerofoil can be expected to have extended regions of adverse pressure gradient on the upper surface, and favourable pressure gradient on the lower surface. However, there will be an angle of attack where there is no contribution from the singular component, and the lift is solely associated with the finite component due to camber. In this case, pressure gradients will typically be quite small over most of the section.

(iii) The most obvious effect of thickness is to 'asymmetrise' the distribution. This makes the pressure gradient more adverse on the upper surface, and less favourable on the lower. The shift in lower surface c_p is unlikely to cause problems (although it could, if the section were *really* thick). The issue remains, however, on the upper surface, so we would conclude from thin aerofoil theory alone that thickness is inherently detrimental. In fact, thickness *does* have a beneficial effect, but *only* around the leading edge, where the theory breaks down. Qualitatively, we can argue that the decreased streamline curvature in the flow passing around the leading edge will correspond to a lower normal pressure gradient, and hence reduced suction at the surface. Thus the leading edge curvature determines the extent to which the predicted infinite suction peak is smoothed out.

(g) The 'design' incidence

In the previous section we mentioned the possibility of generating lift without having a significant suction peak, by eliminating the singular contribution shown in Figure 20(a). From (89), this requires an incidence α_d satisfying $2\alpha_d + g_0 = 0$, i.e.

$$\alpha_d = -\frac{g_0}{2} = \frac{1}{\pi}\int_0^\pi \frac{dy_c}{dx}d\theta. \tag{90}$$

Given the relatively benign pressure gradients predicted at this incidence, we can expect that the boundary layer momentum loss, and hence the drag, will be at a minimum. Nonetheless, the boundary layers will have been more 'maltreated' than those on a symmetrical aerofoil of the same thickness distribution. We thus conclude that

- **the minimum drag of a cambered aerofoil will typically be greater than that of a symmetric section of comparable thickness, but...**

- **the cambered section produces lift at its minimum drag condition**.

2.5 Lumped Parameter Models

In the incompressible flow course, it was shown that the two-dimensional potential flow far away from a lifting body can be represented to a first approximation by a vortex at the body. This is an example of a *lumped parameter model*; in this case the surface vorticity is 'lumped' into the single vortex. Such models are useful in aerodynamics when one wishes to consider interactions between multiple wings, or even aeroplanes.

The flat plate admits a very simple lumped parameter representation; since the lift acts at the quarter-chord point, we can ensure that the pitching moment is correct by placing our point vortex there, as shown in Figure 21. The force on the vortex is $\rho U \Gamma$, and thus

$$c_l = \frac{\rho U \Gamma}{\frac{1}{2}\rho U^2 c} = \frac{2\Gamma}{Uc}. \tag{91}$$

This allows us to find Γ in terms of c_l, and hence α:

$$\Gamma = \frac{Uc}{2}c_l = 2\pi \left(\frac{c}{2}\right) U\alpha. \tag{92}$$

Now, the downwash on the plate due to the vortex is:

$$\frac{\Gamma}{2\pi(x - c/4)} = U\alpha \frac{c/2}{x - c/4}, \tag{93}$$

and this is exactly equal to the upwash from the free-stream, $U\alpha$, when $x = 3c/4$, i.e. at the three-quarter chord point. Thus, although the lumped parameter model is clearly incapable of satisfying the no-flow boundary condition over the entire plate, it does so at one special place, known as the **collocation point**. This observation is central to the use of the lumped parameter model for multiple lifting surfaces, as it tells us how to account for the influence of other wings. Specifically, **the lumped parameter model for an uncambered wing consists of a point vortex at the quarter-chord, with circulation determined by the requirement that the overall downwash at three-quarter-chord is zero.**
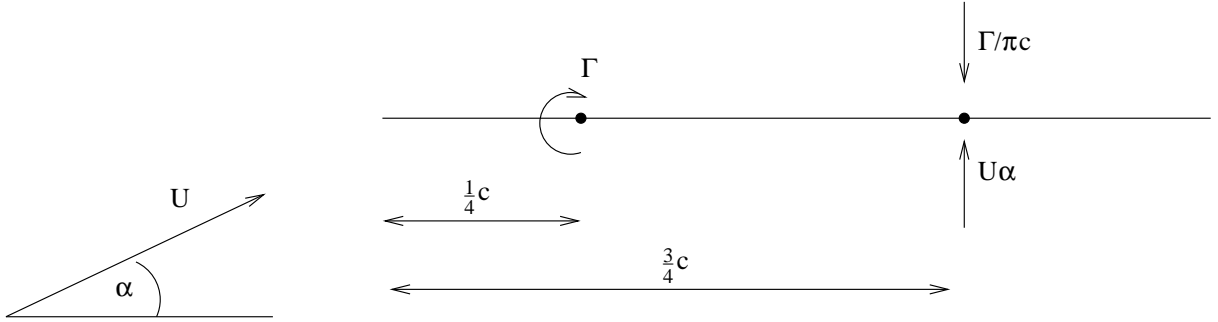

Figure 21: The lumped-parameter model of an uncambered aerofoil. The circulation of the bound vortex is determined by the requirement that its downwash cancels the vertical free-stream component at three-quarters chord.

Example: Wing near the ground

Example (cont'd)

When a wing is cambered, the lumped parameter model is less straightforward. The dependence of the centre of pressure on incidence means that we must either allow the vortex to move, or include a pitching moment in our representation. The latter is preferable and, if we again place the vortex at the quarter-chord, then the pitching moment coefficient is constant at c_{m0} (see (74)). The lift coefficient is $2\pi(\alpha - \alpha_0)$ so, from (91),

$$\Gamma = 2\pi \left(\frac{c}{2}\right) U(\alpha - \alpha_0). \tag{94}$$

This implies that the downwash due to the vortex at three-quarters chord is equal to the free-stream upwash on a surface inclined at α_0 to the horizontal (see Figure 22). We thus have to postulate an *effective* camber-line slope $dy_c/dx = \alpha_0$ at our collocation point. For a typical aerofoil, with positive camber, this effective slope is negative, as one would typically find towards the rear of such a section. It is *not*, however, necessarily equal to the true camber-line slope at three-quarter chord, and in general will not be.
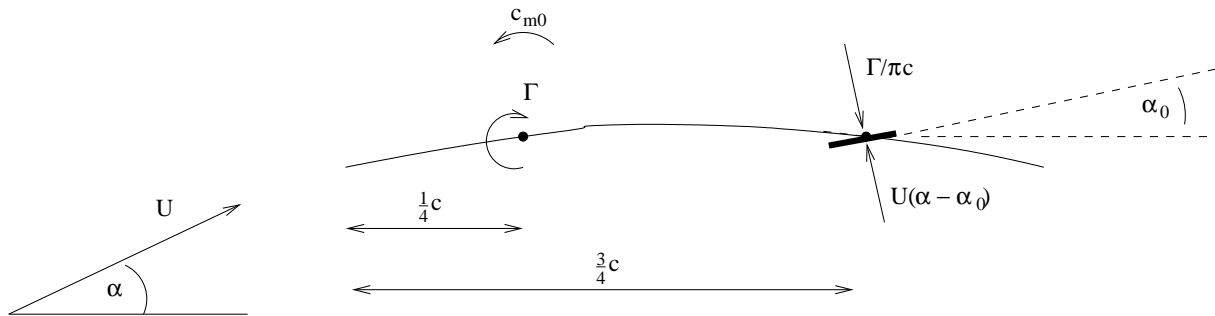

Figure 22: The lumped-parameter model of a cambered aerofoil with zero-lift angle α_0.

2.6 Viscous Effects and Stall

We conclude our discussion of two-dimensional aerofoil flow by returning to the regime where viscous effects cause fundamental departures from potential flow, i.e. stall. Although this is not the design regime, it is one that may be encountered, and the stall characteristics of an aircraft are thus crucial to its safe operation. Ideally, one would like to delay stall as long as possible, to receive advance warning as it is approached, and only to lose lift gradually if it is reached. Unfortunately, as we shall see, these requirements are not necessarily consistent with one another, or with good performance at the design point.

This section starts with a brief recap of boundary layer properties, so that we can identify where separation is most likely on an aerofoil. We then discuss **separation bubbles**, which do not *in themselves* cause a significant loss of lift, but which are important in the eventual stall behaviour of an aerofoil. Finally, stall itself is addressed.

2.6.1 Boundary layers and separation

As you have already seen earlier in the course, boundary layers come in two flavours, **laminar** and **turbulent**. In laminar boundary layers, the transport of momentum normal to the surface is via the diffusive mechanism of viscosity, which is rather weak at aerodynamic Reynolds numbers. In turbulent boundary layers, viscous diffusion is swamped by unsteady mixing, which increases in importance with distance from the wall. The difference between these physical mechanisms means that turbulent boundary layers are typically thicker than their laminar counterparts, but with a 'fuller' profile.

The key features of boundary layers from the point of view of separation are:

- separation can *only* occur in a boundary layer subject to an adverse pressure gradient;

- the effect of an adverse pressure gradient is cumulative, i.e. the longer a boundary layer is subject to such a gradient, the more likely it becomes to separate;

- laminar boundary layers, by virtue of their shallower profile, are much more prone to separation than turbulent ones;

- laminar boundary layers can transition to turbulence once their Reynolds number is high enough. *Transition can occur under any pressure field*, but is inhibited by favourable and encouraged by adverse gradients.

Note, in particular, that *transition and separation are not the same thing*; there is a world of difference between flows with attached, turbulent boundary layers and flows with large-scale unsteady separations.

Returning to the typical pressure distribution associated with an aerofoil at high incidence (Figure 2), we see that it is the upper, suction surface, that is subject to adverse pressure gradients. Two regions are especially sensitive:

- just after the suction peak, where the maximum adverse gradients are encountered. This is particularly true if the boundary layer is laminar at this point;

- towards the trailing edge, where the cumulative effect of traversing the suction surface will have significantly increased the boundary layer's tendency to separate.

We now hit an important conceptual hurdle. While the boundary layer at the suction peak may well be turbulent for large passenger aircraft at cruise conditions, it is typically not so for smaller aircraft, gliders and wings in wind tunnels. Surely, then, the laminar boundary layer should separate even at small incidence, resulting in catastrophically early stall?

In practice, such behaviour *is* observed, but only at much lower Reynolds numbers (at model aircraft scale, for example). At higher Reynolds numbers we are saved by *turbulent reattachment*. This occurs because the separated 'shear flow' is much more unstable than the attached boundary layer, so transition to turbulence occurs. The tendency of the turbulent shear layer to entrain surrounding fluid then 'sucks' it towards the aerofoil surface, where it attaches as a robust turbulent boundary layer. We have thus achieved transition, but via a *different* mechanism from the attached boundary layer. *It is important to distinguish between these two phenomena!*

2.6.2 Separation bubbles

The region of flow between separation and reattachment is known as a **separation bubble**. It is shown schematically in Figure 23. As it consists of a nearly stagnant, 'dead-water' region, the surface pressure underneath it is typically almost constant. This allows the presence of long separation bubbles to be diagnosed from surface pressure plots. Figure 24 shows an example of this, for the Göttingen 801 aerofoil. Consider first the 18° incidence case. Here laminar separation takes place shortly after the suction peak, as expected. However, at lower incidences, the laminar boundary layer survives the (less severe) adverse pressure gradients for longer, and the results show that one can find separation bubbles a significant distance aft at this, rather low, Reynolds number (corresponding roughly to a 10cm chord wing travelling at 25mph).

The pressure distributions for the same wing at a Reynolds number more representative of aerodynamic applications, 400,000, are shown in Figure 25, along with those already considered
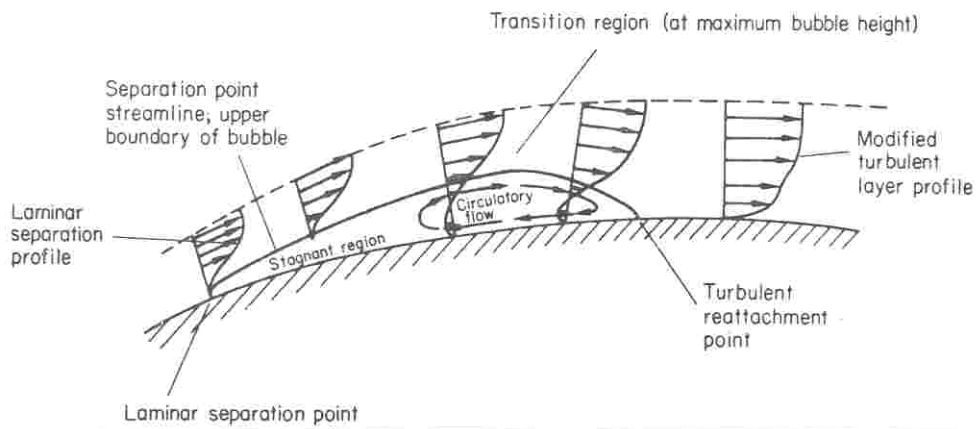
Figure 23: Flow separation and reattachment, with associated separation bubble.
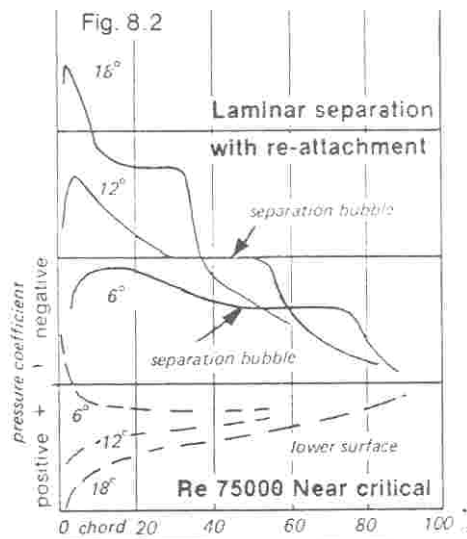

Figure 24: Pressure distributions on Göttingen 801 section at Reynolds number 75,000. The flat regions indicate lengthy upper surface separation bubbles.

($Re = 75,000$) and some for an even lower value ($Re = 42,000$). The $Re = 400,000$ results show no significant flat regions, but we can calculate (e.g. with Xfoil) that the boundary layer is still laminar when it reaches the suction peak. Transition is thus still occurring via separation and reattachment, but the bubble is very short, and always just after the suction peak, independent of angle of attack. In this case, the presence of the bubble will have a negligible effect on the lift, and the Reynolds number is 'super-critical'.
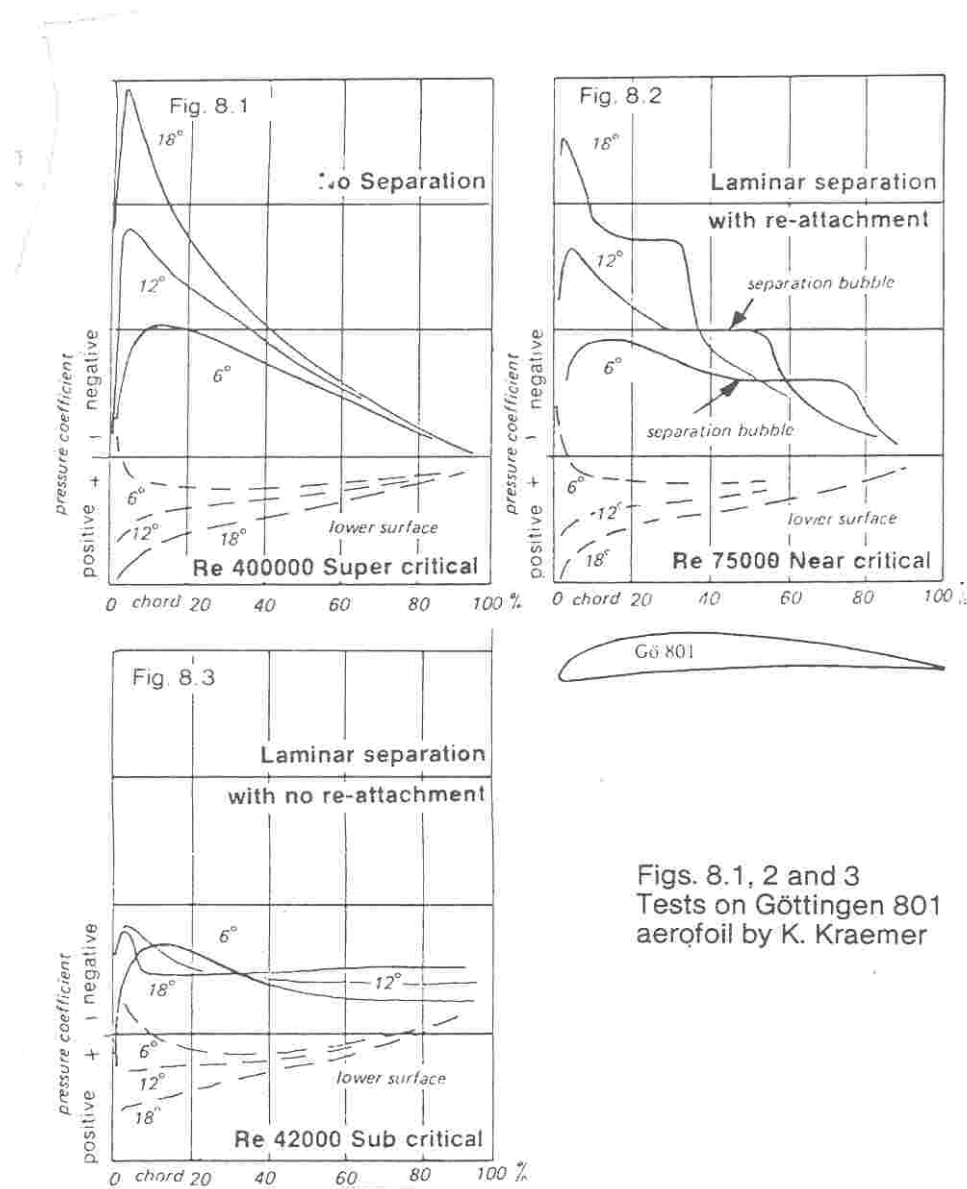

Figure 25: Pressure distributions on Göttingen 801 section at three different Reynolds numbers. The intermediate results are those of Figure 24. At the highest, there are no obvious separation bubbles (although transition will still occur via separation and reattachment). At the lowest, the flow never reattaches after laminar separation.

Finally, the lowest Reynolds number results show the behaviour we anticipated in the absence of turbulent reattachment. The upper surface pressures exhibit flat regions extending to the trailing edge without any recovery, indicating separated flow, with the separation point moving forward as incidence increases. This is fully laminar stall behaviour. Equivalently, the Reynolds

number is 'sub-critical'.

The previous discussion has demonstrated that separation bubble properties depend on both Reynolds number and incidence. It will come as no surprise that they are also influenced by the aerofoil geometry. The key factor here is the nose radius, which determines how 'sharp' the suction peak is (for a given incidence). A small nose radius guarantees a sufficiently adverse pressure gradient to separate the laminar boundary layer just after the peak, whereas a large one (combined with a low Reynolds number) may allow the boundary layer to remain laminar well downstream of the nose. This is not *necessarily* a good thing; further aft the thicker aerofoil will have a stronger adverse pressure gradient, and the laminar flow may then separate without reattachment.

2.6.3 Stall mechanisms

There is little more to say about sub-critical stall; in contrast, the range of separation bubble behaviour that has been observed in the critical regime could fill a book, but it cannot easily be summarised. At super-critical Reynolds numbers, however, stall can be categorised into two main types:

- **leading edge stall**, which is typically associated with thin aerofoils;

- **trailing edge stall**, which is typically associated with thick aerofoils.

The borderline between 'thin' and 'thick' is not well defined, but is around 12% thickness for aerodynamic Reynolds numbers.

Leading edge stall is linked to the presence of a separation bubble immediately after the suction peak, which is why it is associated with thin aerofoils. It is illustrated in Figure 26. As the angle of attack increases, so do the flow velocities around the leading edge and outside the separation bubble. Eventually, the force associated with entrainment by the separated shear layer becomes insufficient to provide the required normal acceleration, and the flow fails to reattach. The bubble has 'burst', and the aerofoil has stalled.

Trailing edge stall is simply due to a standard boundary layer separation. It is shown schematically in Figure 27. Since it is due to the cumulative effect of the suction surface adverse pressure gradient, it first appears near the trailing edge, and then progresses upstream as incidence increases. The boundary layer at separation is almost invariably turbulent (it is virtually impossible to come up with an aerofoil which maintains a laminar suction-surface boundary layer to the trailing edge), but may have become so either via 'natural' (i.e. attached) transition, or separation/reattachment.

It is intuitively clear from the foregoing descriptions that leading edge stall will be abrupt, and trailing edge stall gradual, as illustrated in Figure 28. Less obviously, aerofoils exhibiting leading edge stall typically have higher maximum lift coefficients than those that stall from the trailing edge. The reason is the link between stall type and aerofoil thickness. We saw in 2.4.2 that thickness is associated with adverse pressure gradients towards the rear of the aerofoil, and that these worsen with increasing thickness. Thus the price we pay for smoothing out the suction peak and avoiding a sudden leading edge stall is a more severe adverse pressure gradient downstream, and hence earlier boundary layer separation (as well as increased drag even while the flow remains attached).

To complete our discussion of stall, we should mention a particular type of leading edge stall, seen in the flow around a flat plate, and thus on some very thin aerofoils. It is shown schematically in Figure 29. Here the lack of surface curvature after the leading edge renders rapid reattachment impossible, and the separation bubble is typically long even at high Reynolds numbers. Furthermore, its length increases with incidence, until the reattachment point reaches the trailing edge. After this the aerofoil stalls relatively gently, but at a low lift compared
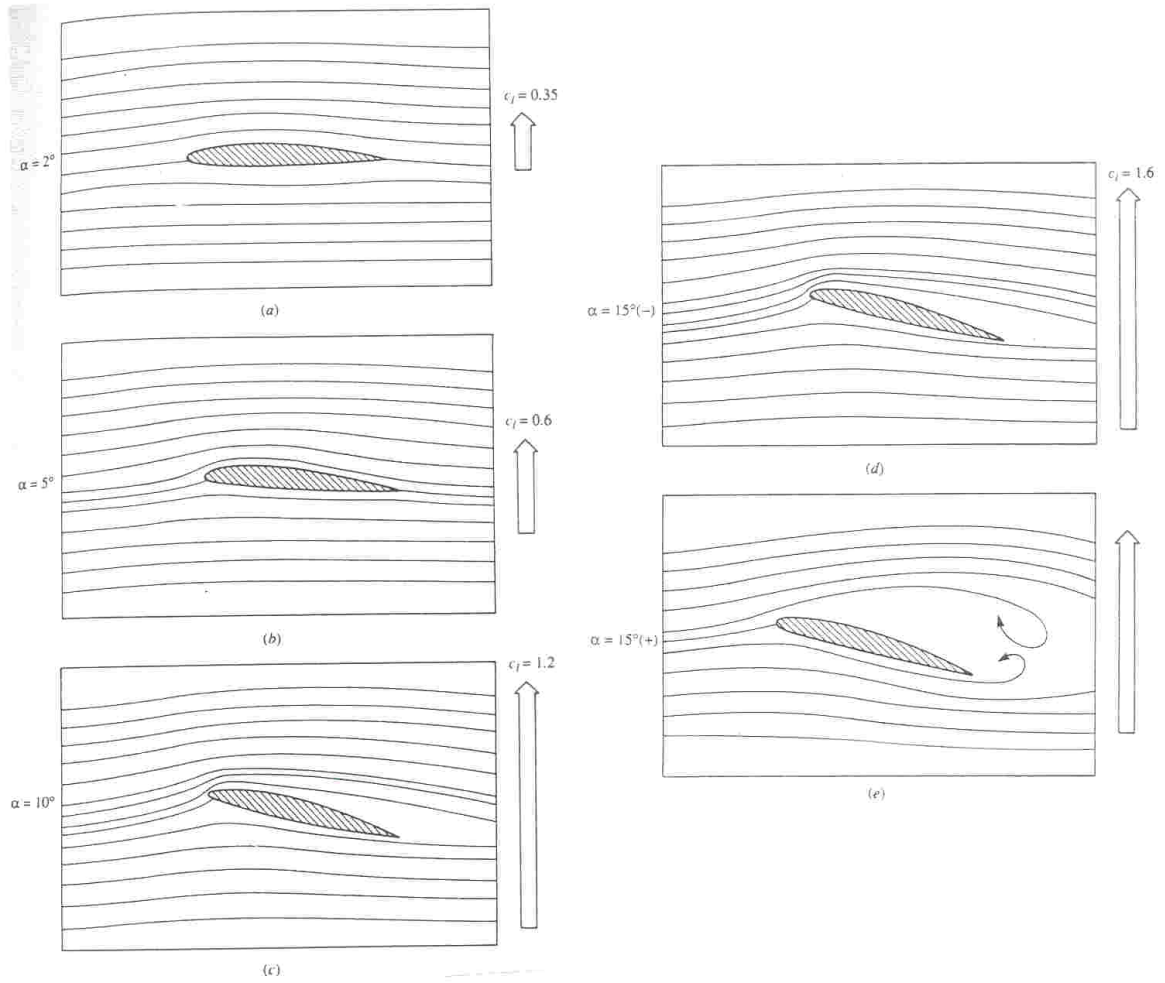
Figure 26: Streamlines around a NACA 4412 aerofoil at Re $= 210,000$, showing leading-edge stall behaviour. The arrows to the right of each diagram indicate the corresponding lift coefficients.
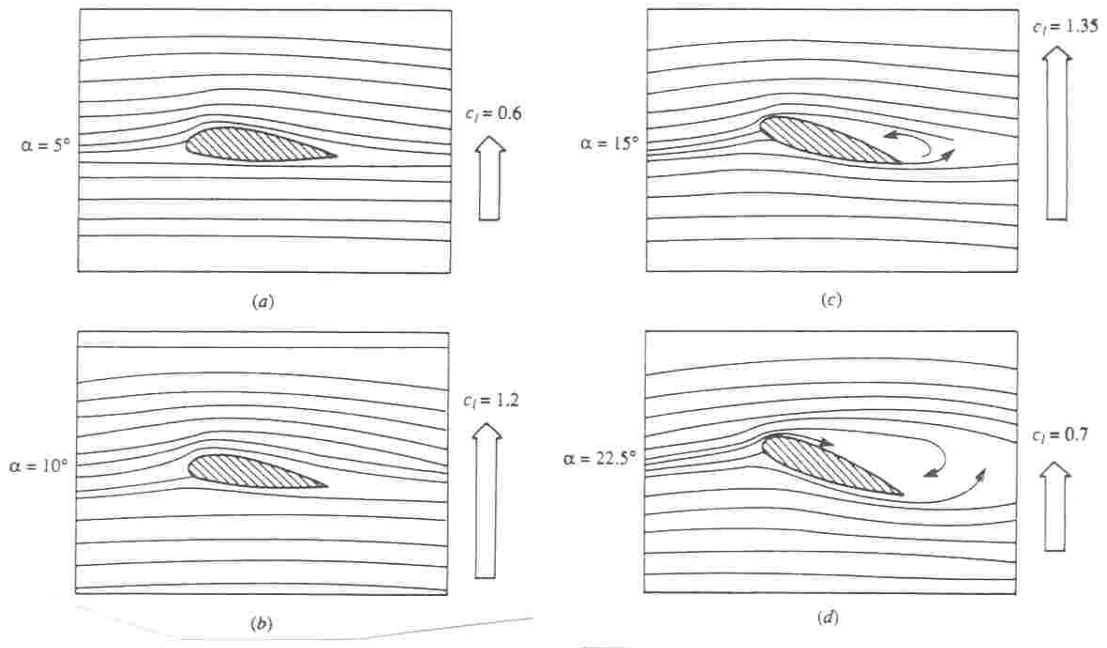
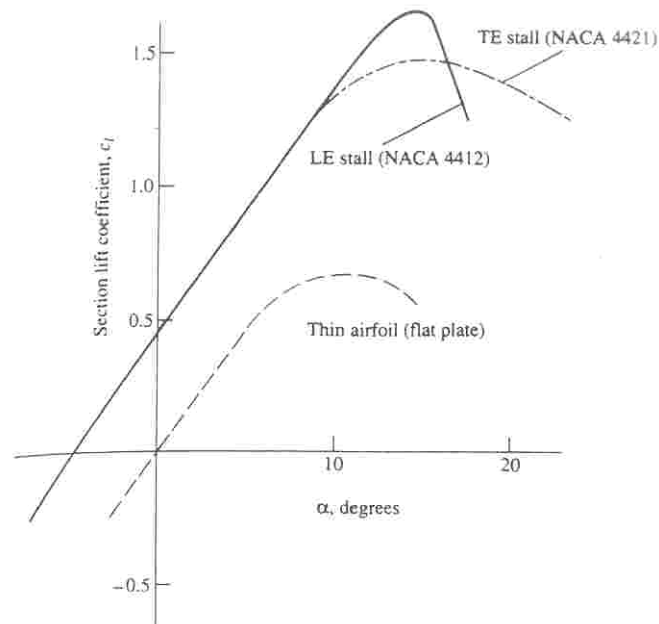Figure 27: Streamlines around a NACA 4421 aerofoil at Re $= 210,000$, showing trailing edge stall behaviour.

Figure 28: Lift-coefficient vs. incidence for the NACA 4412 (Figure 26) and 4421 (Figure 27) sections. Also shown are the results for a flat plate (Figure 29).
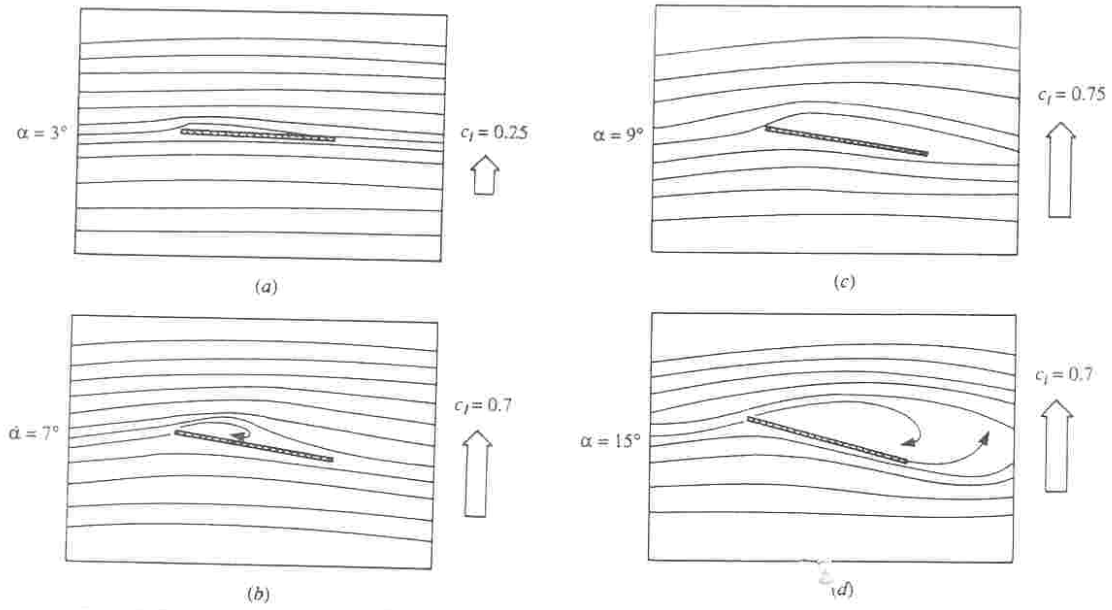
Figure 29: Streamlines around a flat plate at $Re = 210,000$, showing thin aerofoil stall behaviour.

to that obtainable from an aerofoil at supercritical Reynolds numbers, as shown in Figure 28. This figure also implies that maximum lift initially *increases* with thickness before decreasing; depending on section geometry, the optimum is typically around 12%.

2.6.4 Fixes for stall

Sections with unsatisfactory stall behaviour can often be improved by manipulating the boundary layer in some way. For example, the mixing in a turbulent boundary layer on the verge of separation can be enhanced (at the price of increased drag) by introducing streamwise vortices, via **vortex generators** (Figure 30). Alternatively, prolonged separation of a laminar boundary layer can be avoided by triggering transition ahead of the separation point, via **turbulators**, or **trip strips**. Given the different Reynolds numbers at which these problems are likely to occur, it is unsurprising that vortex generators tend to be found on full-scale aircraft, and trip-strips on model-scale wings. **Blowing** and **suction** are also effective ways of manipulating boundary layers, but are not yet regarded as sufficiently reliable for practical applications.
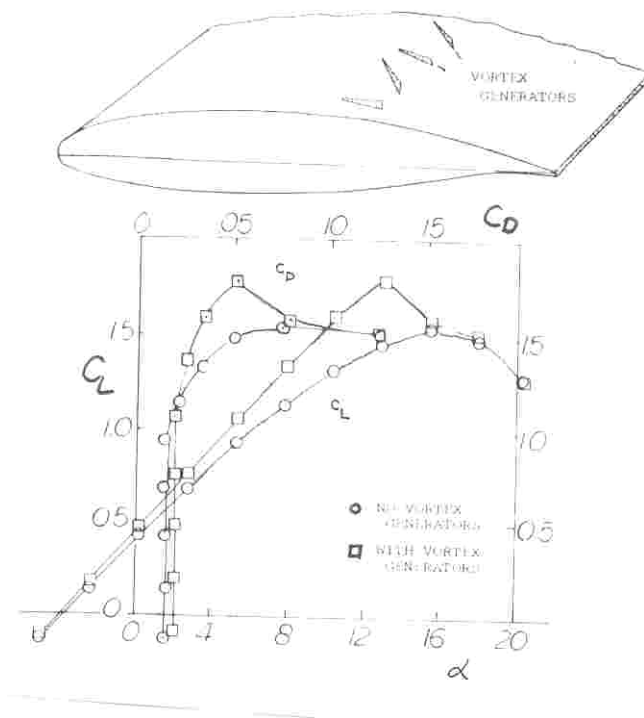
Figure 30: Vortex generators on the upper surface of a wing, and their effect on the aerodynamic forces. Note that drag is *increased* in the attached flow regime.

3 Three-Dimensional Flow Around Wings

Although two-dimensional aerofoil section theory tells us much of the story, it also misses some key points. The chief of these is that wings have to end somewhere, an inconvenient fact that is responsible for fundamental differences between the three-dimensional flow field and its two-dimensional counterpart. Also important are spanwise variations in wing geometry (e.g. chord length), and 'sweep' (streamwise displacement of the tips relative to the root). In this section, we discuss how to model and calculate the effects of these features. For simplicity, we ignore the presence of a fuselage, which does not alter the fundamental points that are made.

The material follows a similar order to the section on two-dimensional flow; first we consider the general features of the flow field, then numerical approaches to its calculation, followed by approximate methods (in this case, lifting-line theory and the horseshoe vortex representation) and stall behaviour. Finally, the important topic of sweep is investigated separately at the end.

3.1 General Features

3.1.1 Spanwise variations

When a finite-span wing provides lift, the pressure on the lower surface is, on average, higher than that on the upper surface. However, at the tips, the pressures must be equal. This implies that there is a reduction in the pressure difference between the wing surfaces as the tips are approached. **Thus, the flow over a finite wing is three-dimensional, even if there are no spanwise variations in its geometry.**
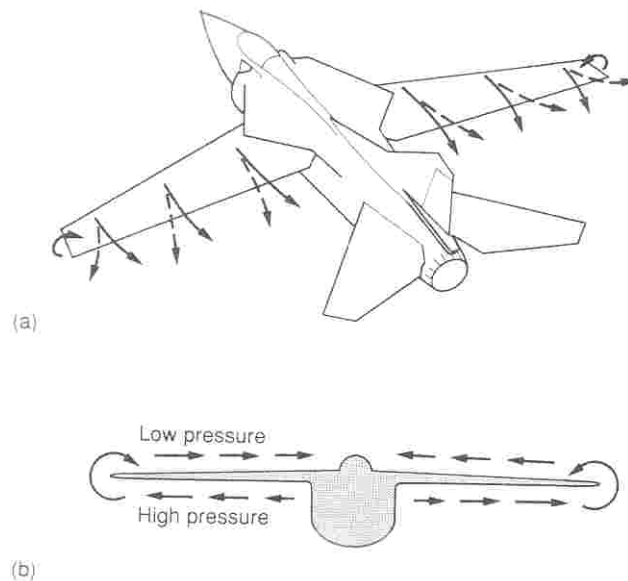
Figure 31: Spanwise pressure gradients (b) and resulting flow (a) over a wing of finite span.

The approximate nature of this flow can be deduced from the spanwise pressure gradients, which act towards the tip on the upper surface, and away from the tip on the lower (Figure 31(b)). Fluid particles are thus accelerated in these directions, as indicated in Figure 31(a). This observation suggests that the wing is likely to shed streamwise vorticity at its trailing edge

(consider the circulation around a contour including part of the wing in Figure 31(b)). If so, this is *fundamentally* different behaviour than found in 2D wing section flow. It also begs the question of how the Kutta condition can still be fulfilled. We shall address this issue shortly, but first we consider another indication that the 3D wing sheds streamwise vorticity: the fate of the bound vorticity.

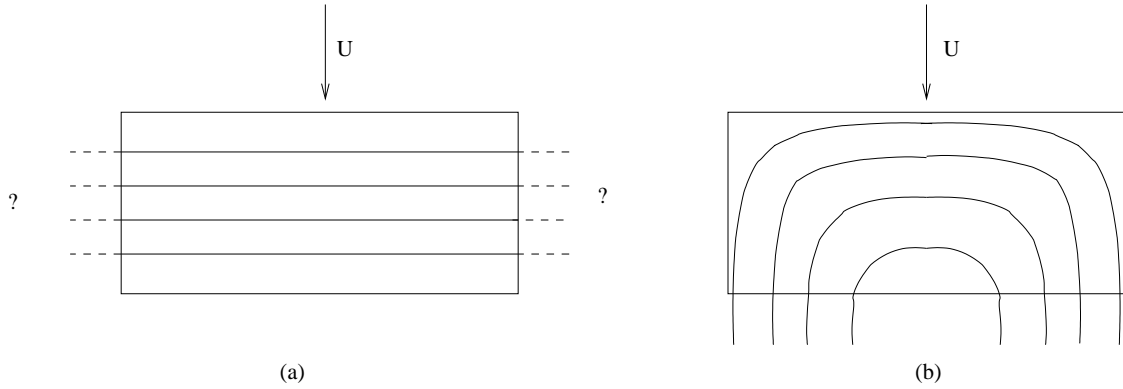### 3.1.2   What happens to the bound vorticity?

Figure 32: Bound vortex lines on a finite wing: (a) postulated two-dimensional pattern; (b) realistic topology, showing shed vorticity at trailing edge.

First, imagine that we *could* achieve two-dimensional flow on our rectangular wing. The bound vortex lines would then be straight and spanwise, as shown in Figure 32(a). They would, however, either have to stop at the tip, which would contravene Helmholtz's second law, or continue into the flow somehow. Now Helmholtz's first law (which states that vortex lines move with the flow) implies that free vorticity in a steady flow must have its vector aligned with the local flow velocity. Thus, having continued into the fluid, the vortex lines must eventually end up oriented with the free-stream as streamwise vorticity. These arguments, combined with the fact that the flow on the wing is *not* purely two-dimensional, lead to the postulated vorticity distribution shown in Figure 32(b), with initially spanwise bound vortex lines gradually curving into the streamwise direction, and leaving the trailing edge to form a *vortical wake*.

3.1.3   The Kutta condition in three dimensions

Just as in the 2D case, we have the choice of an infinite number of possible inviscid flows, and need to invoke viscous effects to specify the one that is physically relevant. Previously, this led us to the conclusion that the flow could not go around the trailing edge, which therefore had to be a stagnation point. This, however, appears to be inconsistent with the claim that vorticity is shed at the trailing edge of a wing.

The problem is resolved by the observation that, in 3D, the requirement on the flow to avoid going around the trailing edge does not necessarily imply a stagnation point, because the flow can have a spanwise component there. This is illustrated in Figure 33, which shows that it is possible to retain the 2D cross-sectional flow pattern (a) without a stagnation point, as long as the flow is purely spanwise at the trailing edge (b). Furthermore, the upper and lower surface components can be different, corresponding to a streamwise vortex sheet (c). There is, however, another physical requirement in addition to the Kutta condition; the pressure must be continuous across the sheet. This constraint implies (via Bernoulli) that $v_{sl} = v_{su}$.

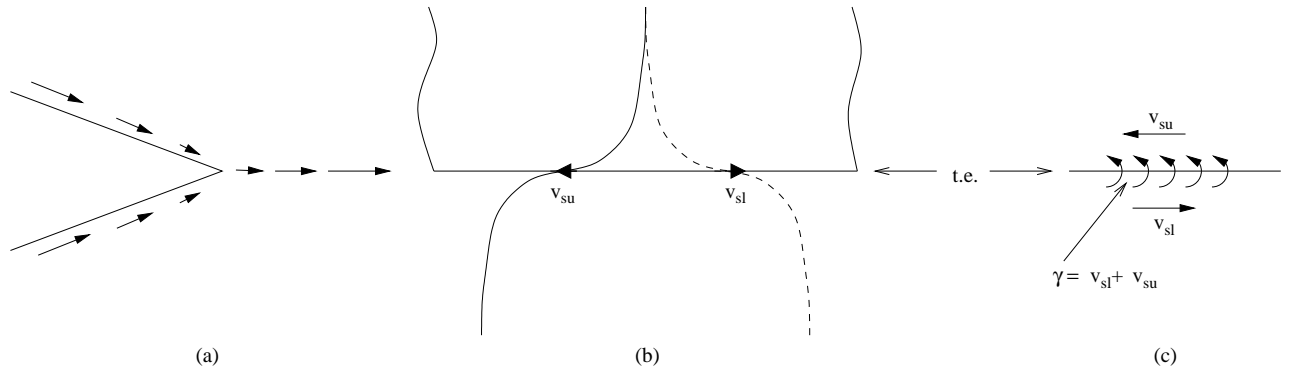Figure 33: The trailing edge flow specified by the Kutta condition for a finite span wing: (a) velocity vectors in the cross-sectional plane; (b) plan view of upper (—) and lower (- -) surface streamlines; (c) associated trailing vortex sheet.
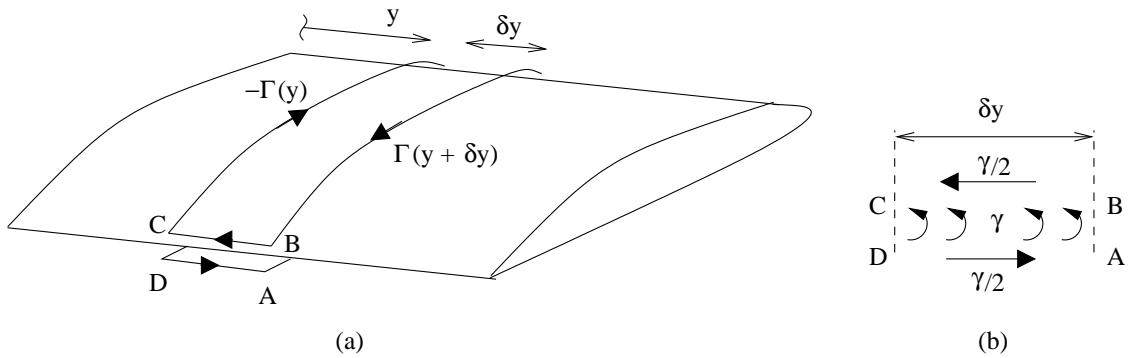

Figure 34: Analysis for the strength of the trailing vortex sheet behind a finite span wing: (a) wing, showing contour enclosing potential flow only; (b) trailing edge velocities.

We can link the vortex sheet strength, γ, to the circulation around the wing by considering two neighbouring cross sections, a distance δy apart (Figure 34(a)). The circulation around the first is:

$$\Gamma(y) = \Gamma_{DC} = -\Gamma_{CD}, \tag{95}$$

while that around the second is

$$\Gamma(y + \delta y) = \Gamma_{AB}. \tag{96}$$

Now the entire contour $A \to B \to C \to D \to A$ forms a closed curve enclosing potential flow, and thus has zero overall circulation. Therefore

$$\Gamma_{ABCDA} = \Gamma_{AB} + \Gamma_{BC} + \Gamma_{CD} + \Gamma_{DA} = 0. \tag{97}$$

Finally, from our previous arguments, the spanwise flow speeds at the trailing edge are $\gamma/2$ (Figure 34(b)), so

$$\Gamma_{BC} + \Gamma_{DA} = \gamma\delta y. \tag{98}$$

Equation (97) can thus be rearranged to give

$$\gamma\delta y = \Gamma(y) - \Gamma(y + \delta y) \simeq -\frac{d\Gamma}{dy}\delta y,$$

i.e.

$$\gamma = -\frac{d\Gamma}{dy}. \tag{99}$$

This relationship is central to understanding 3D wing flow. It states that a vortical wake is not just qualitatively likely, and admissible by the 3D Kutta condition, but is *inextricably linked* with the inevitable fall-off in wing loading (represented here by section circulation) towards the tips.

3.1.4   Where is the wake?

This may seem a stupid, or pointless, question. Do we need to know anything more than the observation that it extends downstream from the trailing edge? The answer is 'yes', unlike the 2D case, because of the trailing vorticity. The flow field associated with this vorticity turns out to have a material influence on the forces on the wing, as we shall see.

Recall that, in a steady flow, the vorticity and velocity vectors must be parallel. Thus, to a first approximation, we might expect the wake to consist of a flat vortex sheet more-or-less in the free-stream direction. In fact, though, the additional velocity components (associated with the bound and wake vorticity) result in the wake 'rolling up' into a pair of concentrated streamwise vortices (Figure 35). These are often referred to as 'tip vortices', in spite of consisting of shed vorticity from the entire trailing edge. They are sometimes visible as aircraft 'contrails' at altitude (the water vapour from the engine exhausts condenses into highly reflective ice crystals in the low pressure vortex cores), or as water vapour trails in humid conditions near the ground.
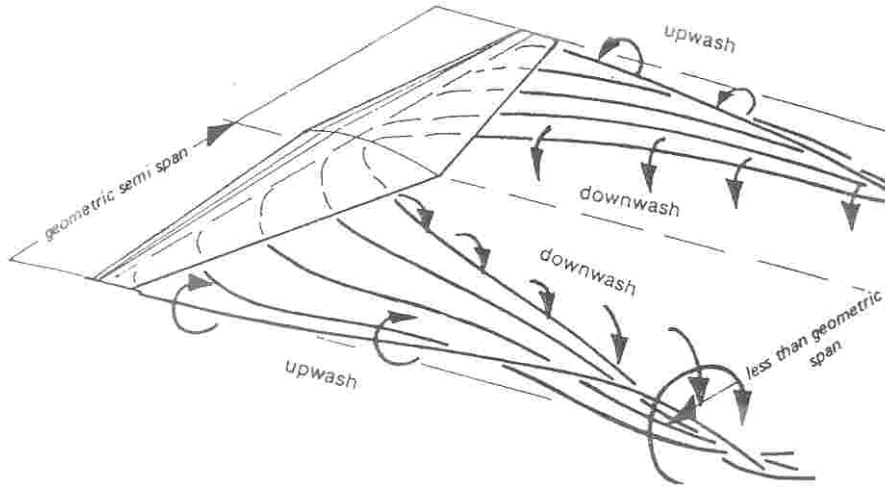
Figure 35: Schematic of trailing vortex formation via 'roll-up' of the vorticity shed by a 3D wing.

3.1.5 The forces on the wing

Although the lift of a 3D wing is inevitably modified from that of its 2D counterpart by the reduction in load towards the tips, the mechanism by which it is generated remains qualitatively the same. The major change in going from 2D to 3D is manifested in the drag, which is now non-zero **even before taking viscous effects into account**. This phenomenon is known as **induced drag**.

One can see that the 3D wing must experience drag from energy arguments. The continuous creation of more vortical wake, with its associated kinetic energy, can only come about if the wing is doing work on the fluid. Lift, by definition, is perpendicular to the direction of travel, so the work input must be linked to a drag force. (If this sounds self-evident to you, you might like to consider why a similar argument *doesn't* apply in the 2D case.) Alternatively, the drag can be viewed as a by-product of the **downwash** associated with the vortical wake. If we accept, for the moment, that the downwash exists, then Figure 36 shows how it leads to an induced drag component. For a downwash w_d, the effective oncoming flow is rotated downwards by an angle

$$\alpha_d = \tan^{-1}\left(\frac{w_d}{U}\right), \tag{100}$$

and this results in a similar rotation of the lift vector, so the resultant force now has a streamwise component – the induced drag. Note too that the downwash also leads to a reduction in incidence, and hence in the magnitude of the lift vector.

3.1.6 Summary

The general features of the flow around a wing of finite span may be summarised as follows:

- the presence of **spanwise pressure gradients**, due to pressure continuity at the wing tips, causes corresponding **spanwise cross-flows**;
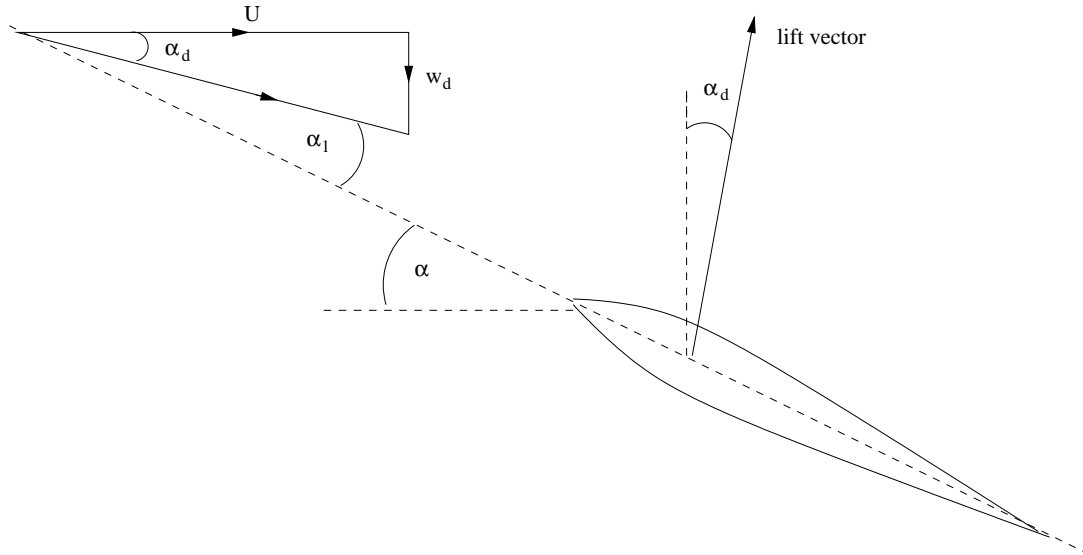
Figure 36: The effect of downwash is to reduce the local angle of attack from α to α_1, and to rotate the lift vector so that it has a streamwise component.

- the cross-flows result in the shedding of **a sheet of (essentially) streamwise vorticity** at the trailing edge, with strength determined by the spanwise variation of wing circulation;

- associated with the trailing vortex sheet is a streamwise force on the wing, known as **induced drag**. This is an entirely *inviscid* phenomenon.

3.2   Panel Methods in Three-Dimensions

3.2.1   Introduction

Like their two-dimensional counterparts, 3D panel methods aim to find an exact numerical solution for the potential flow field around a body without further modelling approximations. The body surface is divided into a set of panels, each having a distribution of elementary solutions with unknown strength. The boundary condition of zero normal flow on the surface is then applied to find these strengths. Once they are obtained, the velocity at any point in the flow field can be calculated without further discretisation. This makes panel methods much more efficient than numerical solutions of the Euler and Navier-Stokes equations (which require a mesh in the fluid), and they are therefore still important design tools.

Although straightforward in principle, panel methods can be complicated in practice. A consultation of the literature will reveal a bewildering array of possible formulations, due to two features of the theory:

(i) the type of elemental solution that one chooses for the panels is not unique, i.e. the same flow external to the body can be produced in different ways;

(ii) a range of other boundary conditions can be shown to be equivalent to that of zero normal flow.

Furthermore, to make things worse, the most obvious and/or intuitive approaches may not necessarily be the best numerically.

A study of these issues is beyond the scope of the course. Here, then, we shall restrict ourselves to a brief discussion of panel element types.

3.2.2 Types of elemental solution

You have already met two fundamental solutions that can be used as the basis for panels: the 3D source and doublet. A 'source panel' simply consists of a prescribed distribution (eg uniform) of sources over the panel area; a 'doublet panel' is similarly formed from a doublet distribution. With these building blocks, one has all that is needed to construct a panel method.

   Alternatively, given our discussion of 2D aerofoil flows, one might expect to be able to represent a closed body by a surface vortex sheet, which would then model the boundary layer. This is true, with one important caveat: the Helmholtz condition that vortex lines cannot end in the fluid must be enforced, either by a choice of panel that does so implicitly, or by auxiliary conditions. Also, to create a panel method on this basis, one must be able to calculate the velocity field associated with a vortex sheet element. This requires a theoretical result that you have not yet encountered: the Biot-Savart law.
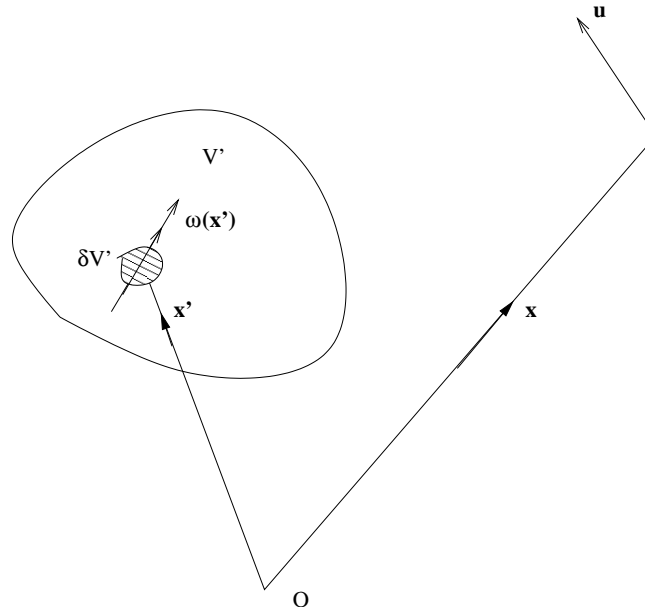
3.2.3 The Biot-Savart law

Figure 37: Geometry for the Biot-Savart law applied to a volume V' of vorticity, equation (101)

In its most general form, the Biot-Savart law tells us the velocity field due to a 3D distribution of vorticity. The derivation is involved, so is relegated to Appendix B. The result is

$$\boldsymbol{u}(\boldsymbol{x}) = \frac{1}{4\pi} \int_{V'} \frac{\boldsymbol{\omega}(\boldsymbol{x}') \times (\boldsymbol{x} - \boldsymbol{x}')}{\mid \boldsymbol{x} - \boldsymbol{x}' \mid^3} dV' \tag{101}$$

where (see Figure 37) $\boldsymbol{x}$ is the observer location and the integration is over the entire region containing vorticity. For a vortex sheet (Figure 38(a)), the law becomes

$$\boldsymbol{u}(\boldsymbol{x}) = \frac{1}{4\pi} \int_{S'} \frac{\boldsymbol{\gamma}(\boldsymbol{x}') \times (\boldsymbol{x} - \boldsymbol{x}')}{\mid \boldsymbol{x} - \boldsymbol{x}' \mid^3} dS', \tag{102}$$

where the sheet strength is the integrated vorticity across it:

$$\boldsymbol{\gamma}(\boldsymbol{x}') = \int \boldsymbol{\omega}(\boldsymbol{x}' + \eta\boldsymbol{n}) d\eta. \tag{103}$$
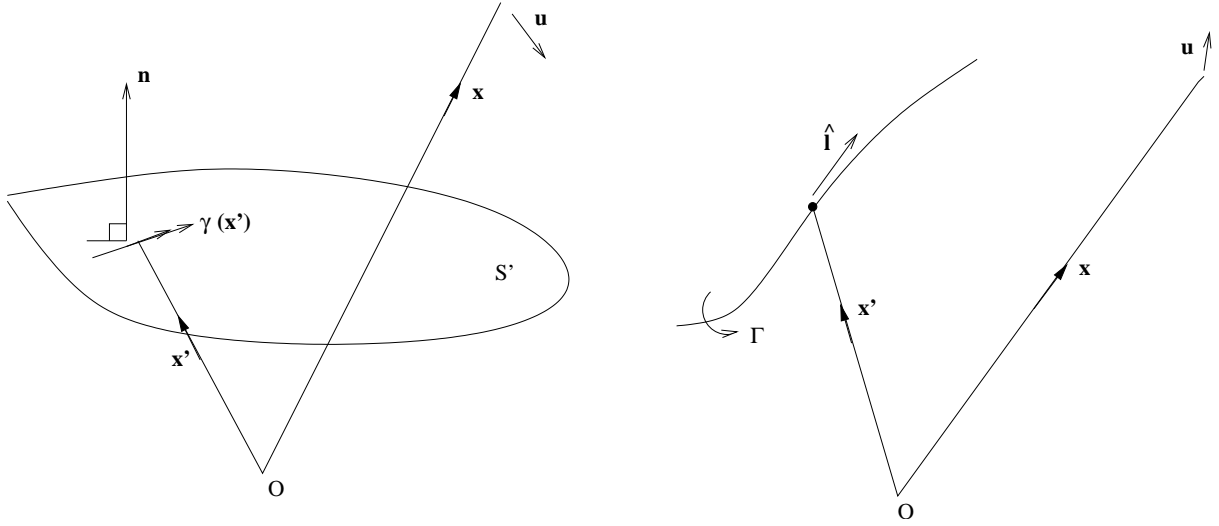
Figure 38: Simplified representations of 3D vorticity fields: (a) vortex sheet, covering region S' with normal $\mathbf{n}$; (b) line vortex, with lengthwise coordinate l.

Similarly, for a line vortex (Figure 38(b)), the vorticity is concentrated around the axis, with direction $\hat{\boldsymbol{l}}$, and can be integrated over the plane normal to the line to give

$$\boldsymbol{u}(\boldsymbol{x}) = \frac{\Gamma}{4\pi} \int \frac{\hat{\boldsymbol{l}} \times (\boldsymbol{x} - \boldsymbol{x}')}{\mid \boldsymbol{x} - \boldsymbol{x}' \mid^3} dl, \tag{104}$$

where Γ is the circulation of the vortex.

Example: Velocities due to a straight vortex line

Example (cont'd)

3.3 Lifting Surface Methods

Simplifications analogous to thin aerofoil theory can also be applied in three dimensions. The result is a vortex sheet lying on the camber surface of the wing, with strength to be determined from the boundary condition that the flow is parallel to this surface.
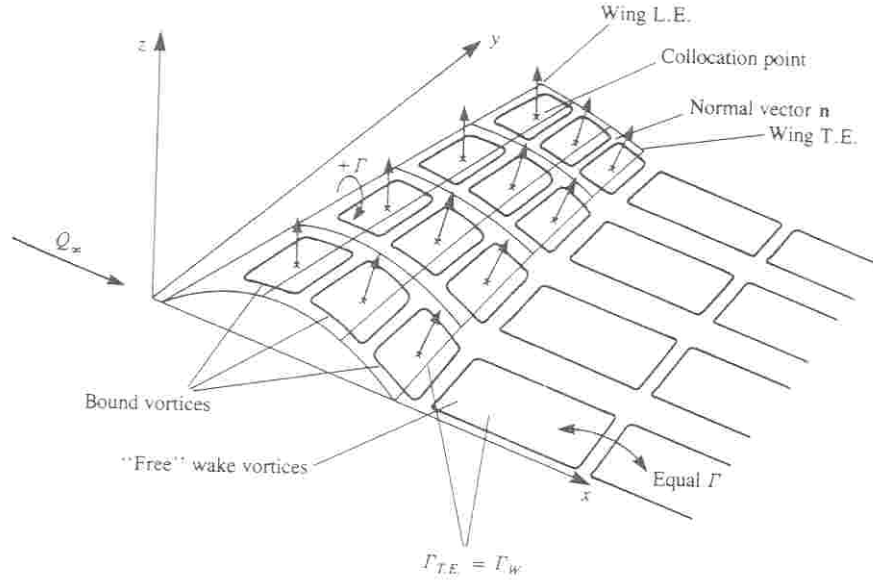

Figure 39: The vortex lattice discretisation for lifting surface calculations.

A popular numerical implementation of the lifting surface concept is the **vortex lattice method**, illustrated schematically in Figure 39. Here the vortex sheet is discretised as a set of quadrilateral vortex 'rings', thus automatically satisfying the Helmholtz requirement of continuity of vorticity. The Kutta condition is fulfilled by placing horseshoe vortices at the trailing edge. A well-established example of such a code is Mark Drela's AVL, available at http://web.mit.edu/drela/Public/web/avl.

3.4 The Lifting-Line Theory

As its name suggests, this theory simplifies the 3D problem by representing the wing as a 'lifting line' in the flow. This is an approximation that we would expect to become increasingly applicable as the ratio of the wing's span to its chord (the **aspect ratio**) gets bigger. In this case, we anticipate that the flow at a given spanwise station becomes closer and closer to its two-dimensional equivalent (imagine stretching the wing of Figure 32(b); what happens to the lines of bound vorticity?), and this observation is central to the development of the theory. First, however, we need to clarify what is meant by a 'lifting line'.

3.4.1 Lifting-line representation of a high-aspect-ratio wing

If the flow around a given section of the wing is effectively two-dimensional, then we can employ the 2D lift result:

$$l(y) = \rho U \Gamma(y). \tag{105}$$

Here $l(y)$ is the lift per unit spanwise distance, and varies with spanwise location, y. This equation tells us that, provided we know the dependence $\Gamma(y)$ of circulation on span, we can calculate the overall lift by integrating from one wingtip ($y = -s$) to the other ($y = s$):

$$L = \rho U \int_{-s}^{s} \Gamma(y) dy. \tag{106}$$

Thus, **the lifting line consists of a line vortex of variable circulation at the wing location**. Physically, it represents the bound vorticity of the wing.
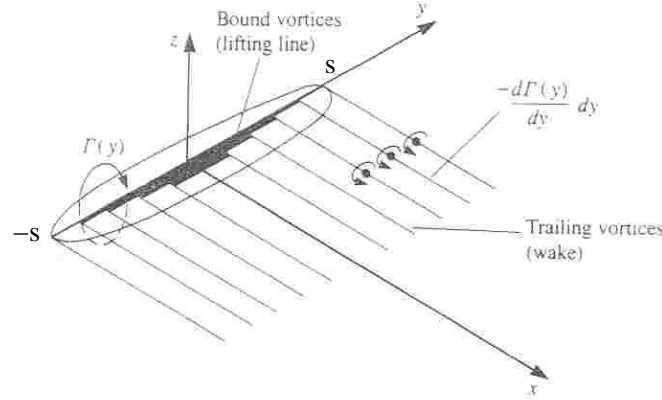

Figure 40: The lifting-line model of a finite wing.

We have already seen that a spanwise variation of circulation must be accompanied by a trailing vortex sheet, with strength $-d\Gamma/dy$. The addition of this sheet completes the lifting-line model, which is shown in Figure 40. Note that the vortex sheet is shown as remaining plane and aligned with the free-stream, not rolling up as in practice. This approximation is necessary to make the model tractable, and is justified on the basis that the vorticity nearest the wing has the greatest influence on it. It becomes less tenable as the flow velocities depart further from the free-stream value, i.e. as the loading on the wing increases. The lifting-line model is thus most applicable to lightly-loaded wings at small angles of attack. We therefore develop the theory assuming that this restriction applies.
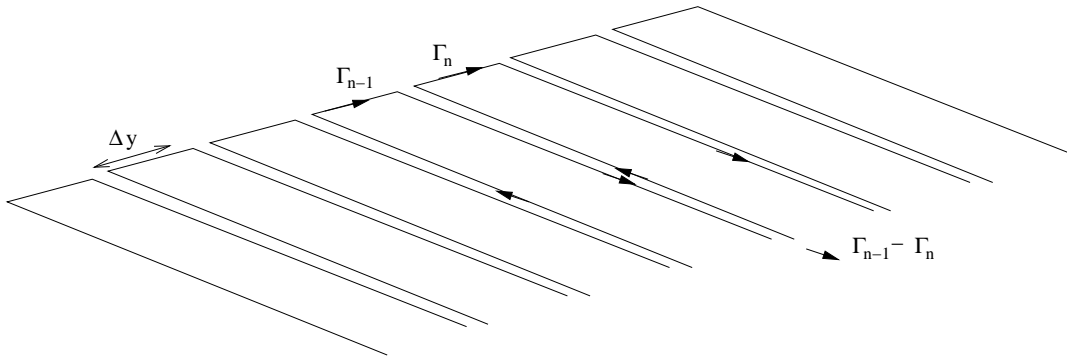

Figure 41: The lifting-line model as a collection of horseshoe vortices.

An alternative view of the lifting line model is to look at it as a collection of discrete horseshoe vortices, as shown in Figure 41. Each horseshoe vortex has constant circulation, but these circulations vary with span. The wake circulation in an element of width Δy is thus

$$\Gamma_{n-1} - \Gamma_n \simeq -\frac{d\Gamma}{dy}\Delta y, \tag{107}$$

as we would expect from Figure 40. As well as providing a helpful, intuitive way of looking at the lifting-line model, this view is also important in solving it numerically, as we shall see.

3.4.2 The downwash and induced drag

We have seen that the fundamental parameter of the lifting-line theory is the bound circulation, $\Gamma(y)$. We can calculate this from the local aerofoil section properties, but only if we know the local incidence, which we have seen (Figure 36) is affected by the wake downwash. We thus need to calculate this quantity.
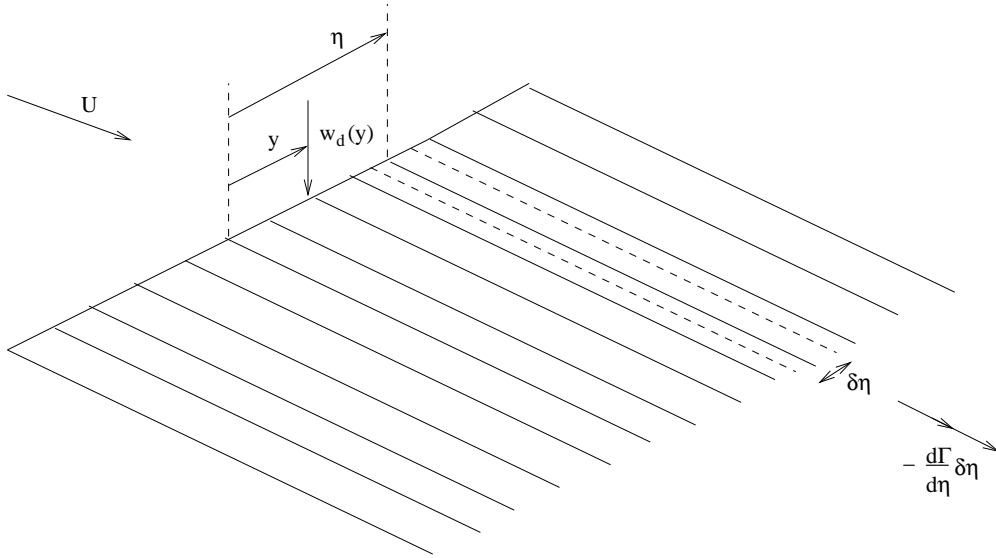
Figure 42: Notation for the downwash calculation, equation (108) ff.

First, consider the contribution from a single element of the wake, located at spanwise position η and of width $\delta\eta$ (Figure 42). The circulation of this element is $(-d\Gamma(\eta)/d\eta)\delta\eta$, and it is semi-infinite viewed from the spanwise position y. Thus, from the Biot-Savart rule for a straight vortex, the downwash at this position is:

$$\delta w_d(y) = \left(-\frac{d\Gamma(\eta)}{d\eta}\delta\eta\right)\frac{1}{4\pi(\eta - y)}. \tag{108}$$

The overall downwash at this location is given by the sum of the wake element contributions, i.e.

$$w_d(y) = \frac{1}{4\pi}\int_{-s}^{s}\frac{d\Gamma(\eta)}{d\eta}\frac{d\eta}{y - \eta}. \tag{109}$$

The corresponding downwash angle (Figure 36) is $\tan^{-1}(w_d/U)$, but our light-loading assumption allows us to replace this by w_d/U, so

$$\alpha_d(y) \simeq \frac{1}{4\pi U} \int_{-s}^{s} \frac{d\Gamma(\eta)}{d\eta} \frac{d\eta}{y - \eta}. \tag{110}$$

Finally, the local induced drag is given by $l(y)\sin\alpha_d(y) \simeq l(y)\alpha_d(y) = \rho U\Gamma(y)\alpha_d(y)$, so the overall induced drag is

$$D_i = \rho U \int_{-s}^{s} \Gamma(y)\alpha_d(y)dy. \tag{111}$$

Thus, a knowledge of the spanwise circulation variation gives us not only the lift on the wing, but also (via (111) and (109)) the induced drag. This brings us back to the central problem of the lifting-line model: how to solve for the circulation distribution.

3.4.3 The lifting-line equation

The key to finding the circulation is its link to the local lift, which is, in turn, linked to the local lift coefficient, c_l. Now, we know from 2D thin aerofoil theory that $c_l = 2\pi(\alpha - \alpha_0)$ and, since the flow around a given section is assumed locally 2D, this relation must carry over, with α replaced by its local value, α_l, where (see Figure 36)

$$\alpha_l = \alpha - \alpha_d. \tag{112}$$

We thus have

$$l(y) = \frac{1}{2}\rho U^2 c(y).2\pi(\alpha - \alpha_d(y) - \alpha_0(y)), \tag{113}$$

where $c(y)$ is the local chord length. Equating this expression with the local lift expressed in terms of circulation, (105), gives us the lifting-line equation:

$$\frac{\Gamma(y)}{\pi U c(y)} = \alpha - \alpha_0(y) - \alpha_d(y), \tag{114}$$

or, with the dependence on Γ shown explicitly via (110),

$$\frac{\Gamma(y)}{\pi U c(y)} = \alpha - \alpha_0(y) - \frac{1}{4\pi U} \int_{-s}^{s} \frac{d\Gamma(\eta)}{d\eta} \frac{d\eta}{y - \eta}. \tag{115}$$

Before discussing how to solve this equation, we should note two points about the zero lift angle, α_0. First, it has been written as a function of y because of the possibility that the section camber-line may vary with span. Second, it can also account for an important design parameter that we have not yet mentioned: **twist**. Twist, i.e. the local rotation of a section, gives the designer an effective means of controlling wing loading. A local, pitch-up, rotation of a section by α_t increases the lift coefficient by $2\pi\alpha_t$, and this effect is thus straightforwardly included by writing

$$\alpha_0(y) = \alpha_{0c}(y) - \alpha_t(y), \tag{116}$$

where $\alpha_{0c}(y)$ represents the contribution due to camber.

Solving the lifting-line equation for a general wing geometry requires a numerical approach. There is, however, one particular analytical solution that is of special interest — the elliptical lift distribution — and we shall consider this first.
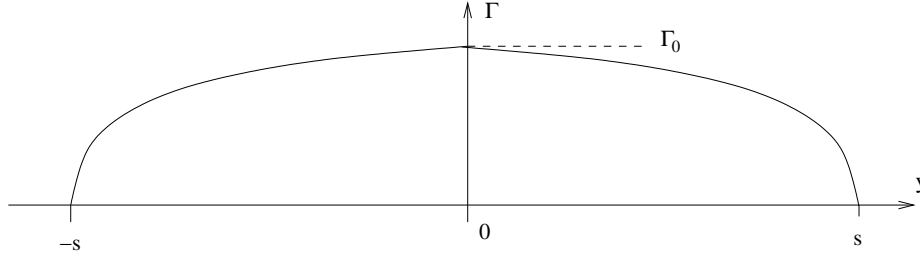
Figure 43: An elliptical circulation distribution.

3.4.4 The elliptical lift distribution

The half-ellipse circulation distribution shown in Figure 43 is described by

$$\Gamma(y) = \Gamma_0 \left(1 - \frac{y^2}{s^2}\right)^{1/2} \tag{117}$$

Assuming that this distribution can be realised somehow, what is the associated downwash? If we make the substitution $\eta = -s \cos \phi$ in (109), then we have:

$$d\eta = \frac{d\eta}{d\phi} d\phi, \tag{118}$$

$$\Gamma(\eta) = \Gamma_0 \sin \phi, \tag{119}$$

and

$$\frac{d\Gamma}{d\eta} = \frac{d\Gamma}{d\phi} \frac{d\phi}{d\eta} = \frac{\Gamma_0 \cos \phi}{d\eta/d\phi}. \tag{120}$$

Substituting into (109),

$$w_d(y = -s \cos \theta) = \frac{\Gamma_0}{4\pi s} \int_0^\pi \frac{\cos \phi}{\cos \phi - \cos \theta} d\phi. \tag{121}$$

The integral is one we have come across before in thin aerofoil theory, and in Appendix A we showed that it takes the value π. **Therefore, the downwash associated with the elliptic lift distribution is constant, and has the value** $\Gamma_0/4s$.

We can now ask what shape wing will exhibit this lift distribution, by returning to the lifting line equation, (114). This becomes

$$\frac{\Gamma(y)}{\pi U c(y)} = \alpha - \alpha_0(y) - \frac{\Gamma_0}{4Us}. \tag{122}$$

If our wing is untwisted and of uniform section shape, $\alpha_0(y)$ is a constant, as then is the entire right-hand side. **In this case, the chord variation required to produce an elliptic lift distribution is itself elliptic,** i.e. $c(y) = c_0(1 - y^2/s^2)^{1/2}$.

The forces on the wing are straightforward to evaluate as follows:

$$L = \rho U \int_{-s}^s \Gamma(y) dy = \rho U \int_0^\pi (\Gamma_0 \sin \theta) s \sin \theta d\theta = \frac{\pi \rho U \Gamma_0 s}{2}, \tag{123}$$

$$D_i = \rho U \int_{-s}^s \Gamma(y) \alpha_d(y) dy = \rho U \int_{-s}^s (\Gamma_0 \sin \theta) \frac{1}{U} \left(\frac{\Gamma_0}{4s}\right) s \sin \theta d\theta = \pi \rho \frac{\Gamma_0^2}{8}. \tag{124}$$

The most informative way to view these results is in terms of the lift and drag coefficients:

58

$$C_L = \frac{L}{\frac{1}{2}\rho U^2 S} = \frac{\pi \Gamma_0 s}{US}, \tag{125}$$

$$C_{Di} = \frac{D_i}{\frac{1}{2}\rho U^2 S} = \frac{\pi}{4S}\left(\frac{\Gamma_0}{U}\right)^2, \tag{126}$$

where S is the wing area. We can eliminate Γ_0 between these two expressions to give

$$C_{Di} = \frac{\pi}{4S}\left(\frac{C_L S}{\pi s}\right)^2 = \frac{C_L^2}{\pi A_R}, \tag{127}$$

where A_R, the **aspect ratio** of the wing, is defined by

$$A_R = \frac{4s^2}{S}. \tag{128}$$

(It's not immediately obvious why this is a sensible definition. However, if we note that the mean wing chord, $\bar{c}$, is $S/2s$, then we see that $A_R = 2s/\bar{c}$.)

Although this result is specific to the elliptic lift distribution, it exhibits two features that are true of induced drag in general:

- **it increases as the square of the lift**;

- **it decreases with increasing wing aspect ratio.**

The latter observation explains why flight vehicles for which low drag is crucial (e.g. gliders, albatrosses) tend to have high aspect ratio wings. Unfortunately, though, the inconvenient realities of structural engineering limit the wing designer's ability to increase aspect ratio *ad infinitum*.

The reduction in lift towards the wing tips also corresponds to a drop in the lift-curve slope compared to the 2D value. From (122) and (125), it is possible to show that

$$C_L = \frac{2\pi}{1 + 2/A_R}(\alpha - \alpha_0). \tag{129}$$

(The working is an examples paper exercise.) The lift-curve slope is thus reduced by a factor $(1 + 2/A_R)^{-1}$. Once again, we can see the aerodynamic desirability of a high aspect ratio.

3.4.5 Solution of the lifting-line equation in general

(a) The Fourier series approach

This method dates from the pre-computer era, but remains of interest because of the insight that it gives into induced drag. As for the elliptic distribution, we make the substitution $y = -s\cos\theta$, but do not constrain the lift distribution. Instead, we express it as the Fourier series

$$\Gamma(y = -s\cos\theta) = Us \sum_{n \text{ odd}} G_n \sin n\theta. \tag{130}$$

Our task now is to find the unknown coefficients, G_n, for a given wing geometry. (Note that this form ensures that $\Gamma(y = \pm s) = 0$. Why don't we need terms with n even?)

As before, we start by evaluating the downwash velocity, using the substitution $\eta = -s\cos\phi$ in (109). Equation (118) still holds, but

$$\Gamma(\eta) = Us \sum_{n \text{ odd}} G_n \sin n\phi \tag{131}$$

and

$$\frac{d\Gamma}{d\eta} = \frac{d\Gamma}{d\phi}\frac{d\phi}{d\eta} = Us\frac{\sum_{n\text{odd}} nG_n \cos n\phi}{d\eta/d\phi}. \tag{132}$$

Equation (110) becomes

$$\alpha_d(y) = \frac{1}{4\pi} \sum_{n \text{ odd}} nG_n \int_0^\pi \frac{\cos n\phi}{\cos\phi - \cos\theta} d\phi = \frac{1}{4} \sum_{n \text{ odd}} nG_n \frac{\sin n\theta}{\sin\theta}, \tag{133}$$

again using the results in Appendix A. The lifting-line equation, (114), can be rearranged as

$$\frac{\Gamma(y)}{\pi Uc(y)} + \alpha_d(y) = \alpha - \alpha_0(y), \tag{134}$$

and substituting for $\Gamma(y)$ and $\alpha_d(y)$ using (131) and (133) leads to

$$\sum_{n \text{ odd}} \left[\frac{s}{\pi c(\theta)} + \frac{n}{4\sin\theta} \right] G_n \sin n\theta = \alpha - \alpha_0(\theta). \tag{135}$$

This equation can be solved by truncating the summation (at $n = 2N-1$ say), and then insisting that it is satisfied at N values of θ. This gives us N linear equations in the N unknowns G_n, and these can be solved computationally (or by hand, in the case of early aerodynamicists). Given, however, that we do not know which values of θ we should choose, and that computer requirements are no longer a serious issue in this problem, it makes more sense to choose a number greater than N, and solve the resulting over-determined set of equations in a least-squares sense. Matlab will do this without batting an eyelid.

The continued interest in this solution method lies in what it tells us about the lift and induced drag forces. First, the lift coefficient is given by

$$
\begin{aligned}
C_L &= \frac{\rho U}{\frac{1}{2}\rho U^2 S} \int_{-s}^s \Gamma(y) dy = \frac{2}{US} \int_0^\pi \left(Us \sum_{n \text{ odd}} G_n \sin n\theta \right) s \sin\theta d\theta \\
&= \frac{2s^2}{S} \int_0^\pi G_1 \sin^2\theta d\theta \\
&= \frac{\pi A_R}{4} G_1.
\end{aligned}
\tag{136}
$$

Remarkably, then, only the first term in the Fourier series contributes to the lift. The induced drag coefficient is

$$
\begin{aligned}
C_{Di} &= \frac{\rho U}{\frac{1}{2}\rho U^2 S} \int_{-s}^s \Gamma(y)\alpha_d(y) dy \\
&= \frac{2}{US} \int_0^\pi \left(Us \sum_{n \text{ odd}} G_n \sin n\theta \right) \left(\frac{1}{4} \sum_{m \text{ odd}} mG_m \frac{\sin m\theta}{\sin\theta} \right) s \sin\theta d\theta \\
&= \frac{s^2}{2S} \sum_{n \text{ odd}} \sum_{m \text{ odd}} mG_n G_m \int_0^\pi \sin n\theta \sin m\theta d\theta \\
&= \frac{\pi A_R}{16} \sum_{n \text{ odd}} nG_n^2,
\end{aligned}
\tag{137}
$$

since the only non-zero integrals are those for which $m = n$. We can cast this expression in a form similar to the elliptic case by substituting $G_1 = 4C_L/\pi A_R$, so

$$C_{Di} = \frac{\pi A_R}{16} \left(\frac{4C_L}{\pi A_R} \right)^2 \sum_{n \text{ odd}} n \frac{G_n^2}{G_1^2} = (1 + \delta) \frac{C_L^2}{\pi A_R}, \tag{138}$$

where

$$\delta = 3 \frac{G_3^2}{G_1^2} + 5 \frac{G_5^2}{G_1^2} + \cdots . \tag{139}$$

This confirms our earlier comments on the general dependence of induced drag on lift and aspect ratio. More importantly, since δ is always positive, it shows that **the elliptic lift distribution is associated with the minimum induced drag**. The validity of (138) was confirmed experimentally by Prandtl in 1915. The left-hand plot of Figure 44 shows measured drag polars on wings of the same cross-section, but different aspect ratio. Assuming that the lift-dependent component of drag is described by (138), it should be possible to collapse the results onto a single, universal curve. Prandtl did this by using (138) to predict the polar for $A_R = 5$ from the polars for other aspect ratios. The results, shown in the right-hand plot, are beautifully convincing; in fact, remarkably so, given that the aspect ratios are not especially large.
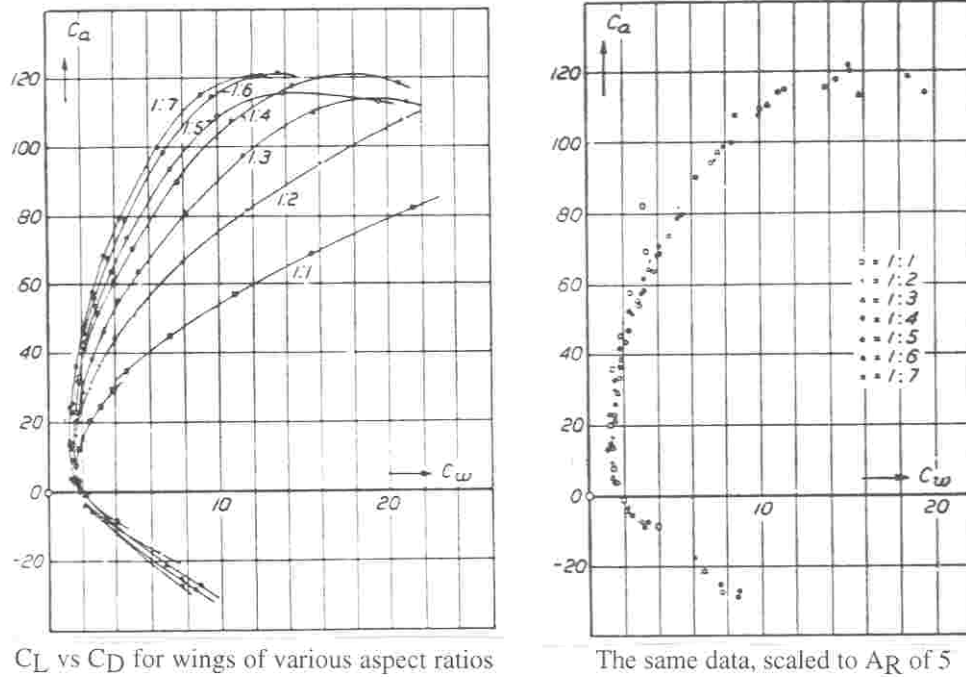

Figure 44: Prandtl's results for the lift (C_a) and drag (C_w) of finite wings. The left-hand plot shows the original data, and the right-hand plot the collapse when it is scaled to an aspect ratio of 5, using (138).

It is also possible to derive a general formula for the lift-curve slope associated with the Fourier series representation. However, it is not especially informative, and the most straightforward approach is to find it numerically from two values of incidence (note that the lifting-line equation gives a linear dependence of Γ, and hence C_L, on α).

Finally, the optimal nature of the elliptical planform is often used to justify its (rare) occurrences in practice – the swallow and Spitfire being the most obvious examples. However, this argument is not entirely watertight, as we shall see.
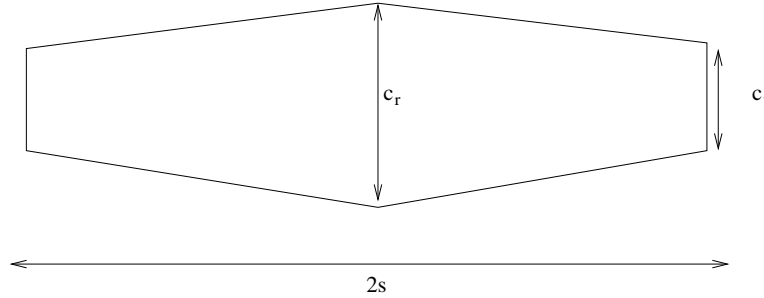
(b) Solutions for tapered planforms

Figure 45: Geometric parameters defining a tapered planform.

To obtain some insight into the characteristics of the lifting-line equation, it is instructive to consider its solution for tapered planforms, without twist or spanwise section variation. Such planforms are defined by the ratio of tip to root chord, c_t/c_r (see Figure 45), and the results of the lifting-line calculations are given by Glauert, for $A_R = 2\pi$. Figure 46 shows the lift distributions for the extreme cases $c_t/c_r = 0$ (full taper) and $c_t/c_r = 1$ (rectangle), as well as half-taper ($c_t/c_r = \frac{1}{2}$) and elliptical planforms. It is notable how close the rectangle and half-taper distributions are to elliptical. Even the full-taper distribution lies nearer to the ellipse than we would expect from its geometry. Equivalently, we can say that the first term in the Fourier series for the circulation tends to dominate, even for non-elliptical planforms. This feature of the lifting-line equation means that the lift-distribution on most practical wings can often usefully be approximated as elliptical.

To reinforce this point, consider the parameter δ, introduced in (138) to describe the fractional increase in induced drag over the elliptical ideal (for a given aspect ratio). Glauert's plot of this quantity against the tapered wing chord ratio is shown in Figure 47. The increase in induced drag is comfortably under 5% over a wide range, and is only around 6% even for the rectangular wing. **We thus conclude that planform shape has a relatively minor influence, in comparison to aspect ratio.**

So, why *do* swallows and Spitfires have elliptical wings? In the case of the former, the debate remains open. However, the explanation for the Spitfire is more prosaic: more space was required at mid-span to accommodate the undercarriage mechanism and ammunition boxes, so the design was changed from tapered to elliptic. The result, although beautiful, was costly and difficult to manufacture.

(c) The discretisation approach

An alternative to the Fourier series solution method is to revert to the discretised view of the lifting-line model shown in Figure 41. The downwash associated with the trailing legs is easily calculated in terms of the unknown strengths $\Gamma_1, \Gamma_2, \ldots \Gamma_N$. In particular, we can calculate its values at the centres of the bound elements, $w_{d1}, w_{d2}, \ldots w_{dN}$. Then, for the n'th element, the lifting-line equation is

$$\frac{\Gamma_n}{\pi U c_n} = \alpha - \alpha_{0n} - \frac{w_{dn}}{U}, \tag{140}$$

where c_n and α_{0n} are the chord and the camber/twist contribution at this element. Allowing n to vary from 1 to N gives us N equations, which can then be solved for the horseshoe vortex
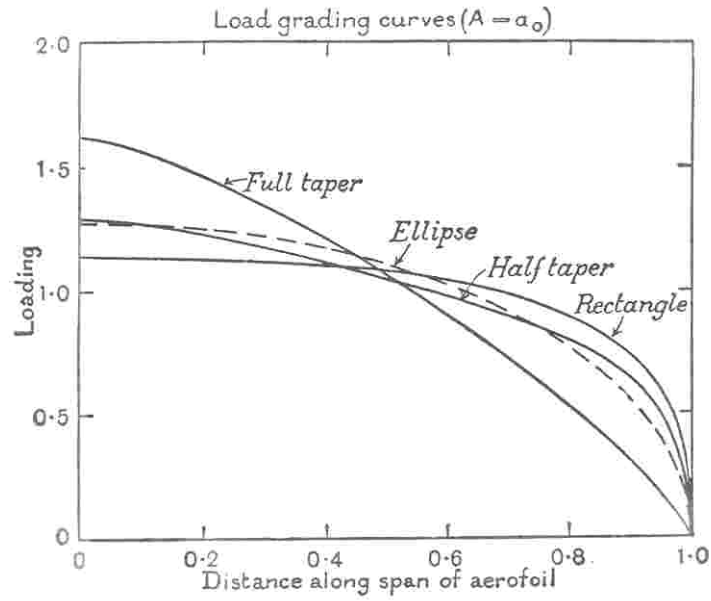
Figure 46: Lift distributions for wings of varying taper ratio (all with aspect ratio 2π).
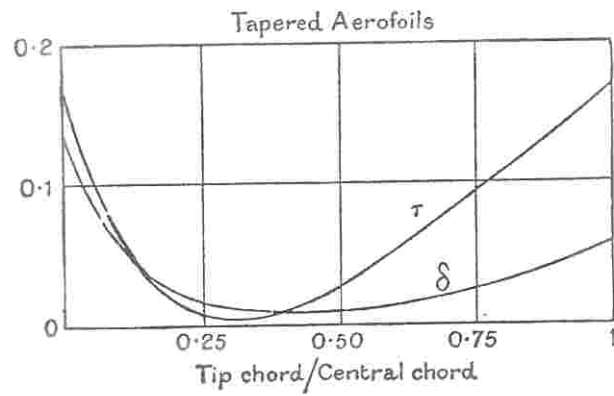

Figure 47: Glauert's results for wings of varying taper ratio. The curve marked δ shows the increase in induced drag over the elliptic ideal.

strengths. The advantage of this approach is that, with a little further thought, it can be generalised to more complex geometries. This topic will be addressed in the section on sweep.

(d) Inverse design with lifting-line

So far, this discussion has been concerned with solving the lifting-line equation for a prescribed wing geometry. Alternatively, however, one may wish to specify a desired lift distribution and find a geometry that achieves it. This 'inverse design' problem is actually *easier* to solve than the 'forwards' problem. Given $\Gamma(y)$, one can evaluate the downwash angle, $\alpha_d(y)$, and then the lifting-line equation simply specifies the relationship between chord and camber/twist distributions that must be satisfied. This is exactly what we did initially with the elliptical lift distribution (see section 3.4.4).

(e) Viscous drag estimation

If one has drag data for the section shape(s) used in the wing, then the results of the lifting-line calculation can be used to provide an estimate of the viscous drag, via integration of the local section drag contributions. Recall that the local lift, $l(y)$, is equal to $\rho U \Gamma(y)$, so

$$\Gamma(y) = \frac{l(y)}{\rho U} = \frac{1}{2} U c(y) c_l(y). \tag{141}$$

This means that the local lift coefficient, c_l, can be calculated from the circulation distribution. The viscous drag coefficient, c_d, is typically given in 'polar' form as a function of c_l, so we now know the local drag, $\frac{1}{2}\rho U^2 c(y) c_d(y)$, and can thus calculate the overall drag coefficient via a numerical evaluation of the integral

$$C_{Dv} = \frac{1}{S} \int_{-s}^{s} c(y) c_d(y) dy. \tag{142}$$

Example: Inverse design for triangular lift distribution

Example (cont'd)

3.5 Lumped Modelling of 3D Wings

We saw the usefulness of a lumped model for analysing interactions between 2D aerofoil sections in Section 2.5. Similarly, problems involving several 3D wings which would become horribly involved using lifting line theory can be quite simply investigated via the **horseshoe vortex model** of a finite wing.
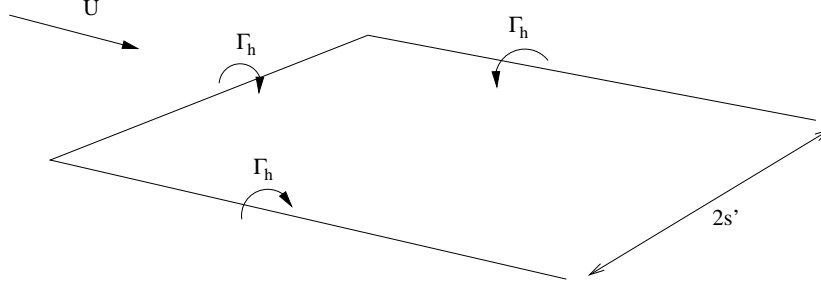

Figure 48: The horseshoe vortex model of a finite lifting wing.

The horseshoe vortex model is shown in Figure 48. It consists of a bound vortex of span $2s'$, and two trailing legs. In order to satisfy the Helmholtz law of vorticity continuity, the bound vortex and the legs have the same circulation (and, in principle, the horseshoe is closed at infinity by the starting vortex of the wing). Given our knowledge of the more detailed wing flow, this is clearly a valid qualitative representation, but we do not yet know the appropriate values of the circulation, Γ_h, and effective semi-span s'.

3.5.1 The horseshoe vortex circulation

We know that, far from the wing, the vortical wake has rolled up into a counter-rotating vortex pair, each with circulation equal to that shed by the two sides of the wing. This, then, must be the circulation of our horseshoe vortex. Thus

$$\Gamma_h = \int_0^s \left(-\frac{d\Gamma}{dy} \right) dy = \Gamma(y=0) = \Gamma_0. \tag{143}$$

The strength of the horseshoe vortex is given by the central (or wing root) value of the bound circulation.

3.5.2 The effective span

The lift on the bound segment of the horseshoe vortex is $\rho U \Gamma . 2s'$, and this tells us that the effective span must be less than the true span if we are to predict the correct lift, because the real bound circulation drops below Γ_0 as the wing tips are approached. For the particular case of the elliptic lift distribution, we have (from (123))

$$L = \rho U \Gamma_0 . \frac{\pi s}{2}, \tag{144}$$

so

$$s' = \frac{\pi}{4} s. \tag{145}$$

In general, the requirement that the lift is correct says that $\rho U \Gamma_0 . 2s'$ must be equal to the integral (106), i.e.

$$s' = \frac{1}{2\Gamma_0} \int_{-s}^{s} \Gamma(y) dy. \tag{146}$$

However, given the general proximity of most circulation distributions to the elliptical form, and the level of approximation involved in the horseshoe vortex model, it is debatable whether this refinement is entirely necessary.

One can also ask whether the effective semi-span required to match the lift gives an accurate representation of the trailing vortex locations. The dynamics of wake roll-up are beyond the scope of this course, but it can be shown that the rolled-up vortices should end up at a spanwise coordinate equal to the 'centroid' of the shed vorticity distribution, i.e.

$$\bar{y} = \frac{1}{\Gamma_0} \int_0^s \left(-\frac{d\Gamma}{dy}\right) y dy. \tag{147}$$

Reassuringly, this turns out to be exactly the same as s', as given by (146). The proof of this result is left to the energetic reader (hint: integrate by parts).
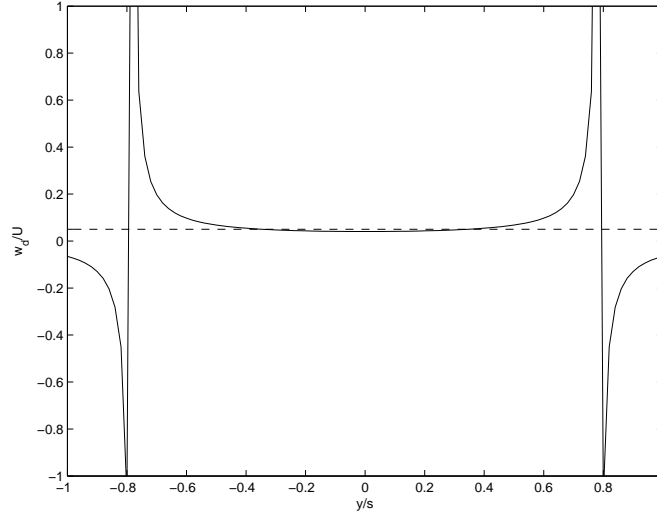
3.5.3 The induced drag

Figure 49: The downwash on the bound element of a horseshoe vortex, for leg spacing appropriate to an elliptical lift distribution and $\Gamma_0/Us = 0.2$. The dashed line shows the lifting-line result for this case.

The induced drag depends on the downwash experienced by the bound segment, and this is where the horseshoe vortex model falls down. The downwash at a location y is

$$w_d(y) = \frac{\Gamma_h}{4\pi}\left[\frac{1}{s'-y} + \frac{1}{s'+y}\right] = \frac{\Gamma_h}{2\pi}\frac{s'}{s'^2 - y^2}, \tag{148}$$

and we have clear problems at $y = \pm s'$. This is confirmed in Figure 49, which shows a plot of (148) for the elliptical distribution, when $s' = (\pi/4)s$. Also shown, as a dashed line, is the constant value predicted by the lifting-line theory in this case. We can see that the horseshoe vortex representation does reasonably well away from the tips, and one possibility is to take the downwash as being constant and equal to the mid-span value. However, this seems unnecessarily crude, given that we know the elliptical distribution result is generally a fair approximation. It

is therefore preferable to use this result directly, and take $w_d = \Gamma_h/4s$. If more accuracy is deemed necessary, for a wing where we know the induced drag polar, i.e.

$$C_{Di} = (1 + \delta)\frac{C_L^2}{\pi A_R},\tag{149}$$

it is possible to show that the equivalent constant downwash is given by

$$\bar{w}_d = (1 + \delta)\frac{\Gamma_h s'}{\pi s^2}.\tag{150}$$

The proof of this is (again!) left to the reader, but note that it does reduce to the correct result for the elliptic case ($s' = (\pi/4)s$, $\delta = 0$).

3.5.4 Application of the horseshoe vortex model

As already stated, the horseshoe vortex representation is useful in assessing interactions between wings. Away from the vortex elements, it gives an increasingly accurate representation of the flow field, so that it *can* be used to estimate the *additional* downwash on another wing. This is best illustrated by an example.

Example: biplane wings of finite span

Example (cont'd)

3.6 Wing Stall

For a finite, unswept wing of reasonably large aspect ratio, the crucial factor additional to 2D considerations is the downwash. As we have seen, this makes the local angle of attack different from the overall aircraft incidence, which means that stall may occur at one spanwise location before another.

3.6.1 General considerations

We have already discussed the desirability of a gradual, rather than abrupt, stall in the context of 2D sections. In the 3D case, this will be achieved by avoiding simultaneous stall at all spanwise locations. (Note, however, that using a section that is well behaved in its 2D characteristics may mitigate this requirement.)

Equally as important is the spanwise location of the section that stalls first. If this is at the tip, then any port/starboard asymmetry (which is almost inevitable) will imply that one tip stalls first, resulting in a large rolling moment. As stall is associated with low-speed flight, which is usually close to the ground, a tip-stalling wing is clearly to be avoided.

3.6.2 The local lift coefficient

The key to understanding planform stall behaviour is the link between lift (or circulation) distribution, chord and lift coefficient. This was given in (141), and is repeated here:

$$\Gamma(y) = \frac{1}{2}Uc(y)c_l(y). \tag{151}$$

The proximity of a section to stall depends on its *lift coefficient*, rather than its absolute loading (ie circulation). We must thus consider the *ratio* between the circulation and chord distributions. This is shown diagramatically for four different planforms, in Figure 50. For each planform, the diagrams show (clockwise from top left) the geometry, the chord (or 'area') distribution, the circulation (or 'load') distribution and the local lift coefficient. We see that the large outboard chord of the rectangular wing gives it very safe stall characteristics, since the sections with highest lift coefficients are at the root. In contrast, a strongly tapered wing has more loading than chord outboard, and is thus prone to a disastrous tip stall. The simple tapered wing offers a fairly close match between loading and chord distributions, with maximum lift coefficients inboard of the tips, while the elliptic lift distribution has uniform lift coefficient across the entire span (as can also be straightforwardly deduced from the downwash distribution in this case).

Thus, in the absence of further design intervention, a rectangular wing will stall first at the root, a strongly tapered one at the tip, and a moderately-tapered one at mid span. In the rest of this section we discuss how a designer can modify these basic characteristics.

3.6.3 Washout

The most common solution to the problem of unwanted tip stall is to twist the sections in this region downwards. This will reduce the local loading, while maintaining the same chord distribution, and hence will reduce the lift coefficient; it is known as applying 'washout' to the wing. The downside, of course, is that the lift distribution will depart somewhat from the ideal. It is possible, through a judicious choice of planform and twist, to design a wing with off-loaded tips at stall *and* an elliptic lift distribution at one given design incidence, but the distribution will be non-ideal at other angles of attack.

Note also that, since camber and twist appear via the same term in the lifting-line equation, one can also achieve washout by decreasing the section camber towards the tips. This approach is known as 'aerodynamic washout'.
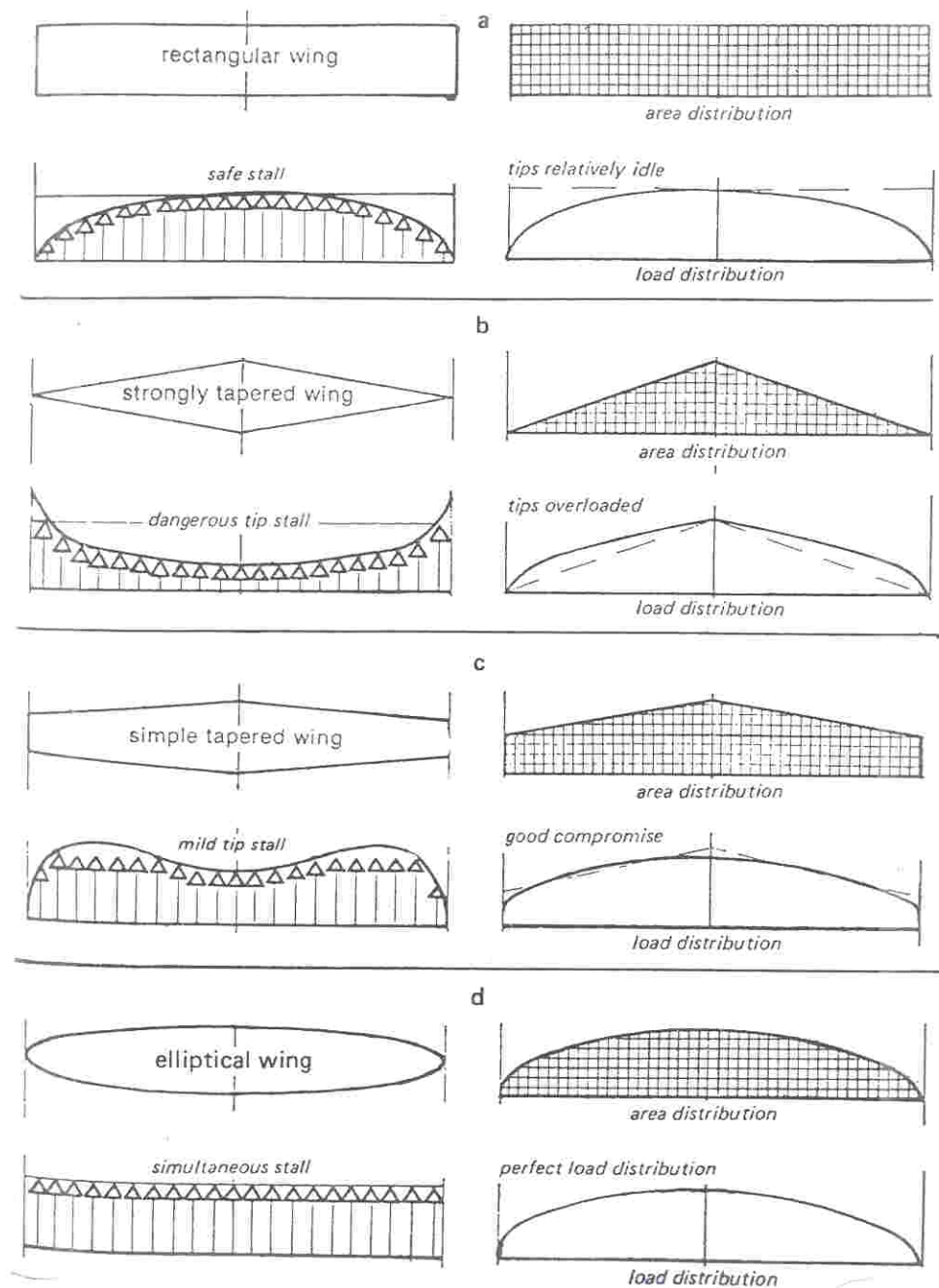
Figure 50: The effect of planform on local lift coefficient (bottom left diagram of each set).

3.6.4 Combined geometric and aerodynamic washout

The off-design penalties of pure washout can be mitigated via a cunning approach described by Simons. This hinges on the observation that increasing a section's camber tends to increase its maximum lift coefficient, as shown in Figure 51. Thus, if one washes out a wing using twist, and then opposes that washout with increased camber ('wash-in'), it is possible to obtain a wing that is more resistant to stall at the tips, and can thus maintain a near-ideal lift distribution across its operating range.
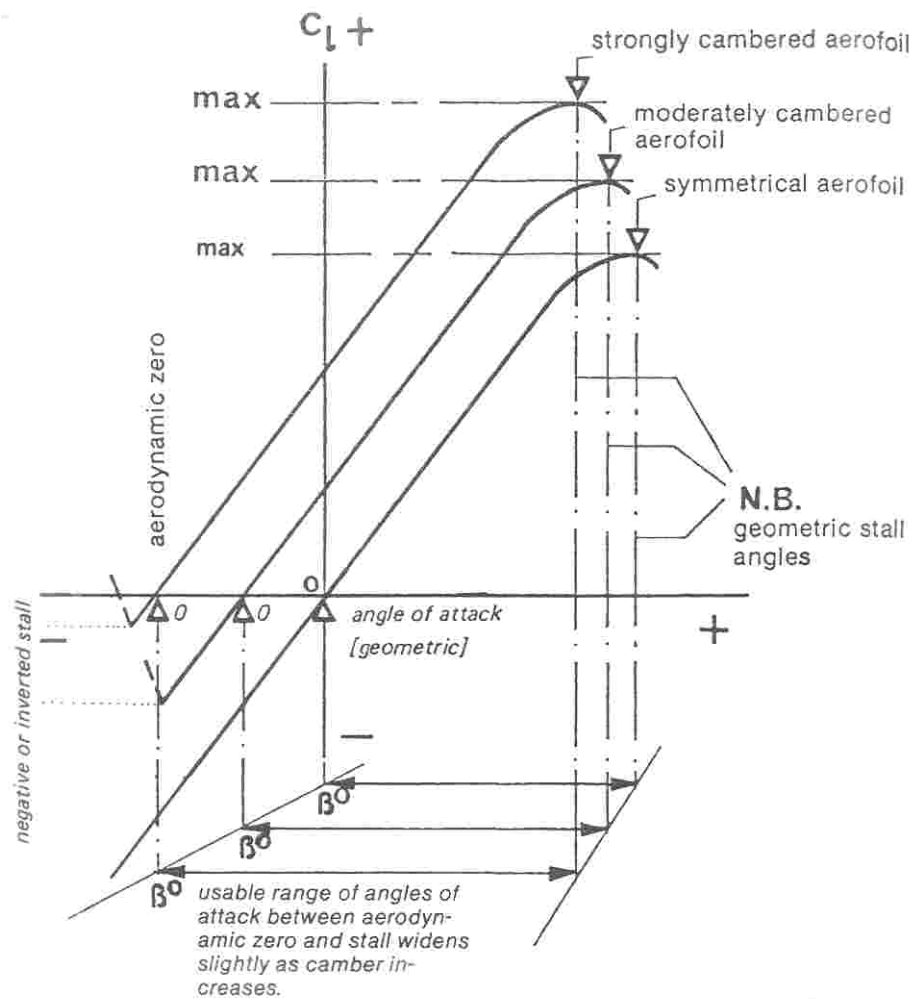

Figure 51: The effect of camber on an aerofoil's 2D lift curve.

3.6.5 Post-hoc fixes

Once a wing has been designed and manufactured, there is a strong incentive to fix any local separations without resorting to a re-design. In this case, the application of vortex generators (as discussed in Section 2.6) may be necessary.

72

3.7 Sweep

The need for wing sweep-back is not, at first, obvious. However, a quick consideration of aircraft types and their design speeds quickly leads to the conclusion that the extent of sweep that is desirable increases with speed. We shall see why this is shortly.
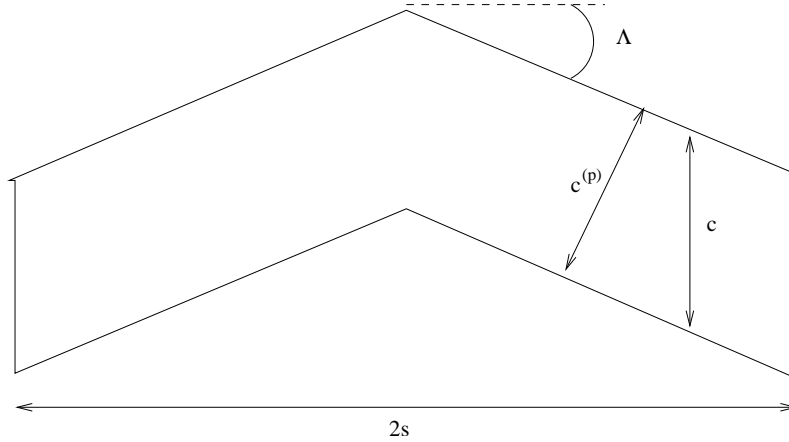

Figure 52: A constant-chord swept wing geometry.

First, however, we need to revisit the nomenclature used to specify the wing geometry. Figure 52 shows a simple swept-back wing, with sweep angle Λ. The important point to note here is that the chord and span are still defined as the dimensions in the x- and y-directions respectively. We will also sometimes need to refer to the distance perpendicular to the leading edge, $c^{(p)}$. Straightforward geometric considerations show that

$$c^{(p)} = c \cos \Lambda. \tag{152}$$

The order of this section corresponds to that of the unswept wing exposition. First, we consider the '2D' problem of the infinite swept wing. Then we discuss the modifications associated with a swept wing of finite span, before finally moving on to 3D stall characteristics.

3.7.1 The infinite swept wing

(a) The inviscid flow and lift
The key to understanding swept-wing flow is the resolution of the oncoming flow into components perpendicular and parallel to the leading edge (Figure 53). **In a purely inviscid fluid, it is only the perpendicular component that determines the flow field**. This is most easily seen by looking at the problem in a reference frame moving with the axial flow component (i.e. along the wing). Now the flow is purely perpendicular to the leading edge, and the wing is moving axially. Such motion, however, has no effect on the normal velocity boundary condition, and the flow is therefore the same as if the wing were still. This observation is known as the **independence principle**.

To analyse the flow, then, we need to work in the plane perpendicular to the leading edge. It is most straightforward to keep the wing in the x-y plane, and represent incidence by an oncoming flow at angle α to the x-axis (Figure 54(a)). For typical operating angles, this gives upwash $U\alpha$ and x-component U, the latter of which is then resolved into components parallel and perpendicular to the leading edge (Figure 54(b)). The equivalent 2D problem is thus that shown in Figure 55.
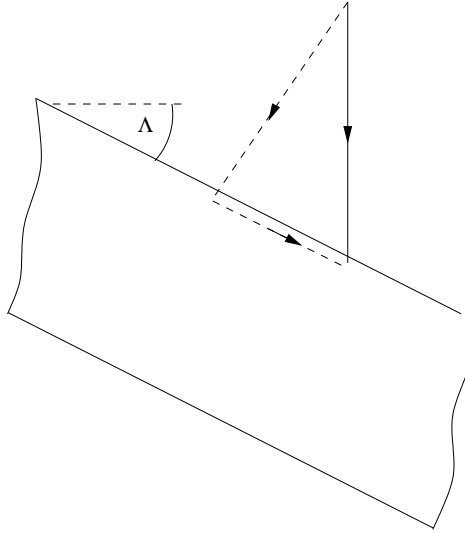
73

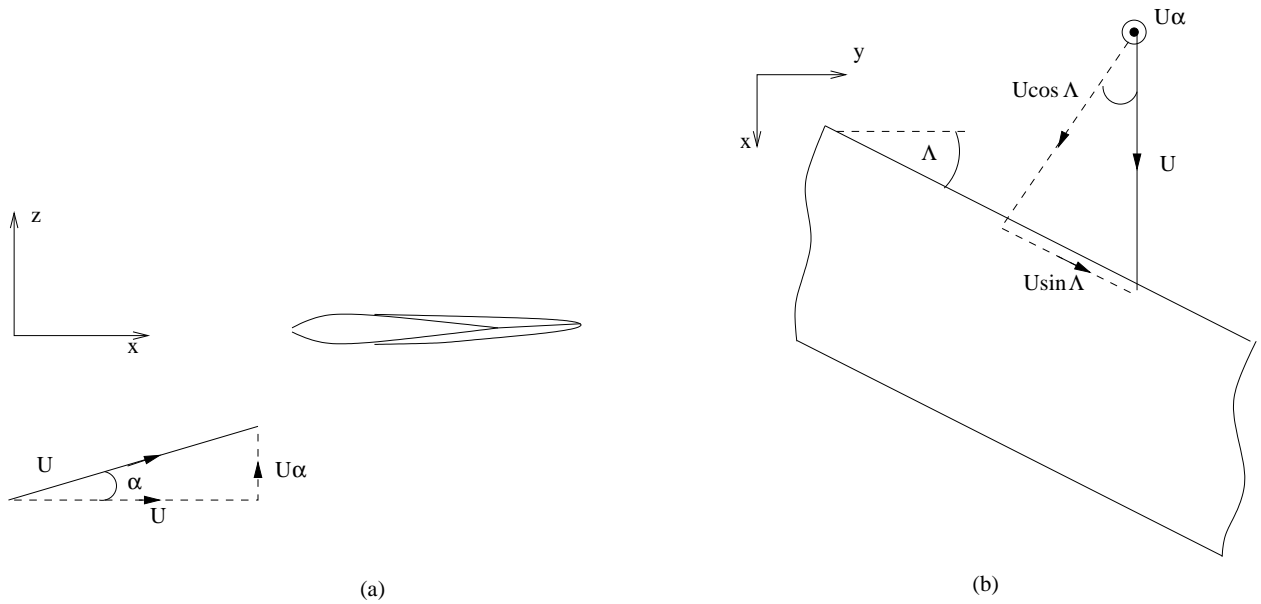Figure 53: Resolving the oncoming flow into components parallel and perpendicular to a swept wing.

Figure 54: Resolved components of the flow at incidence to a swept wing: (a) side view; (b) plan view.
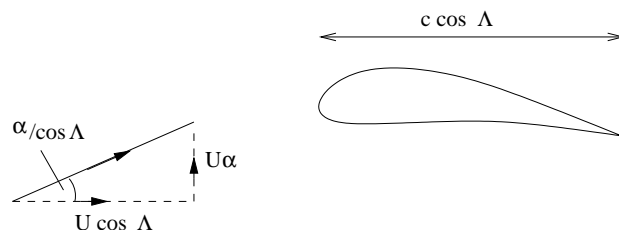

Figure 55: Oncoming flow to a swept wing in the plane perpendicular to the leading edge.

First, consider the most straightforward case, where the aerofoil section is uncambered. Then, according to thin aerofoil theory, the 2D lift coefficient in this view is $2\pi\alpha/\cos\Lambda$, so the lift (per unit distance normal to this plane) is

$$l^{(p)} = \frac{1}{2}\rho(U\cos\Lambda)^2 c\cos\Lambda\frac{2\pi\alpha}{\cos\Lambda} = \pi\rho U^2 c\alpha\cos^2\Lambda. \tag{153}$$

The overall lift coefficient is

$$C_L = \frac{l^{(p)}}{\frac{1}{2}\rho U^2(1.c\cos\Lambda)} = 2\pi\alpha\cos\Lambda. \tag{154}$$

Thus, in the absence of camber, we expect sweep to reduce the lift-curve slope of the wing by a factor of $\cos\Lambda$.
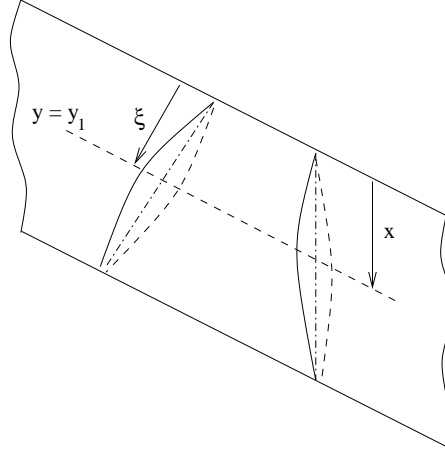

Figure 56: Projection of the streamwise section geometry into the plane perpendicular to the wing axis.

Now we consider what happens in the more practical case where the section is cambered. This means we need to know the geometry in the cross-sectional plane of Figure 55. From Figure 56 we see that this is simply the projection of the streamwise section onto the shorter, perpendicular chord. The zero-lift angle of this projected section is, from thin aerofoil theory

$$\alpha_0^{(p)} = \frac{2}{\pi c^{(p)}}\int_0^{c^{(p)}}\frac{dy_c}{d\xi}\sqrt{\frac{\xi/c^{(p)}}{1-\xi/c^{(p)}}}d\xi, \tag{155}$$

where ξ is the coordinate perpendicular to the leading edge, i.e.

$$\xi = x\cos\Lambda. \tag{156}$$

Substituting (156) and (152) into (155) gives

$$\alpha_0^{(p)} = \frac{2}{\pi c\cos\Lambda}\int_0^c\frac{dy_c}{dx}\sqrt{\frac{x/c}{1-x/c}}dx = \frac{\alpha_0}{\cos\Lambda}, \tag{157}$$

where α_0 is the zero-lift angle of the *streamwise* section geometry. The more general version of the lift coefficient in the perpendicular plane is thus

$$2\pi\left(\frac{\alpha}{\cos\Lambda} - \alpha_0^{(p)}\right) = \frac{2\pi(\alpha - \alpha_0)}{\cos\Lambda}, \tag{158}$$

75

in other words, α is simply replaced by $\alpha - \alpha_0$. The expression for the overall lift coefficient thus becomes

$$C_L = 2\pi(\alpha - \alpha_0)\cos\Lambda \tag{159}$$

and we can say, in general, that **sweep reduces the lift-curve slope of an infinite wing by a factor** $\cos\Lambda$.

(b) Viscous effects

The argument behind the independence principle is invalidated by the no-slip boundary condition. This means that we cannot expect the two-dimensionality of the potential field to continue into the boundary layer. Equally, however, we cannot expect the boundary layer to be purely two-dimensional in the *streamwise* plane, as it is now subject to spanwise (i.e. y-direction) pressure gradients. (This can be seen from the potential field isobars in Figure 57.)
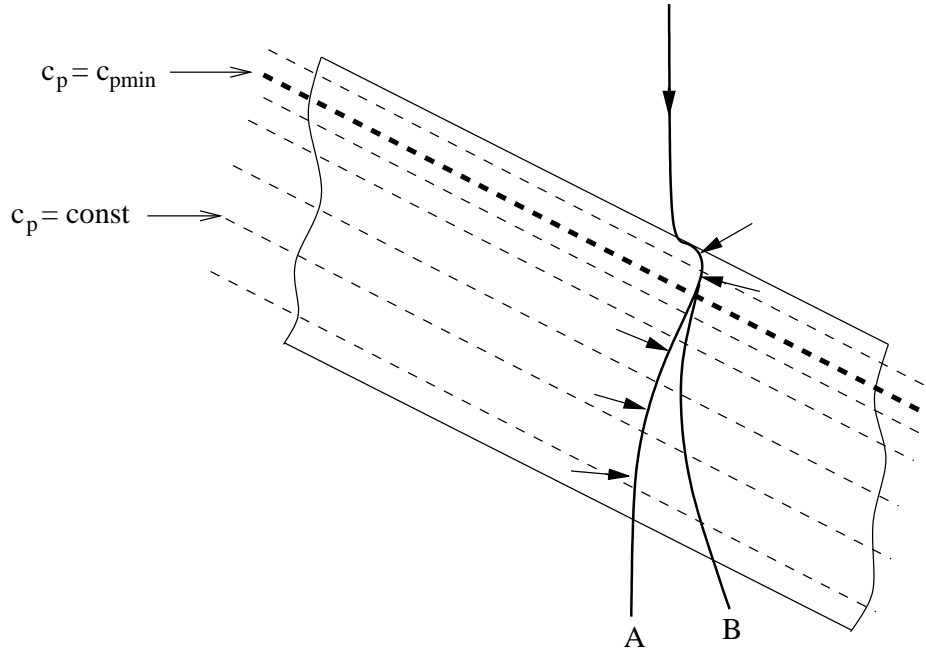

Figure 57: Flow on an infinite swept wing. Streamline A is outside the boundary layer. The directions of the pressure forces normal to this streamline are shown by arrows. Streamline B, inside the boundary layer, is subject to the same pressure field, but exhibits greater curvature, due to the lower velocities in the boundary layer.

A starting point is to consider the path taken by a fluid particle in the potential flow outside the boundary layer. This can be deduced by combining the 2D velocity field in the perpendicular plane with the constant axial component, and is shown as line A in Figure 57. The directions of the pressure forces normal to this streamline are indicated by arrows; they can be seen to be consistent with its curvature. A fluid particle in the boundary layer will experience the same pressure forces, but they will cause greater curvature in its path (as it has a lower speed). We thus expect a boundary layer streamline to follow line B, implying significant spanwise flow as the trailing edge is approached. This tends to thicken the boundary layer there in comparison to an unswept wing, as the flow has been retarded for longer. Heuristically, then, we would expect swept wings to have worse drag and stall characteristics than their unswept counterparts, and this turns out to be the case.

(c) The need for sweep

We have seen that a swept wing will tend to have more drag for a given loading. Furthermore, structural issues mean it will also be heavier. So why employ sweep at all? The reason is to delay the adverse effects of compressibility as the speed of sound is approached. Like the lift, these phenomena depend on the flow component perpendicular to the leading edge, and can thus be greatly mitigated by sweep. Figure 58 shows the results of a NACA experiment reported by Jones, in which the drag coefficients of a swept and an unswept model were measured as a function of Mach number. The benefit of sweep is immediately apparent.
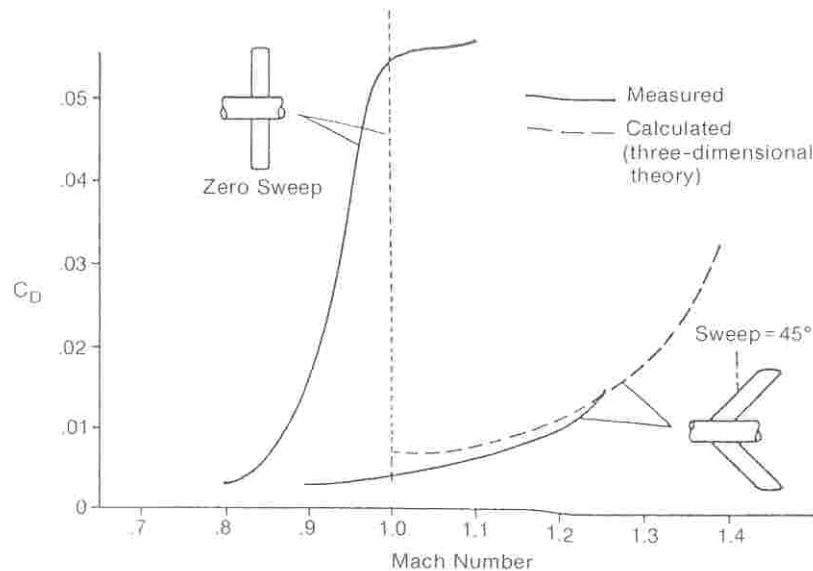

Figure 58: The drag benefits of sweep for high speed flight.

(d) Lumped-parameter model

Finally, it is worth noting that, like the 2D unswept wing, the infinite swept wing can be represented by a lumped-parameter model. This follows directly from the 2D thin aerofoil theory applied to the section geometry in the plane perpendicular to the leading edge, and is shown in Figure 59. (Here C_{M0} and α_0 are the properties of the *streamwise* section geometry.)

3.7.2 Finite swept wings

Like their infinite counterpart, finite swept wings exhibit some important differences compared to the unswept case. These can be calculated by the same numerical methods as discussed previously, but *not* by the classical lifting-line theory. Once the quarter-chord line is allowed to curve, the downwash on the bound vortex includes an infinite self-induced contribution (try applying Biot-Savart to a pair of semi-infinite vortices joined at an angle to see an example of this). This implies that at least *some* account of the finite chord must be taken for swept-back wings, and this is achieved via the **extended lifting-line theory**.

(a) Extended lifting-line theory

This consists of an extension of the classical approach to incorporate the lumped parameter representation of the 2D wing. Consider, first, a 3D view of this representation for the unswept wing (Figure 60(a)). The bound vortex lies along the quarter-chord line, and the collocation
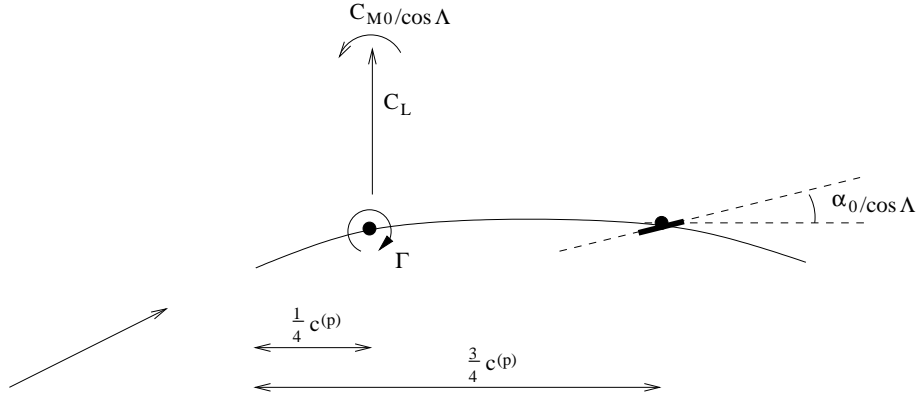
77

Figure 59: Lumped parameter model for a swept wing.

point is replaced by a line at three-quarters chord. Now allow the bound vorticity to vary slowly in the spanwise direction (Figure 60(b)), so the local flow at any spanwise location is still effectively two-dimensional and the 2D lumped model still holds. The only difference is an additional velocity component at the collocation line: the downwash associated with the trailing vortex sheet. The condition of zero normal flow at the collocation line thus leads to an integral equation for the bound vortex strength $\Gamma(y)$, just as in the classical case. The more complicated geometry here, however, makes this equation intractable analytically, so a more relevant representation is the discretised version shown in Figure 60(c). Here we have N collocation points, each of which gives us an equation linking the N unknown horseshoe vortex circulations. This is the extended lifting-line equivalent of the discretisation suggested for the classical theory (Figure 41).

There are clear differences between the two theories' representations of the unswept wing. However, these differences are associated with parameters that are assumed small (chord in comparison to span, spanwise variation of lift), and we would therefore only expect them to become significant as the aspect ratio decreases and the theories become less accurate. One can also query the necessity of forcing the trailing vortex sheet to follow the aerofoil surface to the trailing edge, and some practical implementations simply extend it parallel to the free stream from the bound vortex.

While the extended and classical theories are effectively equivalent for the unswept wing, the latter is, as we have seen, inapplicable to wings with sweep. In contrast, the application of the extended theory is straightforward. For the simple swept wing it takes the form shown diagramatically in Figure 61.

The contribution of each bound vortex element to the lift is, from our lumped model, $\rho U \Gamma \cos \Lambda$ per unit length. The induced drag calculation is harder to generalise from the classical case, and this is an issue that we will not consider.

(b) A digression: winglets

The expression for the lift per unit length of the bound vortex, $\rho U \Gamma \cos \Lambda$, can be written in the more general form $\rho \boldsymbol{U} \times \boldsymbol{\Gamma}$ (remember that the angle between the bound vortex and the freestream is $\frac{\pi}{2} - \Lambda$). This generalisation is all we need to make the extended lifting-line theory applicable to non-planar geometries. In particular, it allows us to consider the go-faster stripes of modern civil aircraft: winglets.

It is sometimes claimed that winglets act like end-plates, and thus make the wing flow two-dimensional. This view is, at best, only part of the story, as can be seen by considering the extended lifting-line discretisation of a wing with a vertical winglet (Figure 62). The directions of the quarter-chord circulations on the winglet elements can be deduced from the circulatory
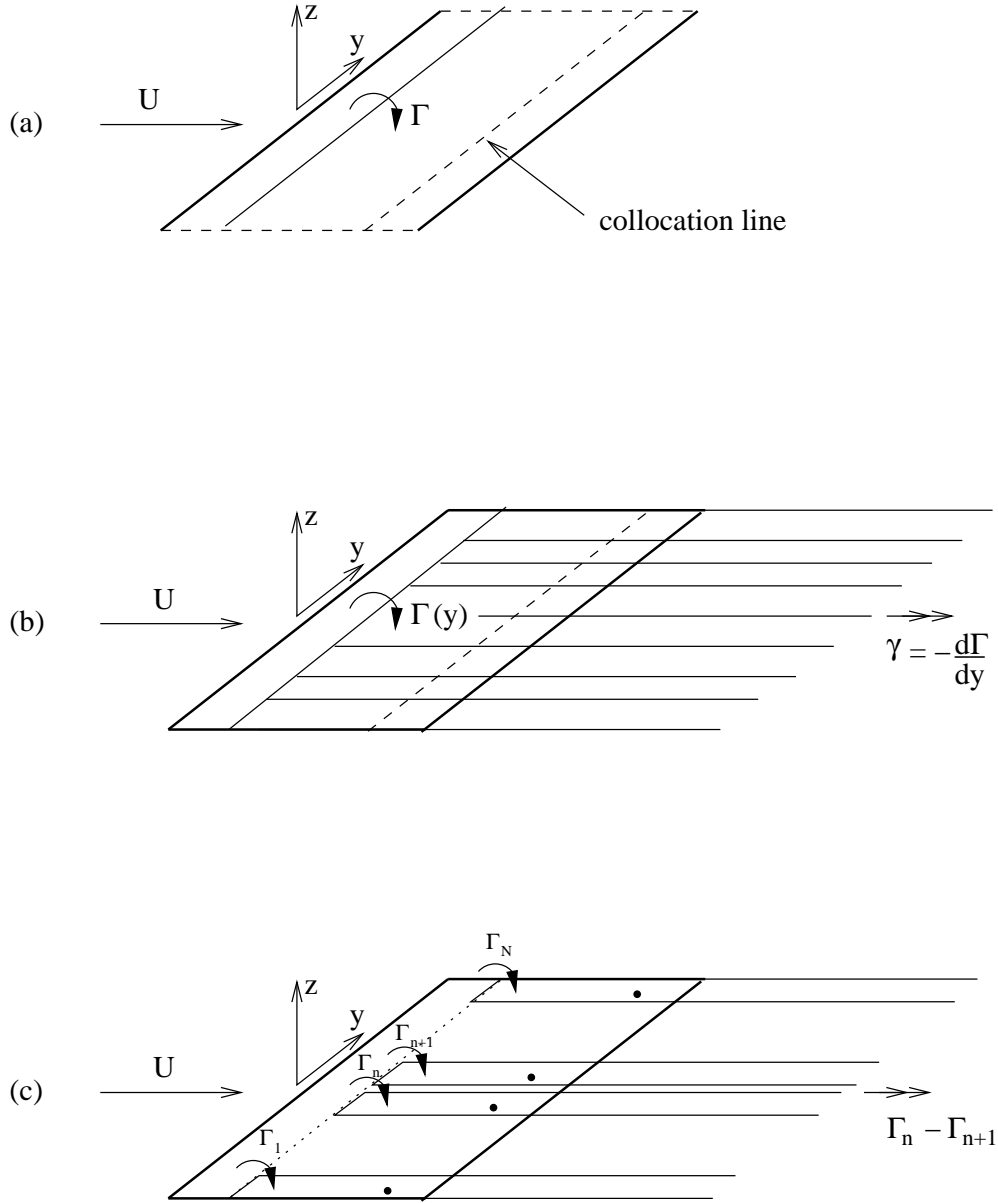
78

Figure 60: Application of 2D lumped-parameter model in the extension of lifting-line theory: (a) 2D lumped-parameter model viewed in 3D; (b) development of 2D model for finite wing; (c) discretised version of (b), with collocation points replacing line.
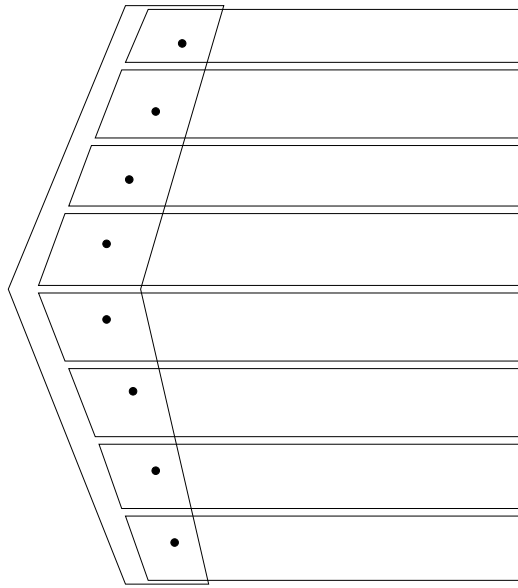
Figure 61: The extended lifting-line model applied to a swept-back wing. Collocation points lie on the three-quarter chord line, centred between trailing vortex legs.
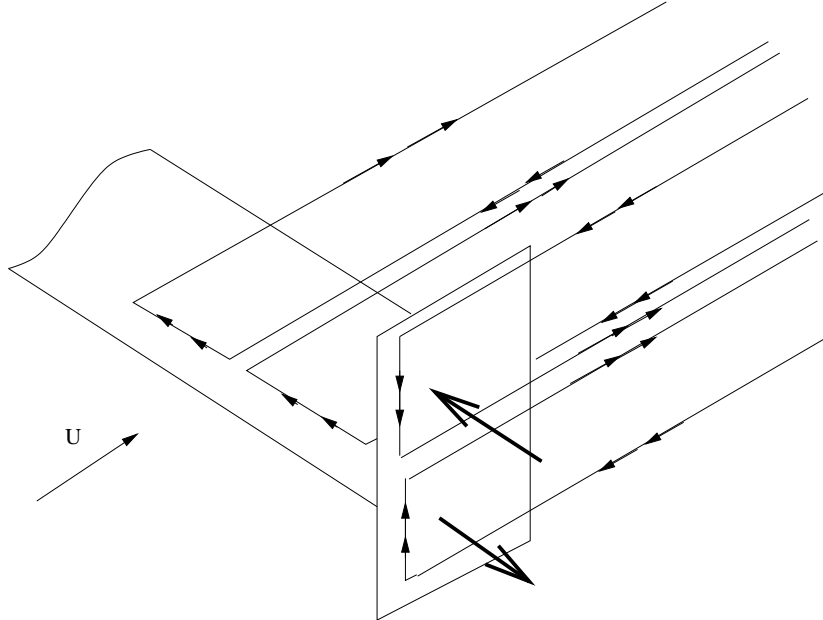

Figure 62: Extended lifting-line representation of a simple, end-plate winglet. The directions of the line vortex circulations are indicated by double-headed arrows. Also shown are the forces on the winglet bound vortices.

velocity components at the collocation points, and the associated forces follow from the cross-product rule above. We can deduce that:

(i) the presence of the winglets will increase the circulation near the wing tip, as it is no longer constrained to zero there. They should thus enhance the lift somewhat;

(ii) the trailing vorticity shed by the winglets is slightly further from the wing than it would be in their absence. There should thus be a reduction in induced drag;

(iii) the forces on the winglet act to increase the bending moment at any given wing section.

Winglets are thus far from pure end-plates; they cannot restore fully 2D flow, nor can they prevent the *eventual* shedding of any of the bound vorticity. Furthermore, they amplify the structural requirements on the wing, just as an increase in aspect ratio would. When one also factors in the additional skin friction drag that they create, it is not surprising that the design of an effective winglet has been found to require care. In particular, the surfaces tend to be oriented somewhat away from the vertical, in order to produce lift (and even thrust) components. An example of a realistic geometry is shown in Figure 63.
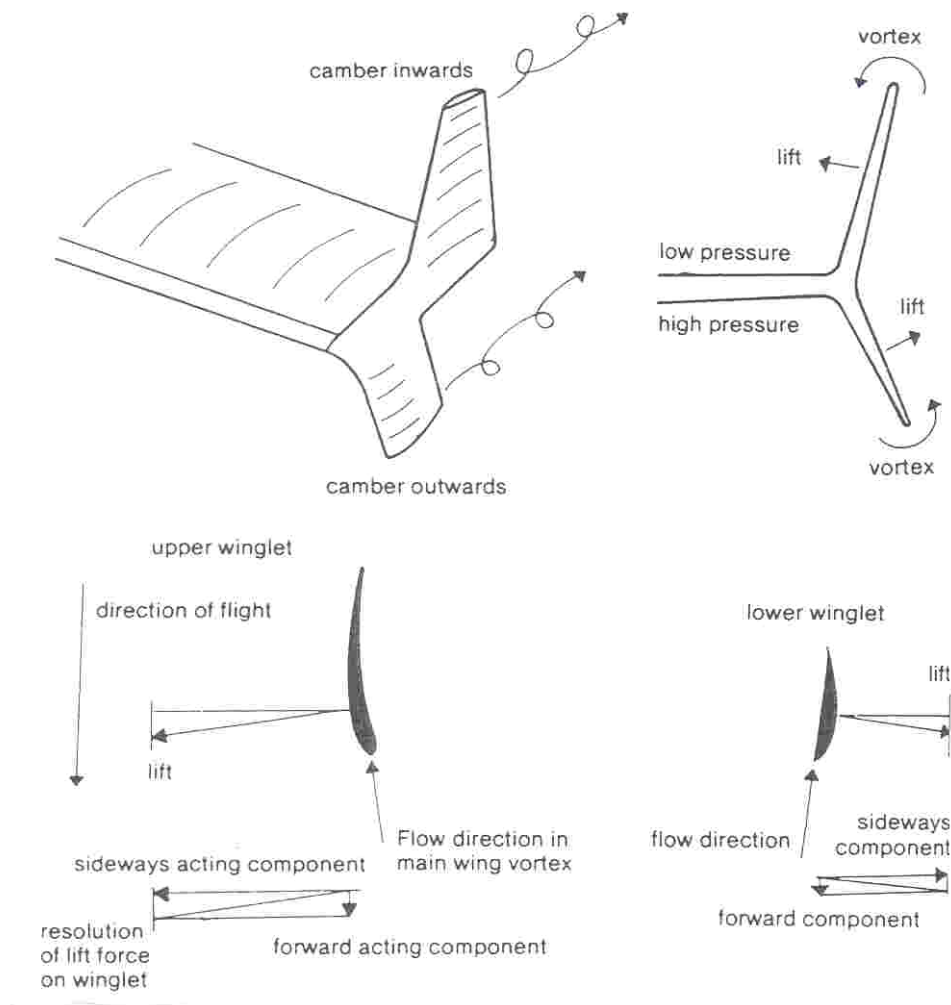

Figure 63: A practical winglet, designed by Whitcomb.

81

3.7.3 Swept wing stall

We have already seen that secondary flows in the boundary layer are likely to reduce C_{Lmax} in the '2D', infinite-sweep case. Here, then, we concentrate on the additional effects for finite swept wings.

The first point is that the backwards-swept geometry tends to increase tip loading relative to root loading in comparison to an unswept wing. This can be argued with reference to Figure 61. We first claim that the change in a horseshoe's geometry has a small effect on the downwash at its own collocation point. This leaves the legs of neighbouring horseshoes as the most important factors. For inboard vortices, the increase in upwash due to the forwards shift of one neighbour's leg will tend to be cancelled out by the decrease due to the rearwards shift of the other's. At the tip, however, only the forwards-shifted neighbour leg is present, so we expect more upwash, and hence a loading gain, relative to the centre. Confirmation of this reasoning (and the converse for a forward-swept wing) is provided by the numerical results shown in Figure 64. Both forward- and rearward-swept wings have reduced, and almost identical, lift-curve slopes, as one would expect from the 2D discussion. Their lift distributions, however, show significant differences, with the expected increase in tip loading with rearward sweep.
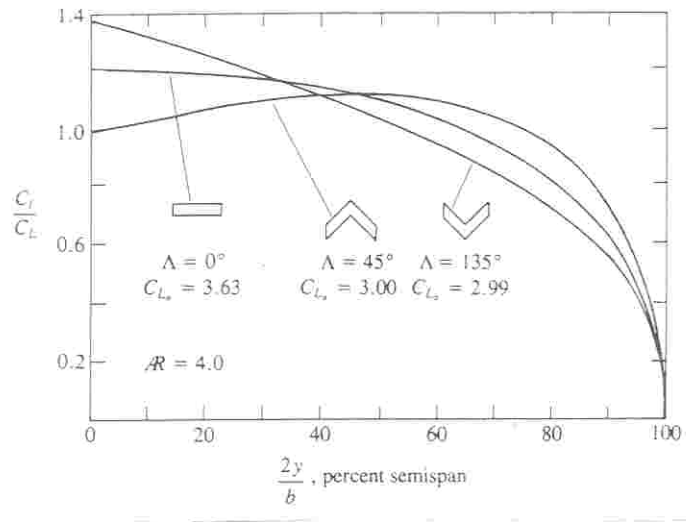

Figure 64: Effect of sweep angle on lift distribution and lift-curve slope. (Calculated numerically using a lifting-surface method.)

The second point is associated with the boundary layer cross-flow. While this is the same at all spanwise locations for the infinite swept wing, it is suppressed near the root on a real wing by the presence of the fuselage. The boundary layer near the tip is thus more susceptible to separation. A post-hoc fix for this problem is to inhibit the cross-flow by installing a chordwise 'fence'. Early fences extended along the entire chord, but then designers worked out that a part-chord fence would also work, thanks to the streamwise vortex shed by it (Figure 65(a)). This insight led to the development of other, vortex-generating devices, such as the vortilon (Figure 65(b)) and saw-tooth leading edge (Figure 65(c)).

Both the issues we have discussed mean that rearward-swept wings are more susceptible to tip stall than unswept planforms. Furthermore, tip stall is an even *bigger* problem for swept-wing aircraft, because the tips are typically aft of the centre of gravity, so a loss of lift there tends

82
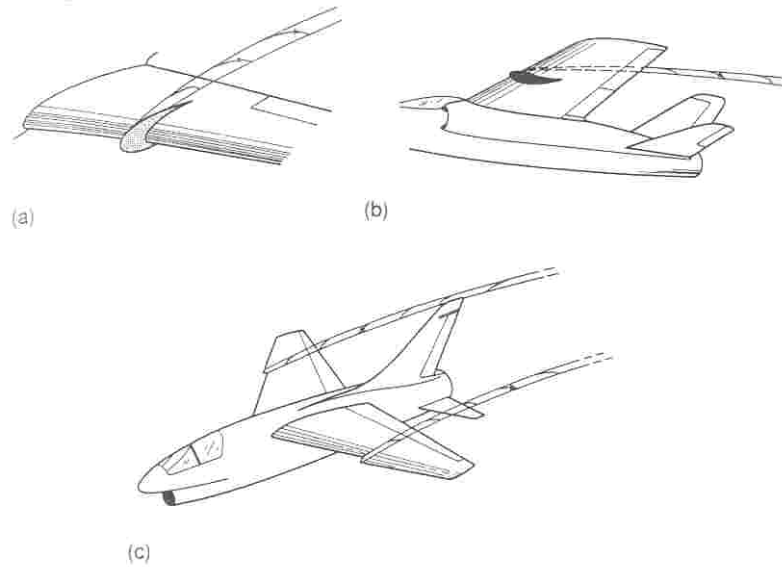
Figure 65: Devices for inhibiting cross-flow: (a) fence; (b) vortilon; (c) saw-tooth leading edge.

to pitch the aircraft upwards - the last thing a pilot wants! Unfortunately, foward-swept wings represent a huge structural design problem (they are susceptible to flutter), so rearward sweep combined with washout has so far been the solution of choice for high-speed flight. However, its associated problems mean that there is strong pressure on aerodynamicists to produce 2D sections with better transonic performance, thereby reducing the degree of sweep required.

A The Glauert Integral

The Glauert integral was introduced in equation (53), repeated here:

$$I_n = \int_0^\pi \frac{\cos n\phi}{\cos \phi - \cos \theta} d\phi.$$

In this appendix we prove the result quoted,

$$I_n = \pi \frac{\sin n\theta}{\sin \theta}, \tag{160}$$

using an induction argument.

First consider the case $n = 0$. We make the substitution

$$\tan \frac{1}{2}\phi = t, \tag{161}$$

which implies

$$\frac{1}{2}\sec^2 \frac{\phi}{2} d\phi = dt \tag{162}$$

$$d\phi = \frac{2dt}{1 + t^2} \tag{163}$$

and

$$\cos \phi = \cos^2 \frac{\phi}{2} - \sin^2 \frac{\phi}{2} = \frac{1 - t^2}{1 + t^2}. \tag{164}$$

The integral becomes

$$I_0 = \int_0^\infty \frac{2}{(1 - t^2) - (1 + t^2)\cos \theta} dt = \int_0^\infty \frac{2}{(1 - \cos \theta) - t^2(1 + \cos \theta)} dt. \tag{165}$$

At this stage, we have to confront the problem of zero denominator at $\phi = \theta$ ($t^2 = (1 - \cos \theta)/(1 + \cos \theta)$). To show that the integral exists, we split the integration range into two parts:

$$0 \leq t \leq t_0 - \epsilon \quad , \quad t_0 + \epsilon \leq t \leq \infty \quad , \quad t_0 = \sqrt{\frac{1 - \cos \theta}{1 + \cos \theta}}. \tag{166}$$

The integrals over these ranges are finite, and we can find I_0 by adding them and letting $\epsilon \to 0$. (This is known as finding the *principal value* of the integral.)

First, we find the indefinite integral:

$$
\begin{aligned}
\int \frac{2}{(1 - \cos \theta) - t^2(1 + \cos \theta)} dt &= \frac{1}{\sqrt{1 - \cos \theta}\sqrt{1 + \cos \theta}} \int \left[\frac{1}{t_0 - t} + \frac{1}{t_0 + t} \right] dt \\
&= \frac{1}{\sin \theta} \log \left| \frac{t_0 + t}{t_0 - t} \right|.
\end{aligned} \tag{167}
$$

The definite integral becomes

$$
\begin{aligned}
I_0 &= \lim_{\epsilon \to 0} \left\{ \left[\frac{1}{\sin \theta} \log \left| \frac{t_0 + t}{t_0 - t} \right| \right]_0^{t_0 - \epsilon} + \left[\frac{1}{\sin \theta} \log \left| \frac{t_0 + t}{t_0 - t} \right| \right]_{t_0 + \epsilon}^{\infty} \right\} \\
&= \frac{1}{\sin \theta} \lim_{\epsilon \to 0} \left\{ \log \frac{2t_0 - \epsilon}{\epsilon} - \log \frac{2t_0 + \epsilon}{\epsilon} \right\} \\
&= \frac{1}{\sin \theta} \lim_{\epsilon \to 0} \left\{ \log \frac{2t_0}{\epsilon} + \log \left[1 - \frac{\epsilon}{2t_0} \right] - \log \frac{2t_0}{\epsilon} - \log \left[1 + \frac{\epsilon}{2t_0} \right] \right\} \\
&= 0.
\end{aligned}
\tag{168}
$$

This is consistent with the claimed result, as $\sin n\theta = 0$ for $n = 0$.

Next we address I_1. Here we have

$$
\begin{aligned}
I_1 = \int_0^\pi \frac{\cos \phi}{\cos \phi - \cos \theta} d\phi &= \int_0^\pi \left[1 + \frac{\cos \theta}{\cos \phi - \cos \theta} \right] d\phi \\
&= \pi + I_0 \cos \theta \\
&= \pi,
\end{aligned}
\tag{169}
$$

which again agrees with (160).

Finally, we are now in a position to prove the general result. First consider the combination $I_{n-1} + I_{n+1}$:

$$
\begin{aligned}
I_{n-1} + I_{n+1} &= \int_0^\pi \frac{\cos(n-1)\phi + \cos(n+1)\phi}{\cos \phi - \cos \theta} d\phi \\
&= 2 \int_0^\pi \frac{\cos n\phi \cos \phi}{\cos \phi - \cos \theta} d\phi \\
&= 2 \int_0^\pi \left[1 + \frac{\cos \theta}{\cos \phi - \cos \theta} \right] \cos n\phi \, d\phi \\
&= 2 \cos \theta I_n.
\end{aligned}
\tag{170}
$$

Thus we have the recurrence relation

$$
I_{n+1} = 2 \cos \theta I_n - I_{n-1}.
\tag{171}
$$

for $n \geq 1$. In particular, if I_n and I_{n-1} are given by (160), then

$$
\begin{aligned}
I_{n+1} &= 2\pi \cos \theta \frac{\sin n\theta}{\sin \theta} - \pi \frac{\sin(n-1)\theta}{\sin \theta} \\
&= \frac{\pi}{\sin \theta} \left[2 \sin n\theta \cos \theta - \sin n\theta \cos \theta + \cos n\theta \sin \theta \right] \\
&= \frac{\pi}{\sin \theta} \left[\sin n\theta \cos \theta + \cos n\theta \sin \theta \right] \\
&= \pi \frac{\sin(n+1)\theta}{\sin \theta}.
\end{aligned}
\tag{172}
$$

In summary, we have shown directly that (160) holds for $n = 0$ and 1, and that its validity for $n - 2$ and $n - 1$ implies that it holds for n ($n \geq 2$). The proof by induction is therefore complete.

Finally, the thin aerofoil theory derivation also calls on an expression for $I_{n-1} - I_{n+1}$. This follows directly from (160):

$$
\begin{aligned}
I_{n-1} - I_{n+1} &= \frac{\pi}{\sin\theta}\left[\sin(n-1)\theta - \sin(n+1)\theta\right] \\
&= \frac{\pi}{\sin\theta}\left[-2\cos n\theta \sin\theta\right] \\
&= -2\pi \cos n\theta.
\end{aligned}
\tag{173}
$$

B   The Biot-Savart Law

The Biot-Savart law is given by equation (101):

$$
\mathbf{u}(\mathbf{x}) = \frac{1}{4\pi}\int_{V'} \frac{\boldsymbol{\omega}(\mathbf{x}') \times (\mathbf{x} - \mathbf{x}')}{|\mathbf{x} - \mathbf{x}'|^3}dV'.
\tag{174}
$$

This is, in fact, no more than an inversion of the definition of vorticity; $\boldsymbol{\omega} = \nabla \times \mathbf{u}$. It does, however, require a bit of work to prove.

We start with the 'Helmholtz decomposition' of the velocity vector:

$$
\mathbf{u} = \nabla\Phi + \nabla \times \mathbf{A},
\tag{175}
$$

where $\mathbf{A}$ is called the **vector potential**. This decomposition is possible for any vector, with the first term representing the irrotational component. The velocity associated with the vorticity is thus given by the second term.

Now $\mathbf{A}$ can be chosen to have zero divergence, as follows. Suppose we have one possible $\mathbf{A} = \mathbf{A}_0$, with $\nabla \times \mathbf{A}_0 = \mathbf{u}$ but $\nabla \cdot \mathbf{A}_0 \neq 0$. Then we can make $\mathbf{A} = \mathbf{A}_0 + \nabla f$, where $\nabla^2 f = -\nabla \cdot \mathbf{A}_0$, and we will have $\nabla \cdot \mathbf{A} = 0$ and $\nabla \times \mathbf{A} = \mathbf{u}$ still.

Next we write the vorticity field in terms of $\mathbf{A}$:

$$
\begin{aligned}
\boldsymbol{\omega} = \nabla \times \mathbf{u} &= \nabla \times (\nabla \times \mathbf{A}) \\
&= \nabla(\nabla \cdot \mathbf{A}) - \nabla^2\mathbf{A} \\
&= -\nabla^2\mathbf{A}.
\end{aligned}
\tag{176}
$$

In other words, each component of $\mathbf{A}$ satisfies a *Poisson equation*, e.g.

$$
\nabla^2 A_x = -\omega_x.
\tag{177}
$$

If we can solve this equation for the components of $\mathbf{A}$, we can then find the velocity field $\nabla \times \mathbf{A}$ associated with $\boldsymbol{\omega}$.

We find a solution to (177) by considering the separate problem of a flow field $\mathbf{u}_s$ with a source distribution $\sigma(\mathbf{x})$ per unit volume. From superposition of elementary source solutions, we know that the associated potential function is given by

$$
\Phi_s(\mathbf{x}) = -\frac{1}{4\pi}\int_{V'} \frac{\sigma(\mathbf{x}')}{|\mathbf{x} - \mathbf{x}'|}dV'.
\tag{178}
$$

However, we also know that

$$
\nabla^2\Phi_s = \nabla \cdot \mathbf{u}_s = \sigma,
\tag{179}
$$

which is the Poisson equation. For our initial problem, equation (177) therefore has the solution

$$
A_x(\mathbf{x}) = \frac{1}{4\pi}\int_{V'} \frac{\omega_x(\mathbf{x}')}{|\mathbf{x} - \mathbf{x}'|}dV'.
\tag{180}
$$

Corresponding expressions apply for the $y-$ and $z-$components of the vector potential, and our results can be summarised as

$$\mathbf{A}(\mathbf{x}) = \frac{1}{4\pi} \int_{V'} \frac{\boldsymbol{\omega}(\mathbf{x}')}{|\mathbf{x}-\mathbf{x}'|} dV'. \tag{181}$$

The final step is to form $\nabla \times \mathbf{A}$. Here we need the following formulae:

$$\nabla \times \left[\frac{\boldsymbol{\omega}(\mathbf{x}')}{|\mathbf{x}-\mathbf{x}'|} \right] = \left[\nabla \left(\frac{1}{|\mathbf{x}-\mathbf{x}'|} \right) \right] \times \boldsymbol{\omega}(\mathbf{x}') \tag{182}$$

and

$$\nabla \left(\frac{1}{|\mathbf{x}-\mathbf{x}'|} \right) = -\frac{\mathbf{x}-\mathbf{x}'}{|\mathbf{x}-\mathbf{x}'|^3}. \tag{183}$$

(Proofs are left to the reader. Remember that ∇ contains differentials with respect to the elements of $\mathbf{x}$, not $\mathbf{x}'$!) Thus

$$\nabla \times \mathbf{A} = \frac{1}{4\pi} \int_{V'} \frac{\boldsymbol{\omega}(\mathbf{x}') \times (\mathbf{x}-\mathbf{x}')}{|\mathbf{x}-\mathbf{x}'|^3} dV', \tag{184}$$

which is the Biot-Savart law.